

## ABSTRACT

WANG, YIXU. Lithium-Ion Battery Cathode Materials Structure Failure Investigation.  
(Under the direction of Dr. Hsiao-Ying Shadow Huang).

The need for the development and deployment of reliable and efficient energy storage devices, such as lithium-ion rechargeable batteries, is becoming increasingly important due to the scarcity of petroleum. Lithium-ion batteries have been used for a wide range of applications, from power tools and portable electronics to recent plug-in hybrid electric vehicles and pure electric vehicles. Lithium-ion batteries operate via an electrochemical process in which lithium ions are shuttled between cathode and anode while electrons flow through an external wire to form an electrical circuit. The study showed that the development of lithium-iron-phosphate ( $\text{LiFePO}_4$ ) batteries promises an alternative to conventional lithium-ion batteries, with their potential for high energy capacity and power density, improved safety, and reduced cost. However, current prototype  $\text{LiFePO}_4$  batteries have been reported to lose capacity over  $\sim 3000$  charge/discharge cycles or to degrade rapidly under high discharging rates. In this thesis, we report that the mechanical and structural failures are attributed to dislocation formations. Analytical models and crystal visualizations provide details for further understanding the stress developments due to lithium movement during charging or discharging. In the present study, we report three different lithium intercalation-induced dislocation mechanisms explaining experimental observed cracks. We use the theory of elasticity to calculate dislocation stress fields. In most cases, dislocations are not perfectly parallel to one specific axis. Therefore, stress variations for arbitrary dislocation directions are investigated. In addition, multiple dislocations usually co-exist and interact each other in the crystal; therefore we use the superposition method to investigate

stress fields and forces between multiple dislocations. The stress fields manifesting between dislocations are numerically calculated via Mathematica (Wolfram Research, Champaign, IL), and anisotropic material properties of electrodes are employed. The results provide links between stress fields and the observed structural failure in lithium-ion batteries. This study contributes to the fundamental understanding of the mechanisms of capacity loss in lithium-ion battery materials and helps the design of better rechargeable batteries, and thus leads to economic and environmental benefits.

© Copyright 2011 by Yixu Wang

All Rights Reserved

Lithium-Ion Battery Cathode Materials Structure Failure Investigation

by  
Yixu Wang

A thesis submitted to the Graduate Faculty of  
North Carolina State University  
in partial fulfillment of the  
requirements for the degree of  
Master of Science

Mechanical Engineering

Raleigh, North Carolina

2011

APPROVED BY:

---

Dr. Hsiao-Ying Shadow Huang  
Committee Chair

---

Dr. Jeffery Eischen

---

Dr. Gracious Ngaile

## **DEDICATION**

To my parents: Z.G. Wang and Y.Q. Xing. Thank you for all your love, substantially support and faith on me! I would not have made it this far without you!

This work is also dedicated to Dr. Hsiao-Ying Shadow Huang, who led me to this field as a mentor and provided me all the valuable knowledge a researcher requires and all the golden opportunities a graduate student needs. She lights up my way to a bright career.

## **BIOGRAPHY**

Yixu, Richard, Wang was born in Chinfeng, China, in 1987. He received the B.S. in Major of Material Science and Engineering from Zhejiang University in 2009, where his field of specialty was mechanical properties of ceramic and metal materials. Currently, he is pursuing his M.S. degree in Department of Mechanical and Aerospace Engineering, North Carolina State University. His research field is investigating structural failure mechanisms with Li-ion batteries cathode material as the modeling system. His specialty is software aided stress analyzing and fracture mechanisms investigation.

## ACKNOWLEDGMENTS

First and foremost, I would like to express my profound gratitude to NCSU department of Mechanical & Aerospace for supporting me to pursue my graduate studies in U.S. The support has given me not only a future career, but also opportunities to be exposed to industrial opportunities, to work on a project I am interested in, and to prepare myself to better serve the society and the mechanical industry.

There are two people whom I would like to acknowledge individually. First, I am deeply grateful to Professor Hsiao-Ying Shadow Huang, my thesis advisor, for her encouragement, and careful and wise guidance of my project. Secondly, I owe a great deal to Professor Robert T. Nagel, director of graduate program, who was fighting for my opportunity of studying in Mechanical Engineering department.

I would also like to offer my sincerest thanks to my committee members: Dr. Jeffery W. Eischen, for strengthening my academic achievement and wise counsel; and to Dr. Gracious Ngaile, who always answering my inquiries so promptly and providing me valuable advices.

Many thanks are also due to my friends in this department: Jingxiao Lu, Letisha McLaughlin, Mike Stamps, Siyao Huang, Chen-kai Chiu Huang, Siqi Xu, Jing Ouyang, Guang Yang, Shuwei Yang, and many others who always provide me both academic and emotional supports during the long process of completing this project.

Finally, I would like to thank all my friends in Raleigh who have always supported me. You made my life here colorful. It would be difficult to acknowledge everyone who has in some way or another contributed to the research reported in this thesis.

## TABLE OF CONTENTS

LIST OF TABLES .....	vii
LIST OF FIGURES .....	viii
CHAPTER 1 INTRODUCTION .....	1
1.1 The Needs for Alternative Energy Solution.....	1
1.2 Rechargeable Batteries as Energy Storage solution.....	1
1.3 Li-ion Batteries .....	3
CHAPTER 2 THE PROSPECTIVE CATHODE MATERIALS.....	5
2.1 Power and Energy Densities: .....	8
2.2 Thermal Stability and Safety .....	10
2.3 Environmental and Cost Factors .....	11
2.4 Capacity and Rate-capacity.....	12
2.5 Summary .....	13
CHAPTER 3 AGING MECHANISMS OF ELECTRODE MATERIALS .....	17
3.1 Aging of cathode Material .....	18
3.1.1 Storage .....	19
3.1.2 State of Charge.....	21
3.1.3 Structure and Jahn-Teller Effects.....	23
3.1.4 Lithium ions Diffusion and Particle Size.....	25
3.2 Aging of Anode Material .....	26
3.2.1 SEI layer formation.....	27
3.2.2 Equation of Li Lost versus Time .....	31
CHAPTER 4 DISLOCATION BASED STRESS AND FORCE DEVELOPMENT IN LiFePO <sub>4</sub> MATERIAL.....	33
4.1 Dislocation and Burgers Vector.....	34
4.2 Development of Stress Field Calculation .....	37
CHAPTER 5 LiFePO <sub>4</sub> CATHODE MATERIAL FRACTURE ACCOMMODATED TO DISLOCATION MOVEMENT.....	65
5.1 Dislocation Movement.....	65
5.2 Lithium Ion Diffusion and Dislocation Formation .....	65
5.3 Dislocation based Fracture.....	67

5.3.1 Edge dislocation based mode I fracture .....	67
5.3.2 Edge dislocation based mode II fracture:.....	68
5.3.3 Screw dislocation based mode III fracture: .....	69
CHAPTER 6 CONCLUSION .....	71
REFERENCES .....	73
APPENDICES .....	88
Appendix A: Stress Data at Each Node in FEA Modeling and from Analytical Calculation	89
1. Nodal Element Numbering Chart: .....	89
2. Nodal Coordinates: .....	90
3. Average Nodal Stresses Computed by ANSYS: .....	94
4. Nodal Stress Calculated by Classical Elastic Theory Equation:.....	97
Appendix B: Mathematica Code for Stress and Force Calculation Code.....	100
1. Mathematica code for stress calculation with classical equation (equation 1) for single dislocation in isotropic material.....	100
2. Mathematica code for stress calculation with generalized equation (equation 2) for single dislocation in isotropic material .....	105
3. Mathematica code for stress calculation with generalized equation (equation 2) for single dislocation in anisotropic material .....	112
4. Mathematica code for stress calculation with generalized equation (equation 2) for multiple dislocation in anisotropic material.....	119
5. Mathematica code for force calculation with generalized equation (equation 2) for two dislocation in anisotropic material .....	127

## LIST OF TABLES

### Chapter 2

<b>Table 2.1:</b> Comparison of various cathode materials, $\text{LiCoO}_2$ , $\text{LiMn}_2\text{O}_4$ , $\text{LiNiO}_2$ , and $\text{LiFePO}_4$ , looking at the volumetric power/energy, gravimetric power/energy, density, decomposition temperature, and capacity loss. The capacity is measured as the hourly (dis)charge rate for 100 cycles .....	7
<b>Table 2.2:</b> Volumetric and gravimetric energy density for four different types of Li-ion batteries and the comparison to USABC requirements .....	10
<b>Table 2.3:</b> Thermal stability characteristics and other factors in cost and environmental issues for battery materials.....	12

### Chapter 4

<b>Table 4.1:</b> Anisotropic elastic constants for olivine structure $\text{LiFePO}_4$ material.....	52
---	----

### Appendices

<b>Table A.1:</b> Coordinates of each node.....	90
<b>Table A.2:</b> Average Nodal Stresses Computed by ANSYS.....	94
<b>Table A.3:</b> Nodal Stress Calculated by Classical Elastic Theory Equation.....	97

## LIST OF FIGURES

### Chapter 1

- Figure 1.1:** The most common Li-ion battery applications in the market are for portable electronics, power tools, and transportation ..... 2
- Figure 1.2:** Electrochemical processes in lithium-ion batteries during charging and discharging..... 3

### Chapter 2

- Figure 2.1:** Three categories of host structures: (a) the layered  $\text{LiMO}_2$  with 2D lithium ion diffusion pathway (such as  $\text{LiCoO}_2$  and  $\text{LiNiO}_2$ ); (b) the  $\text{LiMn}_2\text{O}_4$  spinels with 3D lithium ion diffusion pathway; and (c) the  $\text{LiFePO}_4$  with 1D lithium ion diffusion channel..... 6
- Figure 2.2:** Comparison of various cathode materials,  $\text{LiCoO}_2$ ,  $\text{LiMn}_2\text{O}_4$ ,  $\text{LiNiO}_2$ , and  $\text{LiFePO}_4$ , looking at the volumetric power/energy, gravimetric power/energy, density, decomposition temperature, and capacity loss. The capacity is measured as the hourly (dis)charge rate for 100 cycles..... 15

### Chapter 3

- Figure 3.1:** Electrode aging/degradation categories based on different causes and influences ..... 18
- Figure 3.2:** The different electron losing ratio obtained by Vegard's Law and Mossbauer spectroscopy method indicates that the loss of active material occurred ..... 20
- Figure 3.3:** Reactions related to soluble Mn ions (Vetter, 2005)..... 22
- Figure 3.4:** (a) Eight  $\text{LiFePO}_4$  unit cells without dislocations where lithium ions lay in the spaces along the b(y)-direction. (b) A  $\text{FeO}_6$  octahedron and five  $\text{PO}_4$  tetrahedra connect each other by sharing one edge and three corners..... 23
- Figure 3.5:** An schematic diagram for Jahn-Teller effect..... 25
- Figure 3.6:** Formation, growth, and failure of SEI layers (Vetter, 2005) ..... 28
- Figure 3.7:** Examples of capacity evolutions during 100% DOD cycling..... 29
- Figure 3.8:** Mechanism of Li deposit..... 30

## Chapter 4

<b>Figure 4.1:</b> (a) edge dislocation and (b) screw dislocation .....	34
<b>Figure 4.2:</b> Determine the Burgers vector by drawing rectangular. (a) edge dislocation; (b) screw dislocation.....	36
<b>Figure 4.3:</b> (a) Determine Burgers vector by PLM/AFM photo. (b) determine Burgers vector by XRD picture.....	37
<b>Figure 4.4:</b> Observed cracks in LiFePO <sub>4</sub> particles from SEM images (Chen, 2006) .....	39
<b>Figure 4.5:</b> HRTEM image of the disordered region at the end of the crack in Fig.4, with Fourier transforms of the indicated areas. (Chen, 2006) .....	39
<b>Figure 4.6:</b> A LiFePO <sub>4</sub> crystal model with an infinite length edge dislocation. Edge dislocation is along $z$ -direction ( $c$ -direction) .....	40
<b>Figure 4.7:</b> Distortion zone between LFP phase and FP phase (Delmas, 2008).....	40
<b>Figure 4.8:</b> (a) FEA Model for our dislocation problem. (b) dislocation problem in larger scale.....	46
<b>Figure 4.9:</b> Dislocation stress distribution plot in LiFePO <sub>4</sub> material with isotropic property and classical equations (model A) .....	46
<b>Figure 4.10:</b> (a) Plot of stresses $\sigma$ -xx calculated by classical equation and ANSYS model. (b) Numerical difference between two sets of stress data (Equation - ANSYS).....	47
<b>Figure 4.11:</b> (a) Plot of stresses $\sigma$ -yy calculated by classical equation and ANSYS model. (b) Numerical difference between two sets of stress data (Equation - ANSYS).....	48
<b>Figure 4.12:</b> (a) Plot of stresses $\tau$ -xy calculated by classical equation and ANSYS model. (b) Numerical difference between two sets of stress data (Equation - ANSYS).....	49
<b>Figure 4.13:</b> Comparison of stress distribution graphs from ANSYS and analytical equation .....	51
<b>Figure 4.14:</b> Flow chart of stress distribution plotting: from converting elastic constants to choosing modeling equations. Red: classical equation with isotropic property; purple: generalized equation with isotropic property; green: generalized equation with anisotropic property.....	54
<b>Figure 4.15:</b> The stress field for edge and screw dislocations. (a) Stress distribution calculated via classical solutions for a single edge dislocation with isotropic materials property. (b) & (c) Stress distribution calculated via generalized solutions for a single edge dislocation with isotropic and anisotropic materials property, respectively. (d) & (e) Stress distribution for varied Burger's vector directions where generalized solutions for a single edge dislocation with anisotropic materials property are adapted. (f) Stress distribution calculated via classical solutions for a single screw dislocation with isotropic materials property. (g) & (h) Stress distribution calculated via generalized solutions for a single screw dislocation with isotropic and anisotropic material properties, respectively .....	56

**Figure 4.16:** Representative multiple edge dislocation distributions in  $\text{LiFePO}_4$  crystals. For dislocation number 1, the Burger's vectors is varied from  $(b_x=1, b_y=0)$  in (a) to  $(b_x=0, b_y=0.6)$  in (b). Dislocation number 2 is fixed in its direction ..... 57

**Figure 4.17:** Stress field for multiple edge and screw dislocations. (a) The stress field on the ab-plane is calculated by varying Berger's vector directions of dislocation 1 when dislocation 2 is fixed in its direction, where the Burger's vector of dislocation 1 is  $(b_x=1, b_y=0)$ . (b) The stress distribution between two edge dislocations for which the Berger's vector of dislocation 1 is  $(b_x=1, b_y=0.6)$ . (c) The stress distribution between two edge dislocations for which the Berger's vector of dislocation 1 is  $(b_x=0, b_y=0.6)$ . (d) The stress distribution between two screw dislocations for which the Berger's vector of dislocation 1 is  $(b_z=0.47)$  ..... 59

**Figure 4.18:** The force field of dislocation interactions. The force field changes due to the direction of dislocation 2. (a) and (e):  $b_x=1, b_y=0$ ; (b) and (f):  $b_x=1, b_y=0.6$ ; (c) and (g):  $b_x=0, b_y=0.6$ ; (d) and (h):  $b_x=-1, b_y=0$ . Equal and opposite forces act on dislocation 1. Warm color represents positive force, which means it push/pull the dislocation towards positive direction of x/y axis, and vice versa ..... 63

## Chapter 5

**Figure 5.1:** (a)  $\text{LiFePO}_4$  crystal structure of eight unit cells. (b) Lithium ions diffusion along the b-direction in  $\text{LiFePO}_4$  material during the discharging process (fill the crystal layer by layer in the a-direction) ..... 66

**Figure 5.2:** (a) Kinetics of the formation of the [100] edge dislocation and (010) glide plane in  $\text{LiFePO}_4$  crystal during Lithium ions diffusion. (b) Mechanism of the dislocations gliding resulting in a crack surface normal to (010) where a crack line is parallel to (001). (c) Mode I fracture caused by the accumulated dislocations. .... 68

**Figure 5.3:** (a) Kinetics of the formation of the [010] edge dislocation and (100) glide plane in  $\text{LiFePO}_4$  crystal during Lithium ions diffusion.  $\text{LiFePO}_4$  crystal might be filled with lithium ions inhomogeneously. (b) Mechanism of the dislocations gliding resulting in a crack surface normal to (010) where a crack line is parallel to (001). (c) Mode II fracture caused by the accumulated dislocations. .... 69

**Figure 5.4:** (a) Kinetics of the formation of the [001] screw dislocation and (100) glide plane in  $\text{LiFePO}_4$  crystal during Lithium ions diffusion.  $\text{LiFePO}_4$  crystal might be filled with lithium ions inhomogeneously. (b) Mechanism of the dislocations gliding resulting in a crack surface normal to (010) where a crack line is parallel to (001). (c) Mode II fracture caused by the accumulated dislocations ..... 70

## Appendices

<b>Figure A.1:</b> Nodal numbering of the ANSYS model -- entire part.....	89
<b>Figure A.2:</b> Nodal numbering of the ANSYS model – the core area (circled area in figure (A.1)).....	90

## **CHAPTER 1 INTRODUCTION**

### **1.1 The Needs for Alternative Energy Solution**

For over a century, petroleum-derived fuels have been the first choice as an energy source for transportation, and accounted for more than 71.4% of U.S. petroleum use in 2009 [1]. Although petroleum-based fuel energy resources are convenient and technically mature, researchers started looking for alternative energy sources such as batteries due to the shortage of petroleum and because burning fossil fuels has become an environmental issue. It is reported that 98% of carbon dioxide emissions come from petroleum fuels [2]. Since carbon dioxide accounts for the largest share of greenhouse gases, to meet the stated goal of reducing total U.S. greenhouse gas emissions to 83% below 2005 levels by 2050, an alternative energy storage system is required.

### **1.2 Rechargeable Batteries as Energy Storage solution**

One of the most promising energy storage solutions for future automotive technology is the rechargeable battery. Compared with other resources such as flywheels, capacitors, biofuel, solar cells, and fuel cells, rechargeable batteries are more portable and provide quick energy storage and release [3-5]. Moreover, it is more difficult to use these other resources globally than it is to use rechargeable batteries, due to the operating environment limitations

for these other energy sources [5]. Compared with capacitors, rechargeable batteries have lower self-discharge rates [4, 5], thus holding their charge for longer periods of time.

Therefore, to best serve as a future automotive technology, rechargeable batteries should have both high energy and power densities [3], the ability to output high current for a long period of time, and to be fully charged quickly. The durability and environmental friendliness of rechargeable batteries is also very important. They should safely work for several years under different climatic conditions, even if involved in an unfortunate car collision. Among the rechargeable batteries, Li-ion batteries have dominated the field of advanced power sources due to their high gravimetric and volumetric energy density [6]. The most common Li-ion battery applications in the market are for portable electronics, power tools, and transportation (Figure 1.1).



**Figure 1.1:** The most common Li-ion battery applications in the market are for portable electronics, power tools, and transportation

### 1.3 Li-ion Batteries

Li-ion battery contains three main parts: the cathode, the anode, and the electrolyte (Fig. 1). It operates via an electrochemical process in which lithium ions are shuttled between cathode and anode while electrons flow through an external wire to form an electrical circuit. During discharge, an electrical circuit is formed, and lithium ions move out (extraction) from the anode to the cathode (intercalation) to neutralize these charges (Figure 1.2). The reactions occur continuously and while electrons continue to flow, providing electrical energy to the connected device. The electrical energy is then restored to the battery upon recharge.

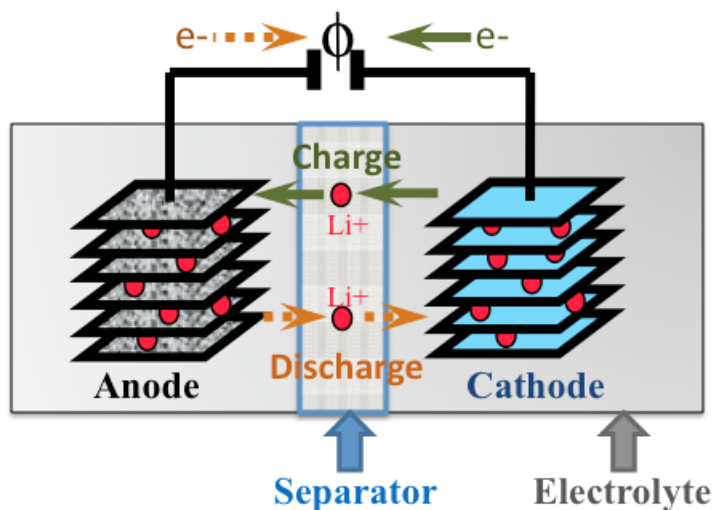


**Figure 1.2:** Electrochemical processes in lithium-ion batteries during charging and discharging.

Both anode and cathode materials exhibit layered structures, which allow lithium ions to stay in or pass through the structures. On the cathode side, intercalated lithium compound such as  $\text{LiFePO}_4$ ,  $\text{LiMn}_2\text{O}_4$ , and  $\text{LiCoO}_2$  are commonly used. On the anode side, layered carbon materials (graphite or carbon nanotube) [7, 8], titanate materials [9], or silicon nanowires [10] are widely used due to their low electrochemical potential with respect to Li metal [11]. The most common electrolyte is a solution that contains lithium salt in an organic solvent. To avoid unnecessary reactions between electrode materials and  $\text{H}/\text{H}_2$  or  $\text{O}_2/\text{H}_2\text{O}$  in the electrolyte, an organic solvent or organic solid were adopted to replace the aqueous solvent [11]. The current collectors, connecting to the anode and cathode, carry electrons and transmit the current to the external circuit. The separator is a membrane that lies between the anode and cathode to avoid the possibility of short circuit (Figure 1.2).

In following work, I provide an overview of commonly used cathode materials for Li-ion rechargeable batteries. I will also discuss our previous works on dislocation-based stress fields and provide stress distributions in  $\text{LiFePO}_4$  cathode materials.

## CHAPTER 2 THE PROSPECTIVE CATHODE MATERIALS

Four mainstream cathode materials on the present market are compared:  $\text{LiCoO}_2$ ,  $\text{LiMn}_2\text{O}_4$ ,  $\text{LiNiO}_2$ , and  $\text{LiFePO}_4$ . The four materials fall in three categories of host structures: the layered  $\text{LiMO}_2$  with 2D lithium ion diffusion pathway (such as  $\text{LiCoO}_2$  and  $\text{LiNiO}_2$ ) (Figure 2.1(a)), the  $\text{LiMn}_2\text{O}_4$  spinels with 3D lithium ion diffusion pathway (Figure 2.1(b)), and the  $\text{LiFePO}_4$  with 1D lithium ion diffusion channel (Figure 2.1(c)) [12, 13].  $\text{LiCoO}_2$  is in a layered structure in which the  $\text{Li}^+$  and  $\text{Co}^{3+}$  ions appear on the (111) planes alternatively. The layer sequence is -O-Li-O-Co-O-, and the stacking sequence is ABCABC. Li ions lay between  $\text{CoO}_2$  layers and could diffuse from/into the layer structure during charging/discharging process [14].  $\text{LiCoO}_2$  is the most commonly used in portable electronic devices due to its excellent charging/discharging rate and power/energy density [15]. However, only 50% lithium ions could diffuse between cathode and anode reversible during charging/discharging, which means the capacity of battery in application could only reach 50% of its theoretical capacity [14]. Also, a battery with  $\text{LiCoO}_2$  as its cathode material does not have good thermal stability [16]. Moreover, cobalt is toxic and expensive, which makes  $\text{LiCoO}_2$  an imperfect choice for a cathode material for electric vehicles (EVs), hybrid electric vehicles (HEVs), and plug-in hybrid electric vehicles (PHEVs), although it is widely used in portable devices.  $\text{LiMn}_2\text{O}_4$ , with a 3-dimensional spinel structure, is able to provide higher voltage, but it does not have a good power/energy density [17]. Due to Jahn-Teller distortion effect and Mn dissolution phenomenon during cycling, the capacity of this material fades very fast [12, 18, 19]. Its relatively short cycle life and high capacity loss [20] indicate that it

is not an ideal cathode material for Li-ion batteries for EV/HEV/PHEV applications. The  $\text{LiNiO}_2$  material, with the same structure as  $\text{LiCoO}_2$ , has more reversible Li ions (65%) [14], and provides good power and energy densities [21]. However, it is difficult to order  $\text{Li}^+$  and  $\text{Ni}^{3+}$  in  $\text{LiNiO}_2$ . Since it is very difficult to prepare pure  $\text{LiNiO}_2$  composite, Co-doped  $\text{LiNiO}_2$ ,  $\text{Li}_{1-x}(\text{Ni}_{0.8}\text{Co}_{0.2})_{1+x}\text{O}_2$ , is usually considered as an alternative material in research and other applications [22]. Another disadvantage of this material is that the impedance would increase when temperature rises [23].

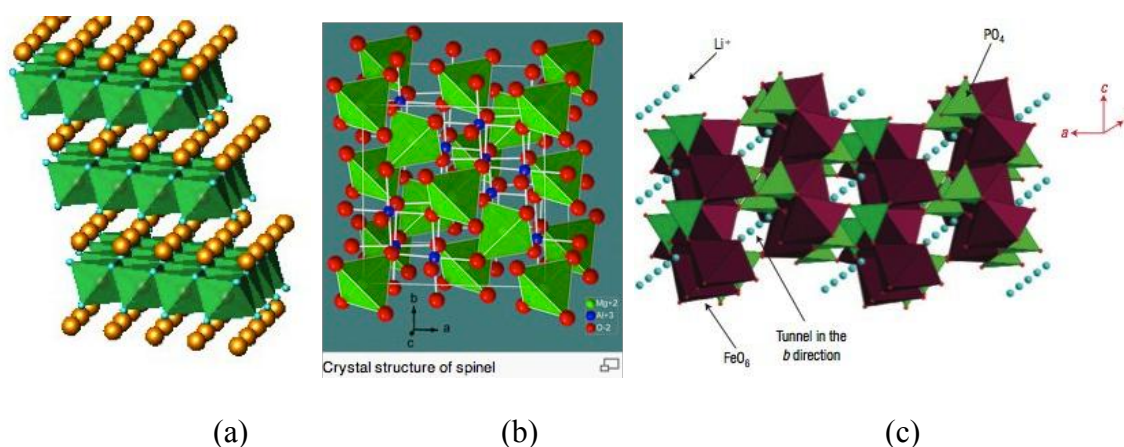


**Figure 2.1:** Three categories of host structures: (a) the layered  $\text{LiMO}_2$  with 2D lithium ion diffusion pathway (such as  $\text{LiCoO}_2$  and  $\text{LiNiO}_2$ ); (b) the  $\text{LiMn}_2\text{O}_4$  spinels with 3D lithium ion diffusion pathway; and (c) the  $\text{LiFePO}_4$  with 1D lithium ion diffusion channel.

With the demand for Li-ion batteries increasing worldwide, an alternative Li-ion battery cathode material, olivine structure  $\text{LiFePO}_4$ , was developed by Goodenough in 1996 [13]. The charging/discharging process of this material is a two phase reaction that olivine host  $\text{FePO}_4$  allows a reversible insertion of Li to  $\text{LiFePO}_4$ . He and his group also discovered that  $\text{LiFePO}_4$  is a good candidate for a cathode material due to its low price, high thermal

stability, and flat discharge voltage ( $\sim 3.6\text{V}$  versus  $\text{Li}^+/\text{Li}^0$ ). However, the two-phase insertion reaction limits the electronic and ionic conductivity and therefore the rate capacity where the cathode particles are too large [24-26].  $\text{LiFePO}_4$  suffers from low intrinsic electronic conductivity ( $10^{-10}$ – $10^{-9}$  S/cm) [27]. Based on the study by Chung and Chiang [28], the low electronic conductivity of  $\text{LiFePO}_4$  could be significantly enhanced by doping other metal elements such as zirconium, niobium, and magnesium [28]. It could also be solved by coating the particles with carbon [29] or other Li-permeable phase [30]. Characteristics and specifications of the aforementioned cathode materials were collected and compared for Li-ion batteries (Table 2.1). Specifically, I focus on (1) volumetric power and energy densities, (2) gravimetric power and energy densities, (3) stability, safety and environmental factors, and (4) capacity and rate-capacity. Since synthetic methods are different for the four different cathode materials, only the representative data that appeared most frequently within the past five years were chosen to ensure that data from different literature sources are comparable.

**Table 2.1:** Comparison of various cathode materials,  $\text{LiCoO}_2$ ,  $\text{LiMn}_2\text{O}_4$ ,  $\text{LiNiO}_2$ , and  $\text{LiFePO}_4$ , looking at the volumetric power/energy, gravimetric power/energy, density, decomposition temperature, and capacity loss. The capacity is measured as the hourly (dis)charge rate for 100 cycles.

	$\text{LiCoO}_2$	$\text{LiMn}_2\text{O}_4$	$\text{LiNiO}_2$	$\text{LiFePO}_4$
Capacity Loss (percentage 100 cycle@1C)	85	90	N/A	92
Decomposition Temp ( °C)	340	275	250	950
Density (10g/L)	500	410	478	220
Gravimetric Energy (Wh/kg)	532	440	629	495
Gravimetric Power (W/kg)	680	584	600	600
Volumetric Energy (Wh/L)	483	785	N/A	970
Volumetric Power (W/L)	767	900	N/A	1236

## 2.1 Power and Energy Densities:

Power and energy densities are important properties for cathode materials. They determine the energy release rate and energy storage capacity per unit weight or volume. For electric vehicles, the volumetric power density and energy density are very important, because with the same energy capacity, a smaller battery is easier to fit into a car. For battery cathode materials, it is observed that  $\text{LiFePO}_4$  has the highest volumetric power density and energy density (1236 W/L, 970 Wh/L, respectively) among the four mainstream cathode materials [31, 32] (Table 2.1).  $\text{LiCoO}_2$  has a volumetric power density of around 767 W/L and an energy density of around 483 Wh/L. These values are roughly half that of  $\text{LiFePO}_4$  [31, 32] (Table 2.1).  $\text{LiMn}_2\text{O}_4$  has a volumetric power density and energy density (900 W/L, 785 Wh/L) higher than those of  $\text{LiCoO}_2$ . However,  $\text{LiMn}_2\text{O}_4$  has a slightly lower volumetric power density and energy density than that of  $\text{LiFePO}_4$  [31, 32] (Table 2.1). The volumetric power and energy density data of  $\text{LiNiO}_2$  were not available since pure  $\text{LiNiO}_2$  is difficult to prepare.

In addition, the United States Advanced Battery Consortium (USABC) listed goals for advanced batteries for EVs where volumetric power density should at least be 600 W/L and the volumetric energy density should be at least 300 Wh/L [33] (Table 2.2). Considering batteries as a whole (including cathode, anode, and electrolyte), current battery technologies, however, are only able to deliver 250-360 Wh/L for  $\text{LiCoO}_2$  batteries, 330 Wh/L for  $\text{LiMn}_2\text{O}_4$  batteries, 450 Wh/L for  $\text{LiNiO}_2$  batteries, and 220 Wh/L for  $\text{LiFePO}_4$  batteries. Therefore, the performance of advanced batteries still falls short of the EV goals set forth in

2006 by the USABC [33]. Note that the values reported in Table 2.1 are based on raw materials and the values reported in Table 2.2 are batteries as a whole (including cathode, anode, and electrolyte) with the said cathode materials.

The gravimetric power and energy densities are very important for portable devices. That is, with the same power and energy capacity, a lighter battery is easier to carry [32, 34, 35]. It is observed that  $\text{LiNiO}_2$  has high gravimetric power and energy densities of 600 W/kg and 629 Wh/kg, respectively (Table 2.1). The gravimetric power density of  $\text{LiFePO}_4$  is reported around 600 W/kg whereas its gravimetric energy density (495 Wh/kg) is lower than that of  $\text{LiNiO}_2$ .  $\text{LiCoO}_2$  has a gravimetric power density of around 680 W/kg and an energy density of around 532 Wh/kg. These values are slightly higher than those of  $\text{LiFePO}_4$  [32, 34, 35] (Table 2.1). Finally,  $\text{LiMn}_2\text{O}_4$  has a gravimetric power density of around 584 W/kg and an energy density of around 440 Wh/kg. These values are comparable to that of  $\text{LiFePO}_4$  [32, 34, 35] (Table 2.1). The density of each cathode material was also listed in Table 2.1.  $\text{LiFePO}_4$  has the lowest density (2.2 kg/L) and  $\text{LiCoO}_2$  has the highest (5 kg/L), which is more than twice of that of  $\text{LiFePO}_4$ .

Gravimetric power/energy densities should not be directly converted to volumetric power/energy densities based on the provided density values. This is due to the different synthetic methods that were chosen based on different demands, and the weight of electrolytes was sometimes included in the collected data when the gravimetric power and energy densities were calculated. According to the USABC, gravimetric power density should at least be 400 W/kg and the gravimetric energy density should at least be 200 Wh/kg [33] (Table 2.2). However, considering batteries as a whole (including cathode, anode, and

electrolyte), current battery technologies are only able to deliver 106-250 Wh/kg for LiCoO<sub>2</sub> batteries, 100 Wh/kg for LiMn<sub>2</sub>O<sub>4</sub> batteries, 192 Whkg<sup>-1</sup> for LiNiO<sub>2</sub> batteries, and 90-110 Wh/kg for LiFePO<sub>4</sub> batteries. Therefore, the performance of advanced batteries falls short of EV goals set forth in 2006 by the USABC [33].

**Table 2.2:** Volumetric and gravimetric energy density for four different types of Li-ion batteries and the comparison to USABC requirements.

Energy Density	LiCoO <sub>2</sub>	LiMn <sub>2</sub> O <sub>4</sub>	LiNiO <sub>2</sub>	LiFePO <sub>4</sub>	USABC
Gravimetric (Wh/kg)	180	100	170	130	200
Volumetric (Wh/L)	305	330	450	220	300

## 2.2 Thermal Stability and Safety

The safety issue for Li-ion batteries is an important factor that determines potential applications, especially for EV/HEV/PHEV and other electronic devices. Battery safety is determined primarily by the material's thermal stability, and the reported overheating and explosion of Li-ion batteries is mainly due to a battery's thermal instability [36]. The differential scanning calorimetry (DSC) test is widely used to investigate the exothermic or endothermic reaction for composite explosives. It determines the ability of a material to absorb or release heat during electrochemical reactions such as lithium insertion or extraction in Li-ion batteries. By using DSC testing, Xia et al. [37] collected the thermal activity and predicted the resultant thermal stability for different cathode materials. They observed that

LiFePO<sub>4</sub> has the lowest exothermic peak temperature (289°C) and exhibited endothermic heat flow (-6 W/g). That is, during electrochemical reactions, LiFePO<sub>4</sub> will see smaller temperature increases than the other three cathode materials. Moreover, it is observed that LiMn<sub>2</sub>O<sub>4</sub> has an exothermic peak at 302°C, which can easily be reached during a car accident. LiCoO<sub>2</sub> and LiNiO<sub>2</sub> also release heat and cause overheating or even explosions at higher temperatures of around 300-400°C, suggesting that LiCoO<sub>2</sub> and LiNiO<sub>2</sub> as cathode materials are an undesirable choice for energy storage systems for EV/HEV/PHEV applications. In contrast, the electrochemical reaction of LiFePO<sub>4</sub> is endothermic, suggesting that LiFePO<sub>4</sub> is a safer battery material. In general, exothermic peak temperature can be used as a description of the self-reaction temperature. The lower the peak temperature, the safer a material is. The decomposition temperature also indicates that LiFePO<sub>4</sub> (950°C) has much higher thermal stability than any other material (Table 2.1). The decomposition temperatures for LiCoO<sub>2</sub>, LiMn<sub>2</sub>O<sub>4</sub>, and LiNiO<sub>2</sub> are 340°C, 275°C, and 250°C, respectively (Table 2.1) [37]. The excellent thermal stability of LiFePO<sub>4</sub> is due to strong covalent P-O bonds in the (PO<sub>4</sub>)<sup>3-</sup> polyanionic clusters [38].

### **2.3 Environmental and Cost Factors**

In addition to the safety issue, I also compared the cost of cathode materials and environmentally-related factors (Table 2.3). It could be noted that cobalt is toxic and nickel has the potential to cause heavy metal pollution. LiFePO<sub>4</sub> is made from non-toxic materials and the transition metal is abundant (160 billion tons in the Earth). As a result, batteries

made from this type of cathode material could be relatively cheaper than those made of  $\text{LiCoO}_2$  since the transition metal storage of  $\text{LiCoO}_2$  is approximately 8.3 million tons (0.005% of  $\text{LiFePO}_4$ ). The transition metal storage of  $\text{LiMn}_2\text{O}_4$  and  $\text{LiNiO}_2$  are 99.7 million and 48 billion tons, respectively. It is suggested that  $\text{LiFePO}_4$  as a cathode material for rechargeable batteries is more environmental friendly and cost effective than the other three cathode materials (Table 2.2).

**Table 2.3:** Thermal stability characteristics and other factors in cost and environmental issues for battery materials.

	$\text{LiCoO}_2$	$\text{LiMn}_2\text{O}_4$	$\text{LiNiO}_2$	$\text{LiFePO}_4$
Exothermic heat flow ( $\text{Wg}^{-1}$ )	20	7	33	-6
Exothermic peak temperature ( $^\circ\text{C}$ )	367	302	348	289
Storage of transition metal ( $\times 10^6$ ton)	8.3	99.7	48000	160000
Battery cost	expensive	moderate	cheap	cheap
Environmental pollution	toxic Co	good	heavy metal Ni	good

## 2.4 Capacity and Rate-capacity

The capacity of a battery is the amount of charge available expressed in milliampere-hours (mAh), and it depends on discharge conditions such as the magnitude of the current, the voltage of the battery, temperature, and other factors. Rate-capacity loss after thousands of cycles is one of the biggest obstacles for advanced rechargeable battery technology. To

better examine the rate-capacity, four mainstream cathode materials were compared for their retained capacity. The retained capacity of cathode materials is measured after a certain amount of cycles at an  $nC$  discharge rate, where a rate  $nC$  corresponds to a full discharge in  $1/n$  hours. For example,  $0.25C$  is the rate at which a battery is totally discharged in 4 hours. The higher the value of the rate  $nC$ , the better the energy output ability of the battery material is. Studies showed that after 100 cycles at  $1C$ -rate discharging,  $\text{LiFePO}_4$  processes 92% capacity retention,  $\text{LiMn}_2\text{O}_4$  processes 90%, and  $\text{LiCoO}_2$  processes 85% capacity retention, respectively [7] (Table 2.1). By extrapolation, if the capacity retention is measured under a higher rate ( $n > 1$ ),  $\text{LiFePO}_4$  has a better capability to maintain rate-capacity than do other cathode materials. Since the preparation and synthetic methods for  $\text{LiNiO}_2$  are extremely difficult, its capacity retention data is unavailable. Nevertheless, the rate-capacity loss of  $\text{LiFePO}_4$  is reported after thousand-cycles high-rate discharging [39, 40]. It is observed that under a high discharge rate, the capacity retention rate of  $\text{LiFePO}_4$  batteries is not as good as that of other batteries.

## 2.5 Summary

So far I provide an overview of four mainstream lithium-ion battery cathode materials. Characteristics of  $\text{LiCoO}_2$ ,  $\text{LiMn}_2\text{O}_4$ ,  $\text{LiNiO}_2$ , and  $\text{LiFePO}_4$  were collected and compared. Base on the data above, a chart could be drawn to make the comparison more clear (Figure 2.2). The first four rows of bars from behind represent the gravimetric and volumetric energy and power densities. From the figure, it could be stated that the gravimetric energy and

power densities of  $\text{LiFePO}_4$  is in the same level as the rest materials. And the volumetric energy and power densities of  $\text{LiFePO}_4$  is higher than the rest of materials. The green bars represent the physical densities of four materials. The density of  $\text{LiFePO}_4$  is about half as that of the rest three materials. A material with lower density has the potential of being made to lighter weight battery, which is good for electrical vehicle. The red bars, which indicate the decomposition temperature, shows that the  $\text{LiFePO}_4$  could remain steady at very high temperature (over  $900^\circ\text{C}$ ) while the other three materials decompose at relative low temperature (about  $350^\circ\text{C}$ ) which could be easily reached in a car accident. Also, according to table 2.3, the  $\text{LiFePO}_4$  material is nontoxic, cheap, and abundant on earth.

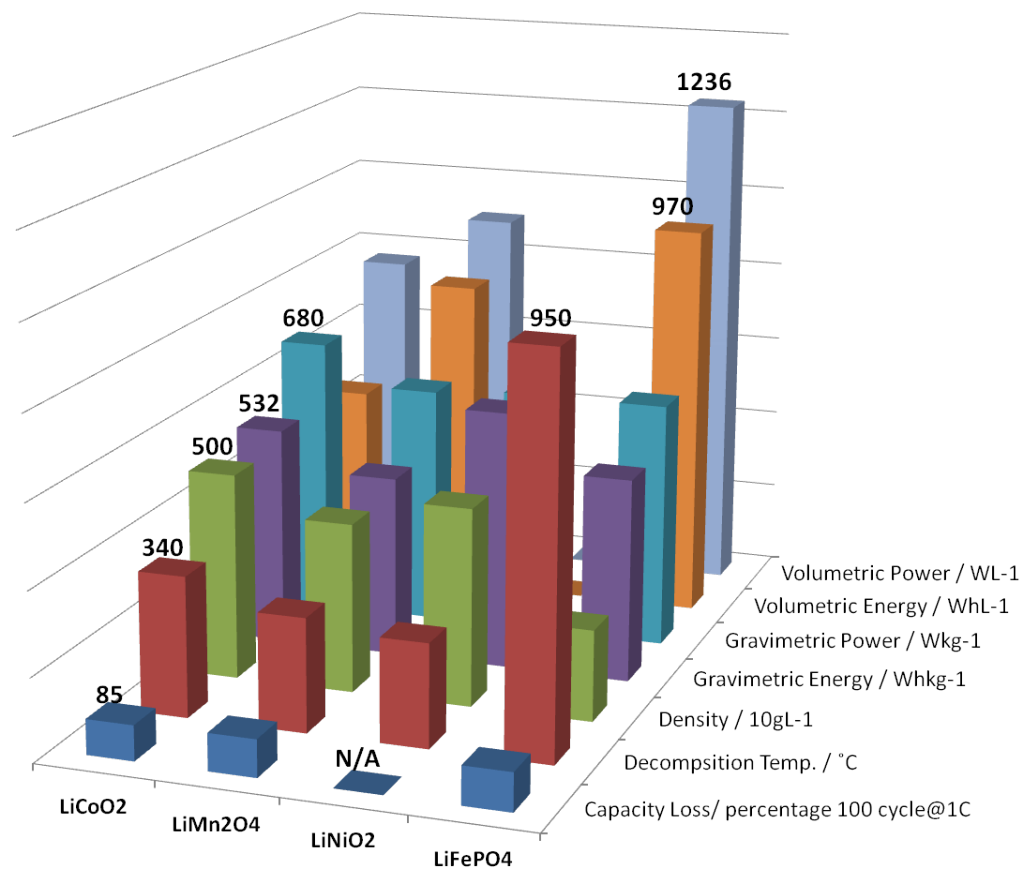


**Figure 2.2:** Comparison of various cathode materials,  $\text{LiCoO}_2$ ,  $\text{LiMn}_2\text{O}_4$ ,  $\text{LiNiO}_2$ , and  $\text{LiFePO}_4$ , looking at the volumetric power/energy, gravimetric power/energy, density, decomposition temperature, and capacity loss. The capacity is measured as the hourly (dis)charge rate for 100 cycles.

From above, I could safely reach the conclusion that  $\text{LiFePO}_4$  has the potential to become a better cathode material due to its combination of several superior properties for most common usage. The advantages of  $\text{LiFePO}_4$  are: Relatively good energy/power density, light weight, raw materials are cheap and abundant, high thermo stability, and friendly to environment. However, there are also some disadvantages for  $\text{LiFePO}_4$  material such as: low

electron conductivity, and high capacity loss rate under high discharging rate. To solve the above problems, researchers are trying to optimize its properties during the preparation. The most commonly used methods developed by MIT researchers are: carbon coating, doping the transition metal material, and minimizing the material into nano-size. Those methods solved the problem of low conductivity. But the high capacity loss rate, which is related to complicated aging mechanism, is still need to be solved.

In conclusion, current electrochemical technology is still limited to developing cathode materials to achieve EV goals set by the USABC. And the main obstacle for advanced rechargeable batteries is found in the rate-capacity loss at high C-rate discharging. It is currently one of the most challenging issues in developing energy storage systems for EV/HEV/PHEV, and the enhancement of rate-capacity retention is the primary design goal of battery chemistry in the electrochemical community. The goal of my research is to learn the mechanism of aging process and rate-capacity loss of  $\text{LiFePO}_4$  material, and try to build up a model of structural aging mechanism. To start my research, I need to begin with learning the aging mechanisms of common electrode materials:

## **CHAPTER 3 AGING MECHANISMS OF ELECTRODE**

### **MATERIALS**

Electrode failures in Li-ion batteries are usually a result of the accumulation of aging or degradation, which affect the ability of electrodes to hold charge, and result in capacity loss in Li-ion batteries, and the mechanism can be categorized based on storage/cycling or chemical/mechanical activities. For anode materials, the aging/degradation mechanism is primarily determined by the development of a solid-electrolyte interphase (SEI) film [41]; it is a chemical reaction. For cathode materials, the aging/degradation mechanisms could be categorized into two groups: (1) ones that cause the loss of active material via storage and cycling, such as the chemical interaction of aging products with anodes, oxidation of electrolyte components, and surface film formation [39, 42-45], and (2) ones that increase the battery impedance or decrease the output voltage, such as structural changes, electrode components changes, or materials degradation [46-48] (Figure 3.1). In general, the aforementioned four phenomena do not happen alone and the mechanism of electrode failure is caused by several factors taking place at the same time, which makes it more complicated.

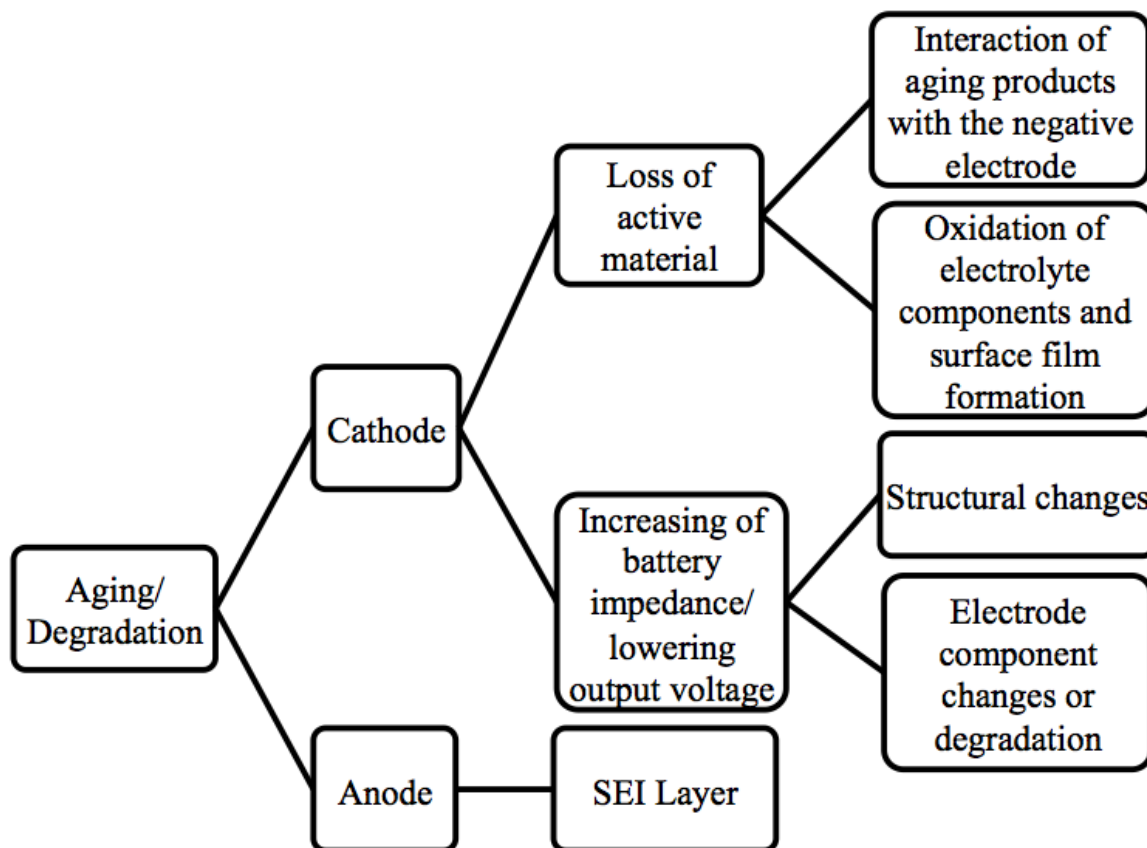


**Figure 3.1:** Electrode aging/degradation categories based on different causes and influences. The proposed work focuses on understanding the interplay between structural changes and deterioration in  $\text{LiFePO}_4$  cathode material.

### 3.1 Aging of cathode Material

Cathode materials are considered to be the vital part of Li-ion batteries since cathode materials affect both performance and cycling life in Li-ion batteries. Since the aging/degradation mechanism of cathode materials is much more complicated than that of

anode materials, and since there are varieties of electrode materials, it is difficult to provide a general explanation for cathode aging/degradation mechanisms in all Li-ion systems. In this part, I focus on basic factors such as storage, state of charge, and the Jahn-Teller effect.

While storing electrode materials, aging/degradation usually occurs because of side reactions due to the thermodynamic instability of the materials [49-52]. Moreover, the state of charge, cycling conditions, and temperature are three main factors that cause materials to age/degrade. Finally, cycling with kinetically-induced effects, such as volume variations and concentration gradients, could potentially result in capacity loss in Li-ion batteries.

### **3.1.1 Storage**

As a cathode material for Li-ion batteries,  $\text{LiFePO}_4$  is presently a promising green material because of its low cost, non-toxicity, rich source of raw materials, and great electrochemical performance [53]. Yet, although commonly considered to be highly stable toward air and  $\text{H}_2\text{O}$ , aging/degradation of the electrochemical performance of  $\text{LiFePO}_4$  was shown after being exposed to air for a few weeks at ambient temperature [54]. To observe the side reaction and side phase of  $\text{LiFePO}_4$  materials in an atmosphere of humid hot air, a nanoscaled sample of  $\text{LiFePO}_4$  material (70 nm) in  $120^\circ\text{C}$  hot air was stored for 30 days. By comparing it with a pristine sample under the X-ray Diffraction (XRD) test, the decreasing unit-cell volume after storing at high temperature was observed, suggesting that the delithiation occurred with hot air [55]. In a parallel study to the XRD test, the decreased unit-cell volume is calculated based on Vegard's Law, which is equivalent to 11% lithium missing

during the high temperature storage. Moreover, the amount of  $\text{Fe}^{3+}$  determined by Mossbauer spectroscopy accounts for 45% of total iron, which is far more than the 11% loss of lithium (Figure 3.2). This phenomenon indicates that while storing, in addition to the trivalent Fe from delithiation, an amorphous ferric phosphate side-phase grows detrimentally to the olivine  $\text{LiFePO}_4$  upon air exposure. Therefore, this loss of active material in  $\text{LiFePO}_4$  cathodes could potentially lead to capacity loss in Li-ion batteries.

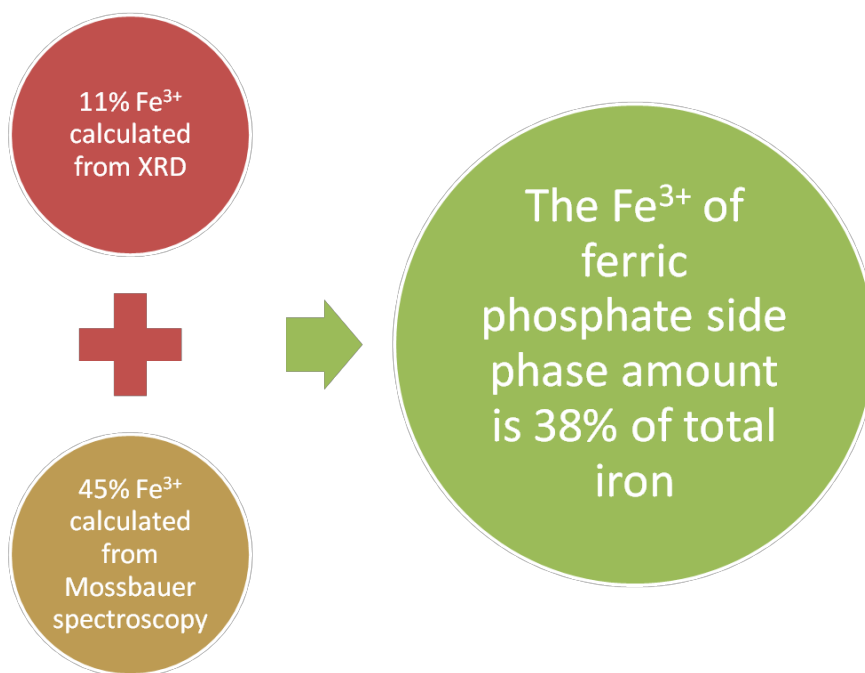


**Figure 3.2:** The different electron losing ratio obtained by Vegard's Law and Mossbauer spectroscopy method indicates that the loss of active material occurred.

### 3.1.2 State of Charge

In current EV/HEV/PHEV markets,  $\text{LiMn}_2\text{O}_4$  has been adopted as the cathode material for Li-ion batteries [56]. The  $\text{LiMn}_2\text{O}_4$  cathode material provides higher voltage than other materials, but its usage is limited by its short cycle life [20, 57, 58]. It is observed that the accelerated aging/degradation of  $\text{LiMn}_2\text{O}_4$  cathode materials is due to the dissolution of Mn in electrolyte under various charging voltages: with a charging voltage higher than 4.2V or when nearly fully discharged. During a very low state of charge or at a high temperature ( $55^\circ\text{C}$ ), a disproportionation reaction will occur, which consumes two  $\text{Mn}^{3+}$  at two Mn sites in  $\text{LiMn}_2\text{O}_4$  cathode materials while  $\text{Mn}^{3+}$  converts to  $\text{Mn}^{2+}$  and  $\text{Mn}^{4+}$  [20, 41, 58].



The  $\text{Mn}^{4+}$  stays in one of the two Mn sites and takes the place of  $\text{Mn}^{3+}$ .  $\text{Mn}^{2+}$  ions, on the other hand, escape from the  $\text{LiMn}_2\text{O}_4$  and dissolve in the electrolyte. The empty Mn site caused by the  $\text{Mn}^{2+}$  dissolution is then filled by a lithium ion. Therefore, new composite materials  $\text{Li}[\text{Li}_x\text{Mn}_{2-x}]\text{O}_4$  are produced. Due to the elemental change at Mn sites in the spinel structure, structural change happens during the dissolution. Moreover, the  $\text{LiPF}_6$ , which is dissolved in the electrolyte and acts as a conductive salt, turns to HF acid at times. HF acid can then react with the  $\text{Li}[\text{Li}_x\text{Mn}_{2-x}]\text{O}_4$  material and make it soluble in the electrolyte. After  $\text{Mn}^{2+}$  ions get into the electrolyte, many side reactions could be activated [59-61].  $\text{Mn}^{2+}$  dissolves from the surface in the 4-V domain to cause a capacity fade with cycling unless ionic substitutions are introduced that reduce the capacity even further (Figure 3.3) [12, 62]. The explosion of  $\text{LiCoO}_2$  cell could also be attributed to overcharging. When

overcharged (over 50% of Li ions escaped from the host structure),  $O_2$  will be generated inside the sealed cell and the inside pressure will increase, which raises safety concerns [63, 64].

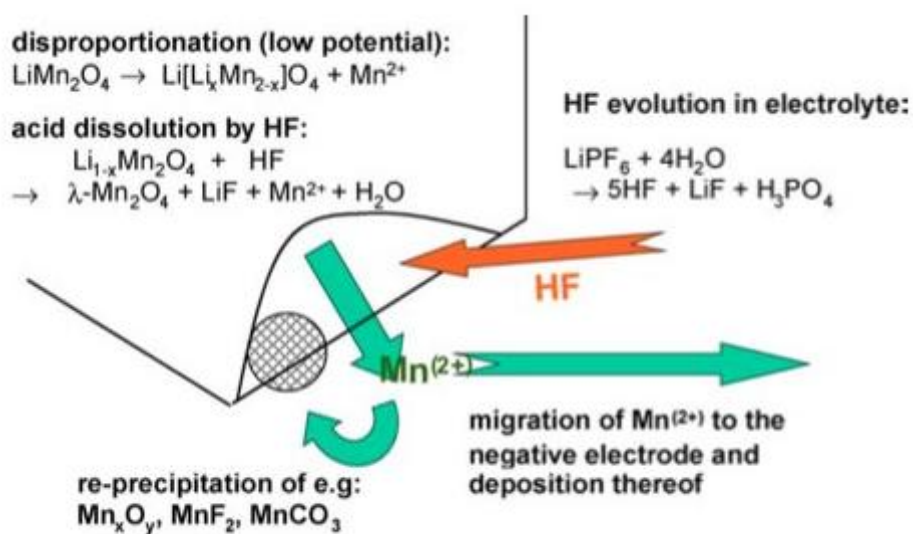


**Figure 3.3:** Reactions related to soluble Mn ions (Vetter, 2005) [58].

### 3.1.3 Structure and Jahn-Teller Effects

Structure failures in cathode materials caused by phase transformations during the insertion and desertion of lithium ions are primary factors that influence the aging/degradation mechanisms. A perfect eight-unit cell crystal  $\text{LiFePO}_4$  model without dislocations is shown in Figure 3.4(a) and lithium ions lay in the spaces along the b(y)-direction in the crystal. The crystal structure is made up by  $\text{FeO}_6$  octahedra,  $\text{PO}_4$  tetrahedra, and lithium ions (Fig. 4(b)). During discharging and charging, lithium ions shuttle in and out of the crystal through the spaces along the b(y)-axis and potentially lead to structural distortions or failures.

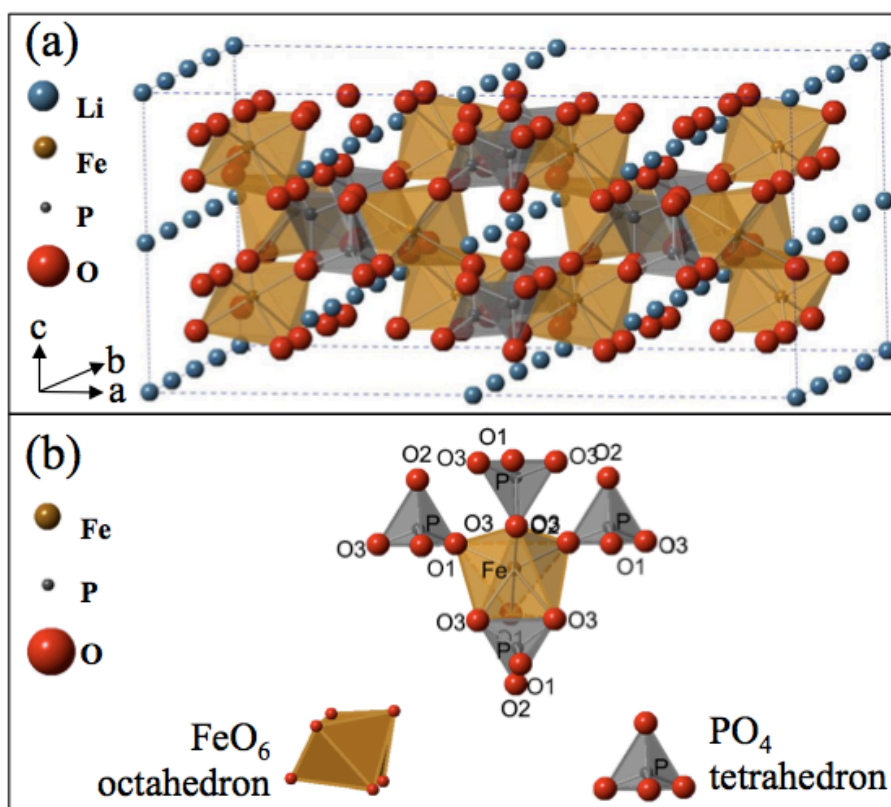


**Figure 3.4:** (a) Eight  $\text{LiFePO}_4$  unit cells without dislocations where lithium ions lay in the spaces along the b(y)-direction. (b) A  $\text{FeO}_6$  octahedron and five  $\text{PO}_4$  tetrahedra connect each other by sharing one edge and three corners.

The olivine-type crystal structure of  $\text{LiFePO}_4$  belongs to space group  $\text{Pnma}$ , in which Li, Fe, and P atoms occupy octahedral 4a (0, 0, 0), octahedral 4c ( $x$ ,  $\frac{1}{4}$ ,  $z$ ) and tetrahedral 4c ( $x,y,z$ ) sites, respectively (Figure 3.4(a)). A  $\text{FeO}_6$  octahedron lies in the middle and is surrounded by five  $\text{PO}_4$  tetrahedra (Figure 3.4(b)). One of the  $\text{PO}_4$  tetrahedra shares an edge (O-O bond) with the  $\text{FeO}_6$  octahedron, and the other four share four corners respectively. The crystal structures of  $\text{LiFePO}_4$  and  $\text{FePO}_4$  are similar except that the lattice parameter of  $\text{FePO}_4$  is smaller than that of  $\text{LiFePO}_4$ , due to differences in lattice parameters of  $\text{LiFePO}_4$  ( $a=10.334\text{\AA}$ ,  $b=6.002\text{\AA}$ ,  $c=4.695\text{\AA}$ ) and  $\text{FePO}_4$  ( $a=9.826\text{\AA}$ ,  $b=5.794\text{\AA}$ ,  $c=4.784\text{\AA}$ ); mismatch occurs during the phase transformation. With extraction of lithium from  $\text{LiFePO}_4$ , the volume decreases by 6.8% and the density increases by 2.6% [38]. The differences in lattice parameters could also be attributed to the different valences of Fe: the valence of Fe is +2 for  $\text{LiFePO}_4$ , and the valence of Fe is +3 for  $\text{FePO}_4$  [65, 66]. The difference in lattice parameter could be related to the Jahn-Teller effect. It states that the relationship between metal valences and lattice parameters can be used to justify lattice parameter changes in  $\text{LiFePO}_4$  and  $\text{FePO}_4$  [67]. In short, the outer shell electrons of an atom have a strong shielding effect caused by charge neutralization between outer shell electrons and atomic nucleus. The shielding effect would cancel out part of the electrostatic forces between the atomic nucleus and the atoms around it. Changing the valence of an atom will lead to a different electron configuration and the outer shell will have a different intensity of shielding effect in each direction (Figure 3.5). Therefore, when Li ions move out from  $\text{LiFePO}_4$ , the valence of the

Fe ions changes, and then the shielding effect in different directions around the Fe ions changes; this phenomenon may cause the structure of Fe octahedra to change.

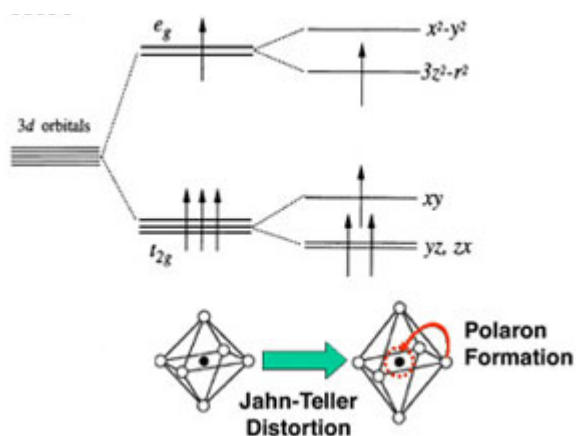


**Figure 3.5:** An schematic diagram for Jahn-Teller effect.

### 3.1.4 Lithium ions Diffusion and Particle Size

It is widely accepted that lithium ions diffuse along [010] 1D channels in LiFePO<sub>4</sub> cathode material [68, 69]. For LiFePO<sub>4</sub>, the charging/discharging process is a diffusion-controlled reaction. The process limitation is a combination of low lithium-ion phase-boundary diffusion and low electronic conduction in the two end phases. Since the low electronic conduction rate has been solved, people start focusing on investigating the relationship between LiFePO<sub>4</sub> capacity, rate capacity, and lithium diffusion. The [010] direction 1D channel could be easily blocked by impurities such as foreign phases with Fe<sup>3+</sup> ions, or defects such as Li/Fe ionic disorder or stacking faults. The blockage will lower the Li-ion diffusion coefficient and the availability of active material volume. The formation of

impurities and defects could attribute to inappropriate raw material ratio during synthesis or wrong state of charge during usage. It is found that larger  $\text{LiFePO}_4$  particles are more subject to stacking faults. The 1D channels are unlikely to be blocked by Li/Fe disorder or stacking faults if the particles are small. Besides less blocked channel, decrease of the particle size can also provide shorter diffusion lengths and a larger electrolyte/electrode contact area for the Li insertion and extraction reaction, which increases the diffusion rate. Many methods were tested to decrease the particle size. Doping carbon was found to be effective to decrease the particle size. Carbon acts as a nucleation agent to decrease the particle size. Moreover, the carbon acts as a reductant to avoid formation of undesirable ferric impurities [70, 71]. It is stated that the optimal carbon content is  $<5 \text{ wt}\%$  [38].

### **3.2 Aging of Anode Material**

For anode aging process, the main mechanism is the formation of solid electrolyte interface (SEI) layer. The SEI layer is formed at the interface between electrode material and electrolyte, where is one of the most important places in a Li-ion battery and the place that the side reactions most likely take place. In following, the SEI layer will be discussed in detail.

### 3.2.1 SEI layer formation

During the first several charging cycles of Li-ion battery, reductive electrolyte decomposition accompanied by irreversible consumption of lithium ions takes place at the electrode and electrolyte interface when the electrode is in the charged state. The decomposition will build up protective thin layers on the surface of anode. The protective layers could stop further reaction between anode material and electrolyte thus avoids further Li-ion consumption. Also, they protect the charged electrode from corrosion.

There are two types of protective layers. The ones covered on the pores and paths that Li-ions go through are called SEI. The SEI layers are permeable for Li-ions but rather impermeable for other electrolyte components and electrons. On the other hand, the layers which are on the non Li-ion transportation areas are called non-SEI. The non-SEI layers have different structure with SEI layers.[41]

Under some circumstances, such as high temperature or high end of charge voltages positive to 4.2V versus  $\text{Li/Li}^+$ , the protective layers could be dissolved or broken (Figure 3.6).

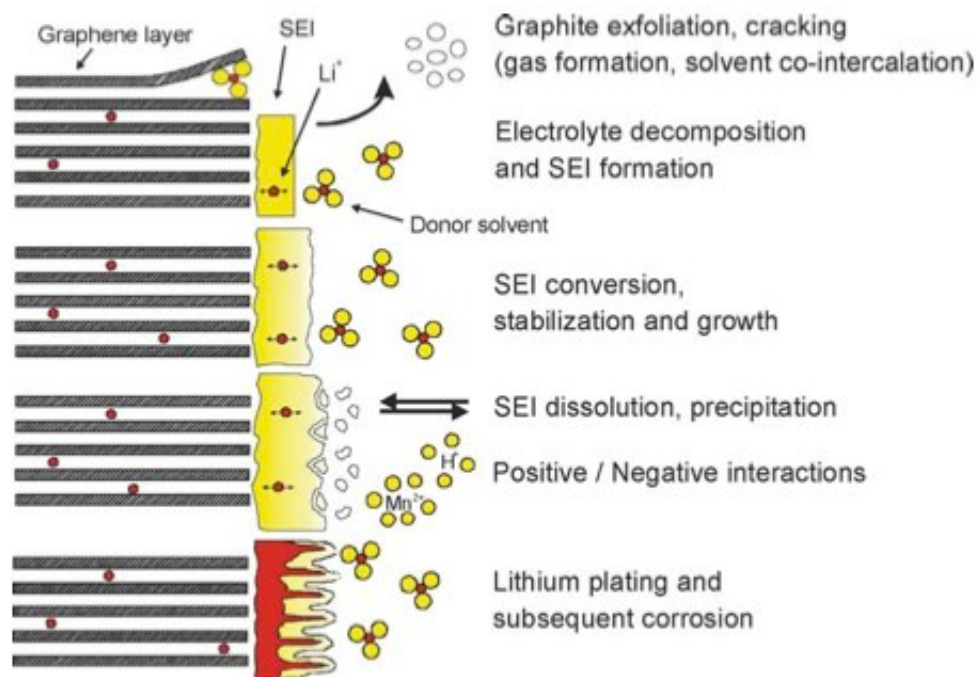
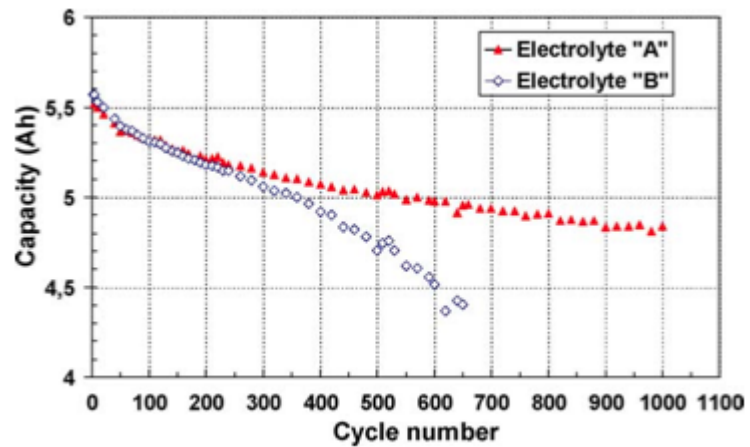
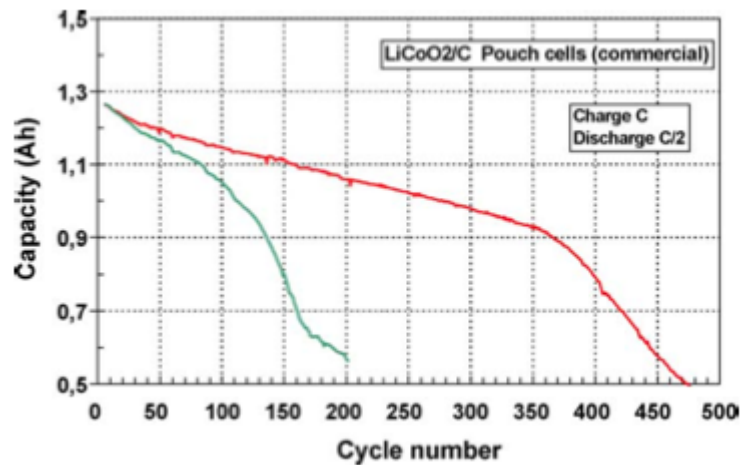


**Figure 3.6:** Formation, growth, and failure of SEI layers (Vetter, 2005) [58]

The SEI layer could protect the electrode material from corrosion. An experiment conducted by M. Broussely agreed the above statement: They cycle the battery for over 600 times and observe the capacity loss [43]. From the data, the capacity fade rate decreases with cycle time, resulting in stabilization with time of utilization (Figure 3.7). That is because with the passivation layer growth, the SEI produces a more and more stable interface, thus the corrosion rate is reduced.



(a)



(b)

**Figure 3.7:** Examples of capacity evolutions during 100% DOD cycling. (a) capacity loss rate decreases; (b) capacity loss rate increases. (Broussely, 2005) [43]

In some cases, the capacity loss rate increases with cycle number. However, in figure 3.6 (b), the capacity loss is due to the deposit of Li metal, which would also cause the increase of cell impedance. This phenomenon could be explained by the progressive clogging of the micro-pores of the negative electrode by the passivation layer growth (Figure 3.8).

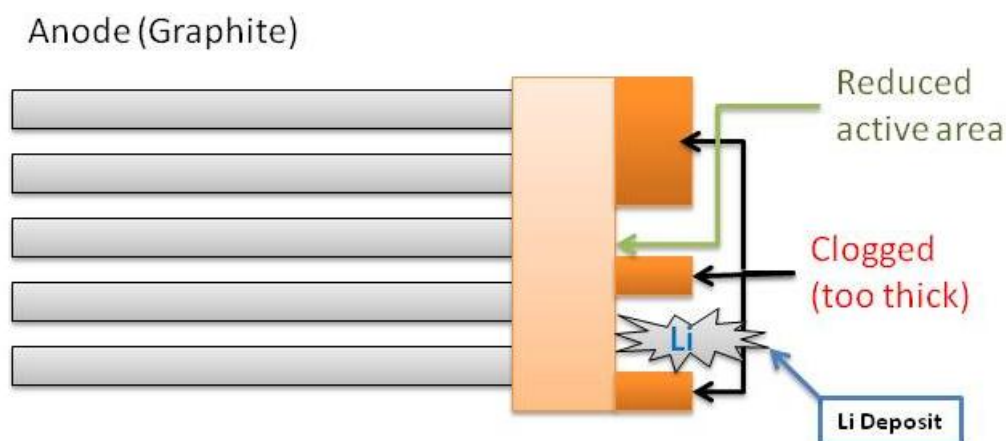


**Figure 3.8:** mechanism of Li deposit

If the SEI is broken, or the electrode material and electrolyte material were wrongly chose, and reaction of forming SEI is not stabilized enough even though the SEI layer is thick enough, the SEI layer would keep growing. The reaction products will depose in the microposity, thus significantly reducing the active surface area. Since the total current is a certain value, the current density will increase on the remaining available surface of the larger pores, up to the points where the reduction rate in these areas is larger than the maximum possible diffusion rate of Li in the graphite. Then, the exceed current will cause the Li deposit on the surface of SEI. When this process starts, lithium plating will produce more deposit itself and aggravates the phenmomenon, which explains the increasing of capacity fading rate (Figure 3.8).

At here, temperature decrease could accelerate the capacity fading rate by lowering the limit at which the Li plating will occur. Increasing temperature will reduce the Li plating limit, but it will accelerates the corrosion rate, which reduce the active area.[43]

### 3.2.2 Equation of Li Lost versus Time

When the battery is in storage, only the thermo stability of the components in battery affects the capacity fade. Among the four main components, the organic electrolyte and the Li-ion in anode material has the highest reactivity. Although the SEI layer has the ability to protect the anode from corrosion, the layer could not be perfectly hermetic, and low rate corrosion takes place at the surface of uncovered anode material. In 2001, M. Broussely et.al. developed a lithium corrosion kinetic model to account for the variation of capacity loss rate during accelerated aging on storage at high temperature. [43]

From that model, the corrosion rate is:  $\frac{dx}{dt} = k\chi s / e$ , where x is the number of moles of Li being reacting,  $\chi$  is the specific electronic semi-conductivity of the layer, s is the interface area and e is the SEI thickness. By integration, a parabolic equation of time versus lithium loss can be established:

$$t = \frac{A}{(2k\chi s)x^2} + \frac{e_0}{(k\chi s)x}$$

Where  $A$  is a proportionality coefficient between the layer thickness and the amount of lost lithium and  $e_0$  is the layer thickness at  $t_0$ , after battery formation. According to his article, a set of data obtained by an experiment after four years supported this equation very well.

## **CHAPTER 4 DISLOCATION BASED STRESS AND FORCE DEVELOPMENT IN $\text{LiFePO}_4$ MATERIAL**

Based on studies of the aging/degradation mechanisms of electrode materials, several methods to improve the stability of Li-ion battery have been developed. These include: (1) decreasing electrolyte decomposition by surface modification and reducing specific surface area [41, 51, 72-74], (2) neutralizing acid by adding proper additives into the electrolyte [41, 75], and (3) stabilizing the structure by doping anions and cations [76, 77]. However, among the aforementioned methods, almost no one could predict and prevent degradations caused by structural failures in cathodes due to lithium intercalation and extraction. Therefore, a better understanding of the mechanism and plausible models to depict cathode material structural failures due to lithium intercalation and extraction are required.

In some cases, such as charging/discharging too fast or unsteady charging voltage [41, 43], the moving rate of lithium ions is higher than the maximum allowed diffusion rate of  $\text{LiFePO}_4$  cathode material. Under that circumstance, lithium ion diffusion would not be well organized and might create incomplete or extra lithium ion planes in  $\text{FePO}_4$  structure. Thus dislocations will be generated due to the half atom planes.

In this chapter, previous works on dislocation-based stress fields are discussed and stress distributions in  $\text{LiFePO}_4$  cathode materials are provided. I chose  $\text{LiFePO}_4$  as our model system due to: (1) It is recognized that  $\text{LiFePO}_4$  is a promising cathode material for Li-ion batteries, thus understanding stress accumulations inside the material is important for developing longer-lasting Li-ion battery materials, and (2)  $\text{LiFePO}_4$  has a 3D matrix structure

with anisotropic elastic material properties. Once I successfully build up a model system for this sophisticated material, I will then be able to provide a general mathematical framework for other Li-battery cathode materials, such as  $\text{LiCoO}_2$ ,  $\text{LiMnO}_2$ , and  $\text{LiNiO}_2$ .

#### 4.1 Dislocation and Burgers Vector

As Li ions leave the parent phosphate, the formation of  $\text{FePO}_4$  generates strong dislocation stress fields in the lattice which could lead to the generalization of dislocation. A dislocation is a crystallographic defect or irregularity, within a crystal structure. Two main types of dislocation exist: edge dislocation (Figure 4.1(a)) and screw dislocation (Figure 4.1(b)). Dislocations found in real materials typically are mixed, meaning that they have characteristics of both.

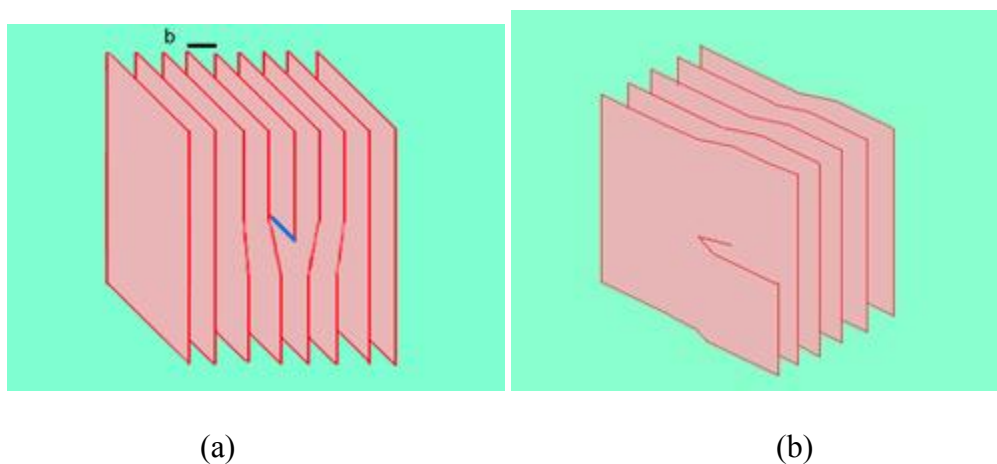


**Figure 4.1:** edge dislocation (a) and screw dislocation (b)

The Burgers vector is a vector that denotes the magnitude and direction of lattice distortion associated with a dislocation. To obtain the vector's magnitude and direction, I should start with a perfect crystal structure, which has no dislocation or other defects. In the perfect crystal structure, a rectangle whose lengths and widths are integer multiples of "L" (the unit cell length) is drawn encompassing the site of the original dislocation's origin. Once this rectangle is drawn, the dislocation can be introduced. Since the dislocation will deform the perfect crystal structures near it, the rectangle around it will be affected as well. What was once a rectangle before the dislocation was introduced is now an open geometric circle, whose opening defines the direction and magnitude of the Burgers vector (Figure 4.2). The Burgers vector can be used to identify both magnitude and the nature of a dislocation. If the Burgers vector is parallel to the dislocation line, this indicates a screw dislocation (Figure 4.2(a)). If, however, it is perpendicular, this indicates an edge dislocation (Figure 4.2(b)). An angle other than these is indicative of a mixed dislocation. Numerically, Burgers vector usually represents by a three elements vector. For example, the vector (020) stands for the Burgers vector is along the y axis and has no components in x and z direction; the length of Burgers vector is twice as the unit cell length.

In face centered cubic and base centered cubic structures, the Burgers vector may be expressed as:  $\mathbf{b}=(L/2)[hkl]$ , where L is the unit cell edge length and [h k l] is the crystallographic direction having the greatest linear atomic density. According to vector calculation, the magnitude of the vector is:  $|\mathbf{b}|=(L/2)(h^2+k^2+l^2)^{1/2}$

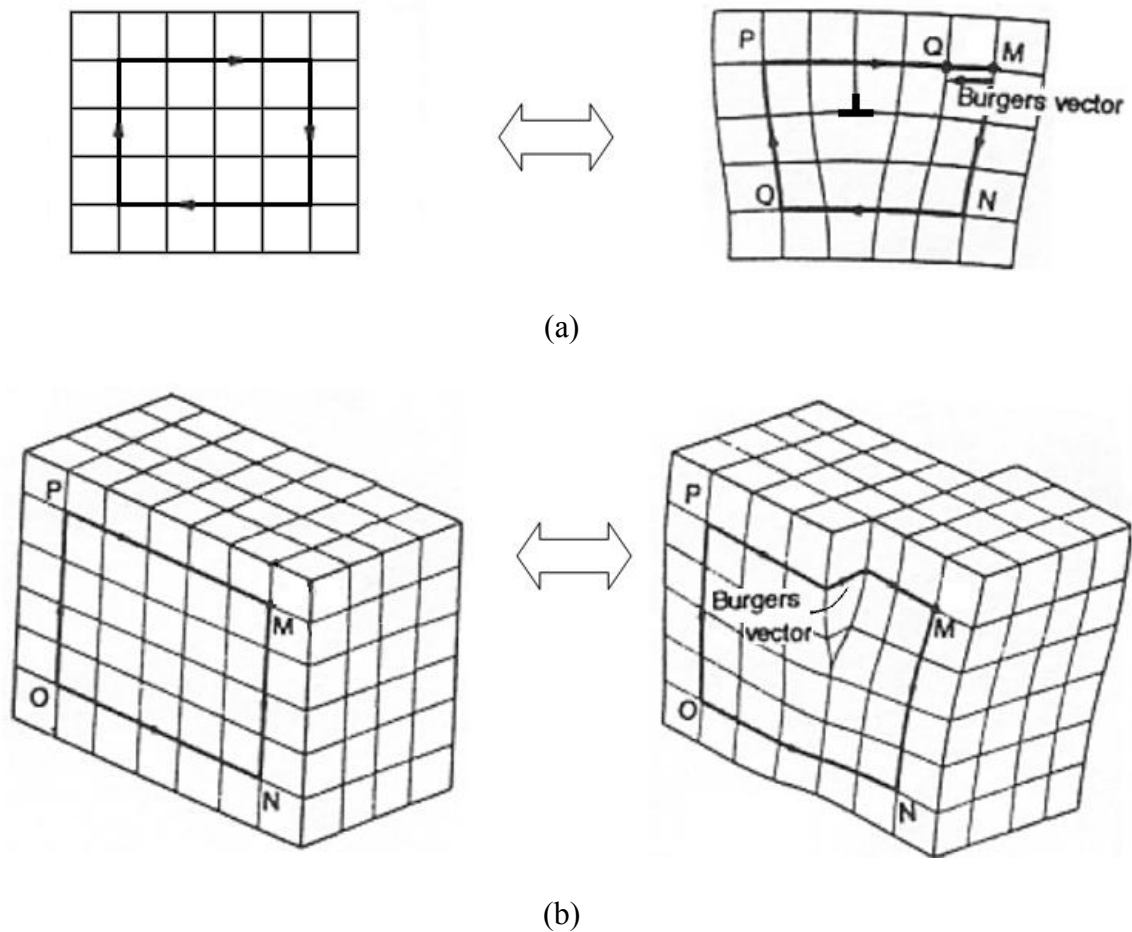
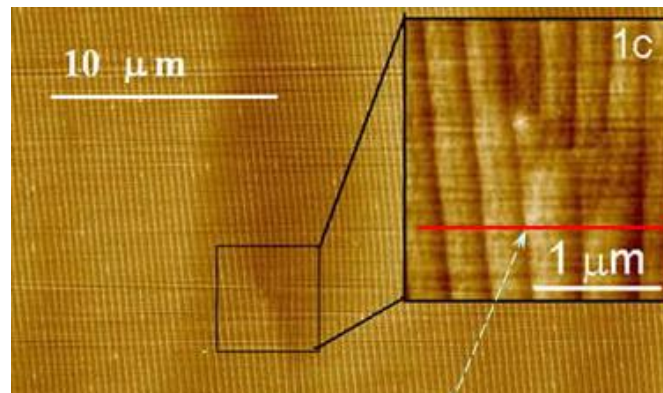
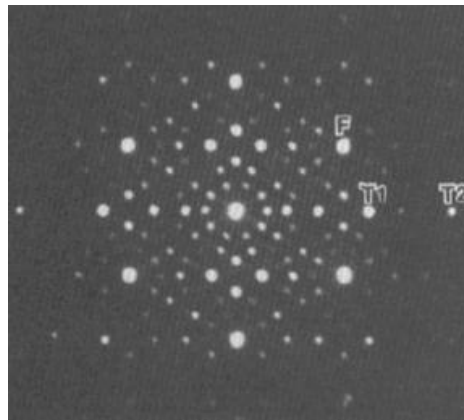


**Figure 4.2:** Determine the Burgers vector by drawing rectangular. (a) edge dislocation; (b) screw dislocation

In reality, it is hard to determine the Burgers vector just by drawing circles on a photo of dislocation (Figure 4.3(a)). Sometimes the dislocation is inside the sample, sometimes the dislocations is complicated to recognize by eyes. Thus, besides observing the dislocation by SEM or AFM, researchers may also do some vector calculation by using electron diffraction pattern got from TEM or XRD methods (Figure 4.3(b)). With the magnitude of Burgers vector determined, the accommodated stress field could then be calculated.



(a)



(b)

**Figure 4.3:** (a) Determine Burgers vector by PLM/AFM photo. (b) determine Burgers vector by XRD picture

## 4.2 Development of Stress Field Calculation

Chen et. al observed cracks in  $\text{LiFePO}_4$  particles from SEM images, which provide evidences of accumulation of dislocations (Figure 4.4) [69][78]. In the study, they also concluded that cracks along  $c$ -direction (the long axis of crystal parallel to  $c$ ) appear to get larger during the process of delithiation. With  $\text{Li}_{0.5}\text{FePO}_4$  samples, slight rotation around  $b$ -

direction of the two phases was observed, indicating the deformation and dislocation associated with delithiation. The same group also reported a TEM image of  $\text{Li}_{0.5}\text{FePO}_4$  sample where a clear disorder region was observed along c-direction (Figure 4.5) [69]. Therefore, it is suggested that the dislocation and distortion zones would be formed by phase transformation during the insertion and desorption of lithium ions and potentially leads to structural failures [79, 80]. Since  $\text{FePO}_4$  and  $\text{LiFePO}_4$  are connected with a coherent interface due to similar crystal structures, internal stresses would form during the phase transformation; the resultant atomic-level displacements lead to dislocations inside crystals (Figure 4.6). Moreover, it is observed that the lithium ion insertion and extraction process leads to  $\sim 7\%$  volume change between  $\text{LiFePO}_4$  and  $\text{FePO}_4$  phase crystals. This is due to internal stress and strain accommodations that occur in  $\text{LiFePO}_4$  crystals because of the coherent interface between phase boundaries (Figure 4.7) [81]. The internal strains initiate dislocations that form after several intercalation-extraction cycles inside cathode materials, and these dislocations potentially lead to the growth of minor cracks.

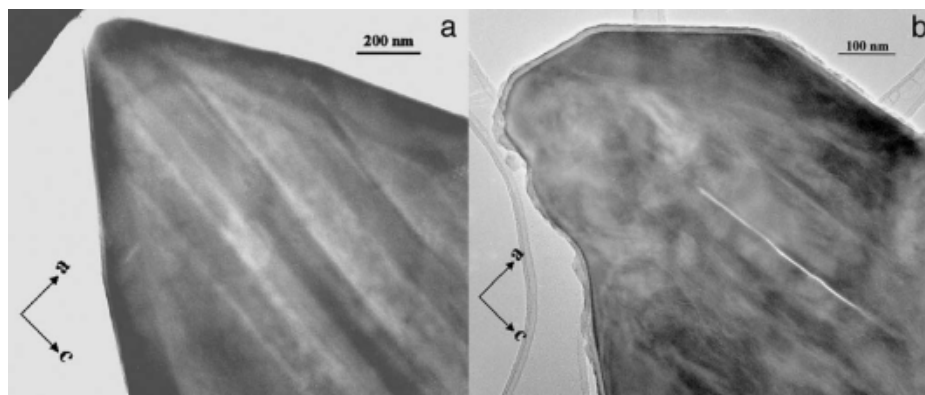


**Figure 4.4:** Observed cracks in  $\text{LiFePO}_4$  particles from SEM images (Chen, 2006) [78]

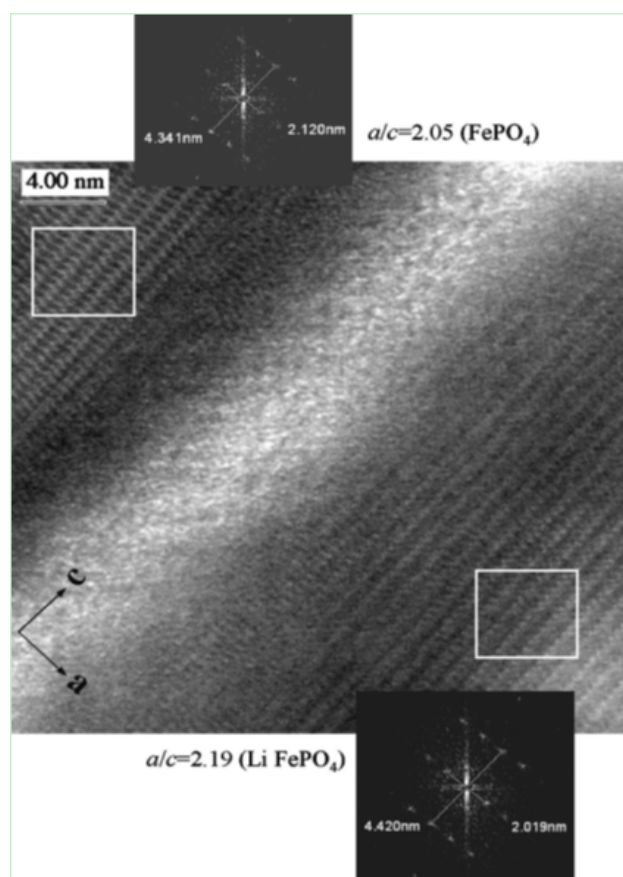


**Figure 4.5:** HRTEM image of the disordered region at the end of the crack in Fig.4, with Fourier transforms of the indicated areas. (Chen, 2006) [69]

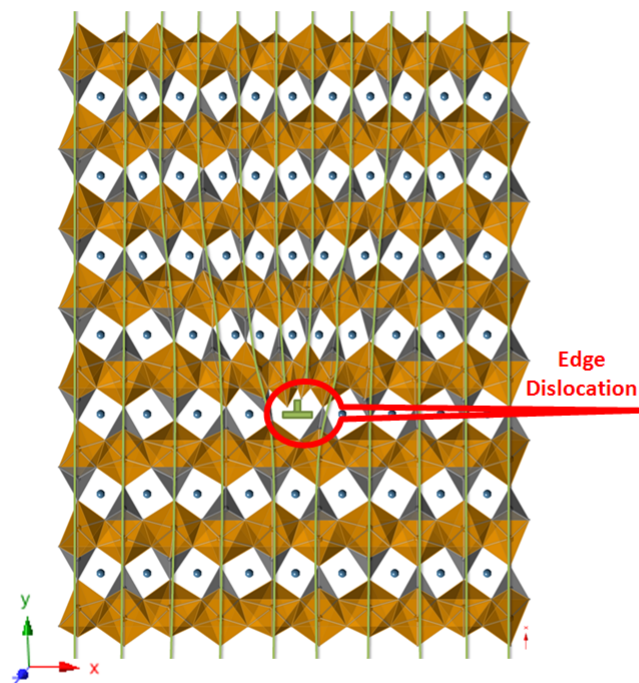


**Figure 4.6:** A  $\text{LiFePO}_4$  crystal model with an infinite length edge dislocation. Edge dislocation is along  $z$ -direction ( $c$ -direction).

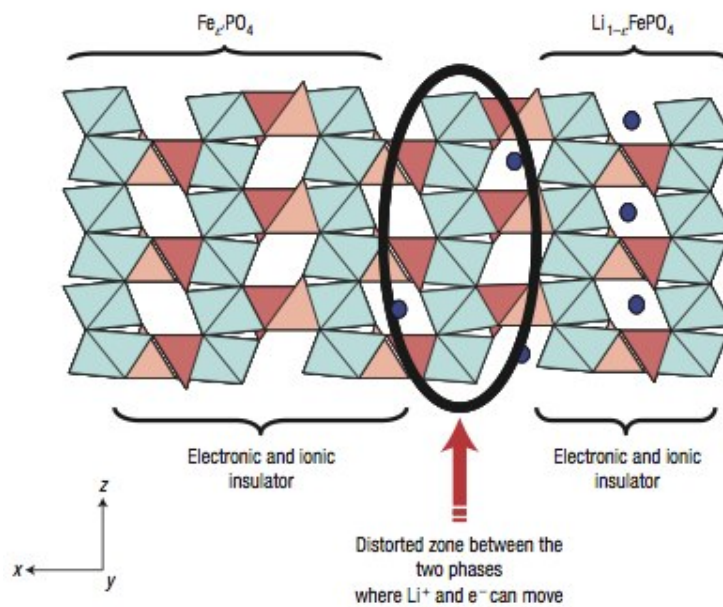


**Figure 4.7:** Distortion zone between LFP phase and FP phase (Delmas, 2008) [68]

To quantify the stress-fields of dislocation of LiFePO<sub>4</sub>, numerical models are developed. Calculations for stress fields of dislocations in crystals are usually approximated as isotropic materials with the classical analytical solution for convenience (I will use it as model A in following parts) [82]:

$$\sigma_{xx} = \frac{-\mu b}{2\pi(1-\nu)} \frac{y(3x^2 + y^2)}{(x^2 + y^2)^2}$$

$$\sigma_{yy} = \frac{\mu b}{2\pi(1-\nu)} \frac{y(x^2 - y^2)}{(x^2 + y^2)^2}$$

$$\tau_{xy} = \frac{\mu b}{2\pi(1-\nu)} \frac{x(x^2 - y^2)}{(x^2 + y^2)^2}$$

**Equation (1)**

However, most cathode materials have anisotropic materials properties. For instance, LiFePO<sub>4</sub> cathode materials for Li-ion battery exhibit orthorhombic crystal structures and have different elastic constants in different directions (Figure 3.4(a)) [83]. Noticing the importance of elastic property of anisotropic materials, studies have focused on developing analytical solutions of stress fields causing by dislocations. In 1953, J. D. Eshelby et al. developed general solutions for evaluating dislocation stresses for an arbitrary homogeneous anisotropic solid material [84]. Numerical solutions were then developed, such as elastic

equations for pure screw dislocation lines with infinite length in monoclinic crystal system materials, and for pure edge dislocation lines with infinite length in orthorhombic crystals. However, limited by computational methods at that time, only few equations for simple cases were fully solved. Later on, with the developments of computers, graphs for the distributions of stress fields around dislocations with anisotropic materials properties were developed [85]. Recently, solutions for stress fields of dislocation loops have been developed [86].

In 1975, H. L. Heinisch et al. numerically calculated the elastic stress fields, self-energies, and energy factors of straight edge and screw dislocations in olivine materials [85]. With the help of computers, stress distributions were provided for different directions of dislocations. From the figures, Heinisch et al. concluded that the orthorhombic olivine materials have moderate elastic anisotropy, though the effects of anisotropy seem to be relatively small. Moreover, the stress distributions of edge dislocations in olivine anisotropic materials properties are similar to those with the isotropic materials properties, with minor differences in the values. They have compared the numerical results with experimental observations. However, they did not successfully predict the slip direction and glide plane preference of dislocations for orthorhombic anisotropic materials based on elasticity theory.

Later in 1992, V.L. Indenbom and J. Lothe introduced an general analytical solution of dislocations for orthorhombic material [87] (I will use it as model **B** in following parts):

$$\sigma_{\bar{y}} = \frac{b_x \lambda (C_{12} - \bar{C}_{11})}{4\pi q^2 t^2 \bar{C}_{11} C_{66} \sin \phi} \left\{ \begin{aligned} & C_{\bar{y}11} \left[ (\bar{C}_{11} + C_{12} + C_{66}) x^2 y + \lambda^2 C_{66} y^3 \right] - C_{\bar{y}12} (\bar{C}_{11} + C_{12}) (x^3 - \lambda^2 x y^2) \\ & - \frac{C_{\bar{y}22}}{C_{22}} \left[ (\bar{C}_{11} C_{12} + C_{12}^2 + 2C_{12} C_{66} + \bar{C}_{11} C_{66}) x^2 y - \bar{C}_{11} C_{66} \lambda^2 y^3 \right] \end{aligned} \right\}$$

$$- \frac{b_y \lambda (C_{12} - \bar{C}_{11})}{4\pi q^2 t^2 \bar{C}_{11} C_{66} \sin \phi} \left\{ \begin{aligned} & C_{\bar{y}22} \left[ (\bar{C}_{11} + C_{12} + C_{66}) \lambda^2 x y^2 + C_{66} x^3 \right] - C_{\bar{y}12} (\bar{C}_{11} + C_{12}) (\lambda^2 y^3 - x^2 y) \\ & - \frac{C_{\bar{y}11}}{C_{11}} \left[ (\bar{C}_{11} C_{12} + C_{12}^2 + 2C_{12} C_{66} + \bar{C}_{11} C_{66}) \lambda^2 x y^2 - \bar{C}_{11} C_{66} x^3 \right] \end{aligned} \right\}$$

$$\sigma_{\bar{z}} = \frac{b_z}{2\pi} (C_{44} C_{55} - C_{45}^2)^{1/2} \left( \frac{C_{45} x - C_{55} y}{C_{44} x^2 - 2C_{45} x y + C_{55} y^2} \right),$$

$$\sigma_{y\bar{z}} = -\frac{b_z}{2\pi} (C_{44} C_{55} - C_{45}^2)^{1/2} \left( \frac{C_{44} x - C_{45} y}{C_{44} x^2 - 2C_{45} x y + C_{55} y^2} \right)$$

where:  $\bar{C}_{11} = (C_{11} C_{22})^{1/2}$ ,  $\lambda = (C_{11} / C_{22})^{1/4}$ ,  $\phi = \frac{1}{2} \cos^{-1} \left( \frac{C_{12}^2 + 2C_{12} C_{66} - \bar{C}_{11}^2}{2C_{11} C_{66}} \right)$ ,

$$q^2 = x^2 + 2xy\lambda \cos \phi + y^2 \lambda^2, \quad t^2 = x^2 - 2xy\lambda \cos \phi + y^2 \lambda^2$$

### Equation (2)

The equation fits well for anisotropic materials, suggesting that it could be used to predict dislocations of LiFePO<sub>4</sub>. Based on their model, a coordinate system with the z-axis along the dislocation was chosen and the sense vector of the dislocation was to point to the negative z-direction. This coordinate system is aligned with the dislocations lines observed in LiFePO<sub>4</sub> cathode materials; the dislocation sense vector in LiFePO<sub>4</sub> materials is along z-direction.

Once the elastic coefficients are available [83], the magnitudes and distributions of internal stress and strain fields that caused by dislocations in  $\text{LiFePO}_4$  could be obtained.

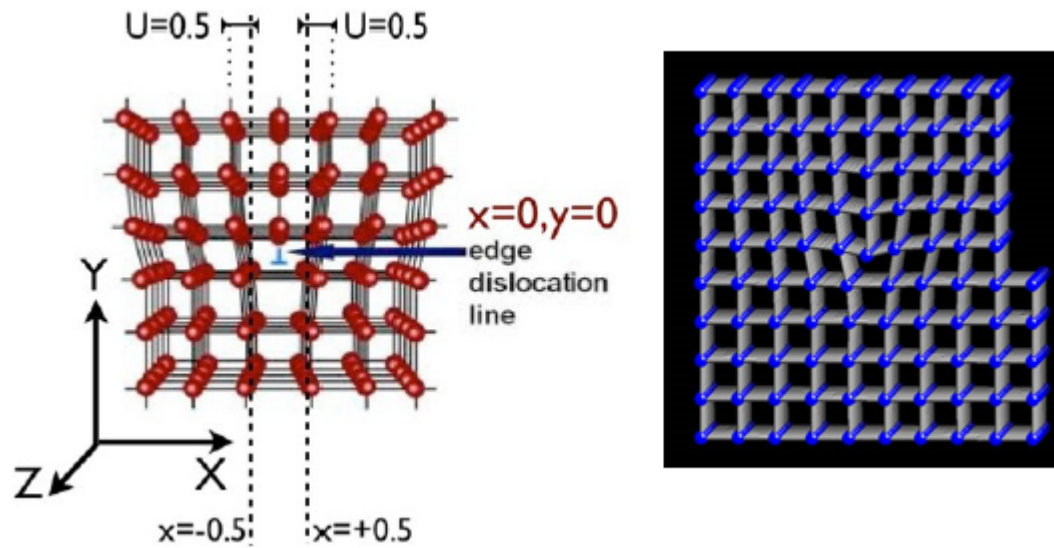
### **4.3 Verifying Analytical Solution by Finite Element Modeling Method**

Before starting the modeling and calculation process for the dislocation stress field in  $\text{LiFePO}_4$  material with its isotropic/anisotropic property, I firstly tested the feasibility of classical analytical solution (model A) with finite element analysis (FEA) modeling method by comparing the stress results from FEA method and classical analysis equation. The classical analytical stress-dislocation equation for isotropic material (model A) has been developed and widely used for over 50 years. However, the classical equations only fit for the simplified case: a single infinite length edge dislocation that parallels to z-axis in an isotropic material, which does not fit our anisotropic  $\text{LiFePO}_4$  material. So for this comparison and justification, I only consider this  $\text{LiFePO}_4$  dislocation system as the simplest case: (1)  $\text{LiFePO}_4$  material as polycrystalline material that has isotropic property during the test; (2)  $\text{LiFePO}_4$  particle has a square shape and the length of each side is equivalent; (3) only one dislocation line lays in the particle, and it parallels to z-axis. More complicated and realistic model will be considered during further modeling in next chapters.

In the modeling and testing process, crystal with an edge dislocation was modeled as a bulk with an extra half plane lays in y-z plane. Considering the real dimension of crystals, I set crystal lattice constant (the length between two nearest atoms) as  $L=10\text{\AA}=10\times 10^{-10}\text{m}$ . And the area of x-y plain is set as  $100L\times 100L$  because this area is big enough to provide

accurate results but not too big for meshing and computation. The deformation load brought by the edge dislocation could be modeled in this way: The extra half atom plane lays in the upper part of the bulk (plane coordinates:  $x=0, y>0$ ). That extra plane will take extra space of  $1L$  width, which is one unit of crystal lattice. To make the  $1L$  width room for that extra plane, two neighboring planes will move to left/right accordingly. The left half plane moves  $0.5L$  to the left and the right half plane moves  $0.5L$  to the right (Figure 4.8a). For boundary condition, since the atoms in far away area are still in a good order (Figure 4.8b), the displacements on surfaces of the bulk are 0. At last, since the edge dislocation appears in the middle of the symmetric shaped bulk on x-y plain, I just need to analyze the left/right half of the model. In other words, our FEA assumption is that the bulk would not have any displacement on its surface but only have displacements of crystal lattice inside. According to the references, Young's modulus is 88.83 GPa, and Poisson ratio is 0.34 [89].

With the above simplifications and assumptions, I provide dislocation stress distributions for  $\text{LiFePO}_4$  crystals calculated by classical equation (model A) with mathematical software Mathematica. The stress distribution plot is showed in Figure 4.9, and the stress values at each node are listed in Appendix A.



(b)  
**Figure 4.8:** (a) FEA Model for our dislocation problem. (b) dislocation problem in larger scale

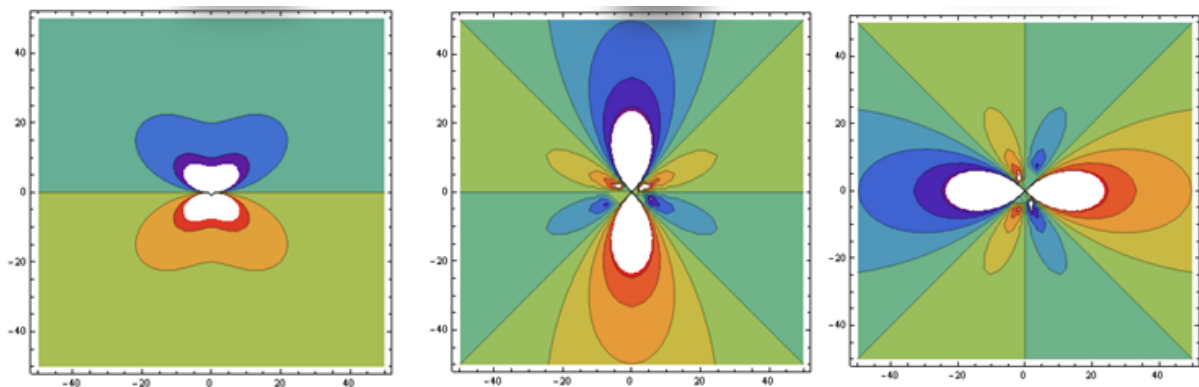


**Figure 4.9:** Dislocation stress distribution plot in  $\text{LiFePO}_4$  material with isotropic property and classical equations (model A).

After the modeling, I could obtain the computed stress values data by running a static analysis with ANSYS FEA software. Stress data at each node and the stress distribution plot could then be obtained. The stress values at each node calculated from ANSYS and from classic elasticity equations are compared. The data comparison graphs (figure 4.10, 4.11,

4.12) were plotted to cross verify the feasibility of classical analytical solutions (model A) and ANSYS model in function of predicting the stress field from dislocation.

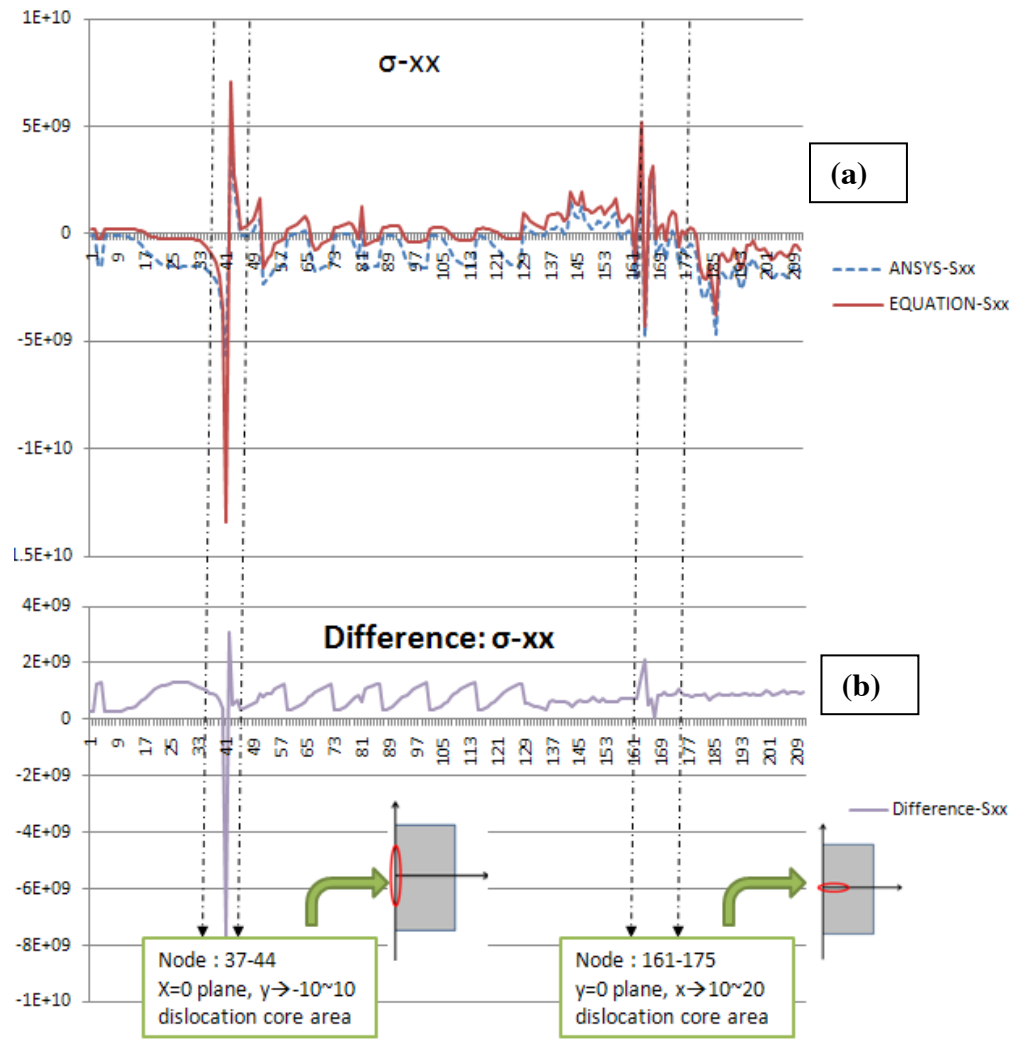


**Figure 4.10:** (a) Plot of stresses  $\sigma-xx$  calculated by classical equation and ANSYS model. (b) Numerical difference between two sets of stress data (Equation - ANSYS)

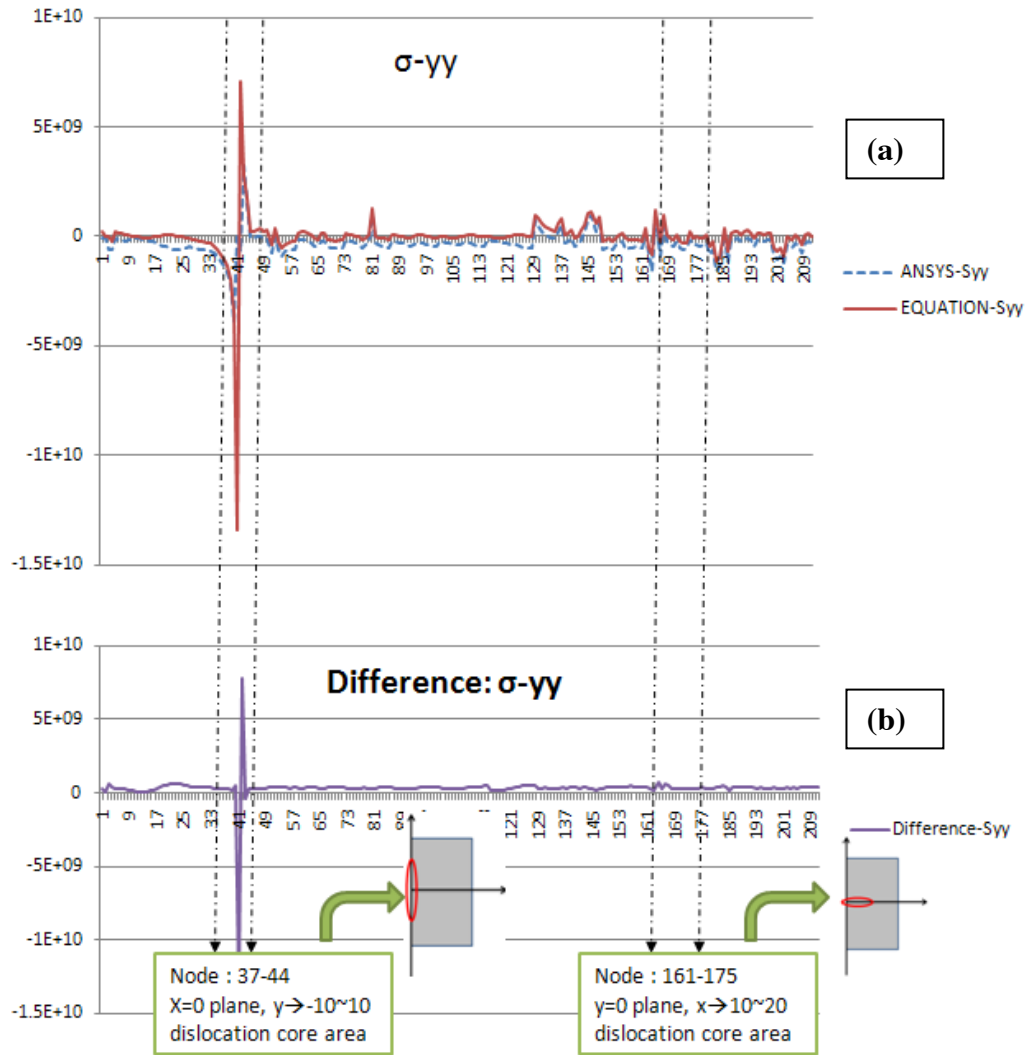


**Figure 4.11:** (a) Plot of stresses  $\sigma_{yy}$  calculated by classical equation and ANSYS model. (b) Numerical difference between two sets of stress data (Equation - ANSYS)

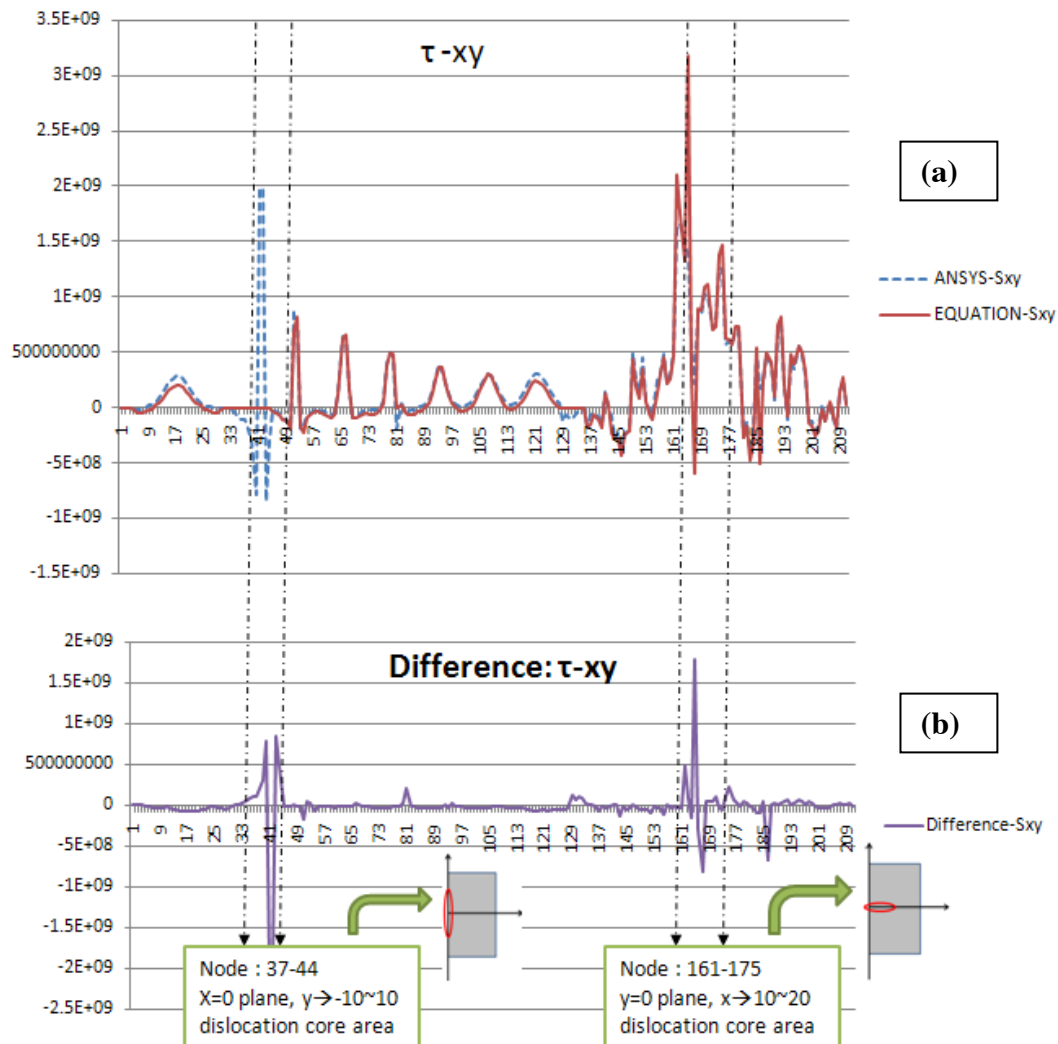


**Figure 4.12:** (a) Plot of stresses  $\tau-xy$  calculated by classical equation and ANSYS model. (b) Numerical difference between two sets of stress data (Equation - ANSYS)

Several characteristics of the data plots could be observed from figure 4.10, 4.11 and 4.12:

(1). As shown in figure 4.10, 4.11 and 4.12, the plot of stress values from ANSYS model are having the same shape as the plot of analytical results from classical equation. In addition, the differences between two sets of results are relatively small. Therefore, I could safely state that the ANSYS method for analyzing the stress field works very well for this

model. In other words, the FEA analyzing method could provide nearly the same results as classical elastic mechanical theory does.

(2). The stress values from classical analytical equation are slightly higher than values from ANSYS method. This is because that the stress value generated by FEA method is lower than the real value due to the stiffness matrix  $[K]$  is approximated to be lower than the actual physical case.

(3). Stresses near the dislocation field are much larger than those in outer part. In those areas, the differences of stress values between ANSYS model and theoretical equation are much larger as well. That is due to the stress concentration led by big geometry changes.

(4). The stress value differences are larger in  $\sigma$ -yy and  $\tau$ -xy calculating than them in  $\sigma$ -xx calculating, which is the same direction displacement load applies. So I may assume that the ANSYS model works better in predicting stresses in directions that do not have shape deformation.

In addition, I use Mathematica 7.0 to plot the stress distribution graphs (Figure. 4.13) according to classical equation. The graphs shows that the stress distribution generated by ANSYS and by classical theory are sharing the same shape, which support our statement that the ANSYS works well in this case.

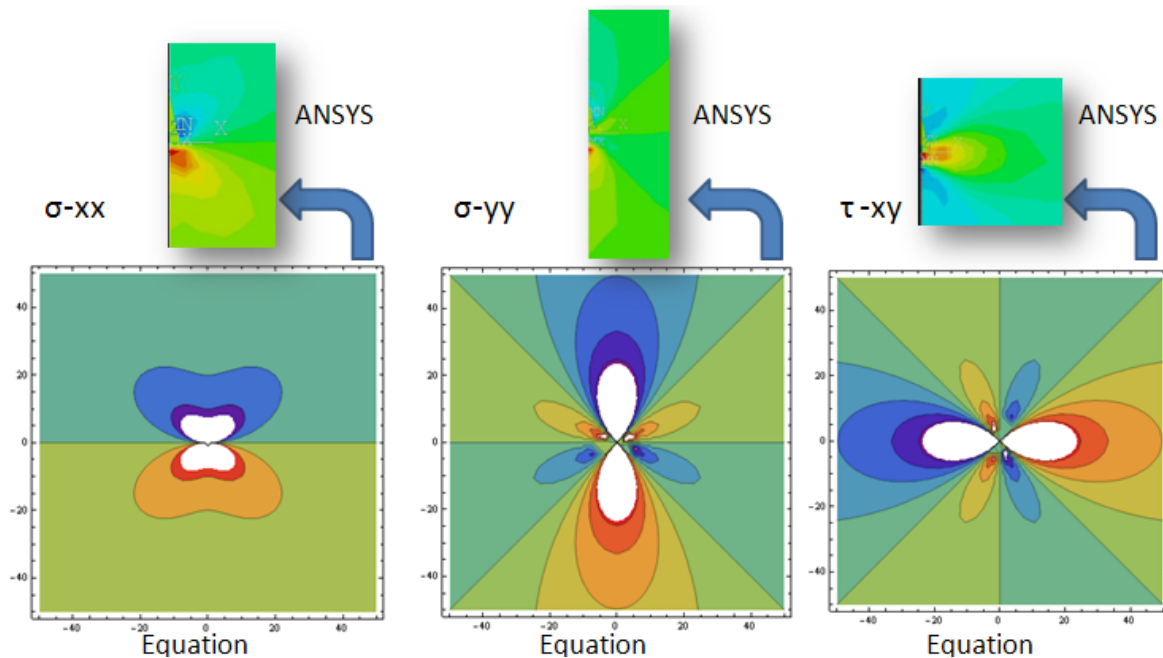


**Figure 4.13:** Comparison of stress distribution graphs from ANSYS and analytical equation

With the ANSYS analyzing, the origin problem and its solution now could be described: Due to the appearance of an extra half atom plane in the middle of upper part of a crystal, atom planes next to the extra plane are forced to move aside to make the room for extra plane (plane on the left side of extra atom plane moves to left, plane on the right side of extra atom plane moves to right). When the two atom planes move to left and right accordingly, internal stress will be generated around the displacement zone. So far, I could say the classical analytical solution works well on predicting dislocation stress distribution in  $\text{LiFePO}_4$  material with isotropic property. It generates almost the same result as the result from FEA method which based on elasticity theory.

#### 4.4 Generalized Solution for Stress Field with Isotropic and Anisotropic material

##### Property

The FEA aided feasibility testing of analytical stress field solution shows that it is safe to use the analytical equations to calculate the stress field in LiFePO<sub>4</sub> material. Thus a further detailed stress field modeling was conducted: To ensure the dislocation stress value for LiFePO<sub>4</sub> material obtained from our numerical modeling is precise, the stress model should be similar to the real cases, and the elastic constant data and geometric data should be close to the real value. Thus, I used the isotropic and anisotropic materials constants that were obtained from the first principal calculations by the Ceder's group at MIT (Table 4.1) [89].

**Table 4.1:** Anisotropic elastic constants for olivine structure LiFePO<sub>4</sub> material

V	299.54Å <sup>3</sup>	c11	138.9 GPa
a	10.45Å	c12	198.0 GPa
b	6.05Å	c33	173.0 GPa
c	4.74Å	c44	36.8 GPa
		c55	50.6 GPa
		c66	47.6 GPa
		c12	72.8 GPa
		c13	52.5 GPa
		c23	45.8 GPa

With the above data and analytical equations provided in previous part, stress value at any position around the dislocation could be calculated. A stress distribution plot could be

further plotted with the calculated stress data. Now review the equation (1): classical analytical solution (model A), and equation (2): generalized analytical solution (model B):

Based on the lattice parameters of  $\text{LiFePO}_4$  ( $a=10.334\text{\AA}$ ,  $b=6.002\text{\AA}$ ,  $c=4.695\text{\AA}$ ) [26], the model dimensions is set as  $100L \times 60L$  on the a-b plane with 60 unit cells, where  $L=10\text{\AA}$ . This is a plausible representative model size due to: (1) the reported  $\text{LiFePO}_4$  particle size is approximately several hundred nanometers [48], which could be correctly represented by  $100L \times 60L = 100\text{nm} \times 60\text{nm}$  in the proposed model system, (2) the model size is sufficient to avoid  $4L \times 4L$  dislocation core regions, the regions within which the elastic solutions would not be valid [90], and (3) the model size of  $100L \times 60L$  is sufficient to depict overall stress distributions without any boundary effects. It can be seen from the equations (1) and (2) that the classical equation which is for isotropic material only needs two elastic constants ( $\mu$  and  $\nu$ ) and one Burgers vector variable. While the generalized equation that is for anisotropic material could allow the utilization of all the 9 elastic constants for  $\text{LiFePO}_4$  material and has two Burgers vector components, which allows the dislocation rotates in x-y plane. In order to plot the stress distribution graph with both models A and B then make a comparison, the original 9 elastic constants for  $\text{LiFePO}_4$  need to be converted to two elastic constants to fit in the classical isotropic equation. The converted isotropic constants are:  $\mu=G=33.05\text{GPa}$  and  $\nu=0.34$ :

$$E = \frac{(c_{11} - c_{12})(c_{11} + 2c_{12})}{(c_{11} + c_{12})} = 88.83\text{GPa}, \nu = \frac{c_{12}}{c_{11} + c_{12}} = 0.34, \mu = G = \frac{E}{2(1 + \nu)} = 33.05\text{GPa}$$

The stress solution obtained from classical equation (model A) with isotropic property and generalized equation (model B) with isotropic property were both plotted and compared with each other to determine if the generalize equation produces the same stress field when using the same isotropic constants. And the stress solution obtained from generalized equation (model B) with isotropic property and generalized equation (model B) with anisotropic property were both plotted and compared with each other to determine the how much the anisotropy property will affect the stress field distribution in LiFePO<sub>4</sub> material when using the same solution equation (Figure 4.14).

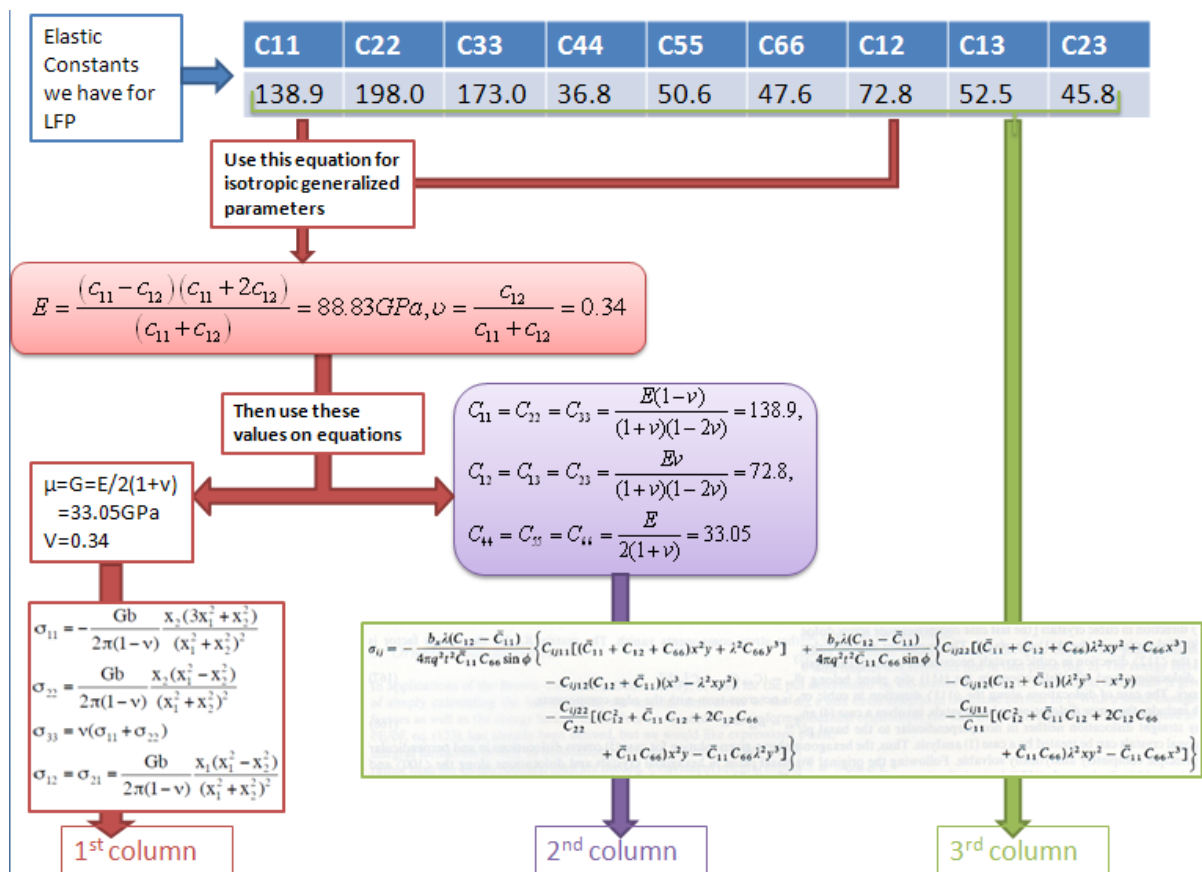


**Figure 4.14:** Flow chart of stress distribution plotting: from converting elastic constants to choosing modeling equations. Red: classical equation with isotropic property; purple: generalized equation with isotropic property; green: generalized equation with anisotropic property.

Classical (model A) [82] and generalized (model B) [87] stress fields for a single edge dislocation (with Burger's vector,  $b_x=1$ ) with isotropic material properties [83] were compared in Figure 4.15(a) and (b). Similarly, classical and generalized stress fields for a screw dislocation (with Burger's vector,  $b_z=1$ ) with isotropic material properties [83] were compared in Figure 4.15(f) and (g) (Appendix B). The results suggest that generalized stress fields are equivalent to classical ones, which provide a solid basis for varying material properties on the said generalized solutions. By incorporating anisotropic material properties of  $\text{LiFePO}_4$  [83] into our model systems, the results reveal that the stress fields are comparable to ones with isotropic material properties (Figure 4.15(c) and (h)), which is in agreement with Heinisch et al.: the effects of anisotropy for orthorhombic olivine materials is insignificant [85].

In most cases, Burger's vectors are not perfectly parallel to one specific axis. Therefore, I expanded our model system to examine stress variations for arbitrary Burger's vector directions. Interesting stress fields are observed for  $b_x=1, b_y=0.6$  in Figure 4.15(d) (for Burger's vectors aligned with  $45^\circ$  from the  $+a(x)$  direction) and  $b_x=0, b_y=0.6$  in Fig. 4.15(e) (for Burger's vectors aligned with  $90^\circ$  from the  $+a(x)$  direction). Comparing with stress fields in Figure 4.15(a) and the one in Figure 4.15(e), it is suggested that stress values for arbitrary Burger's vector directions could be simply calculated by utilizing linear transformations. Moreover, the stress field for the screw dislocation is derived via the displacement in the  $c(z)$ -direction, therefore Burger's vectors in the  $x$  and  $y$  directions are unavailable.

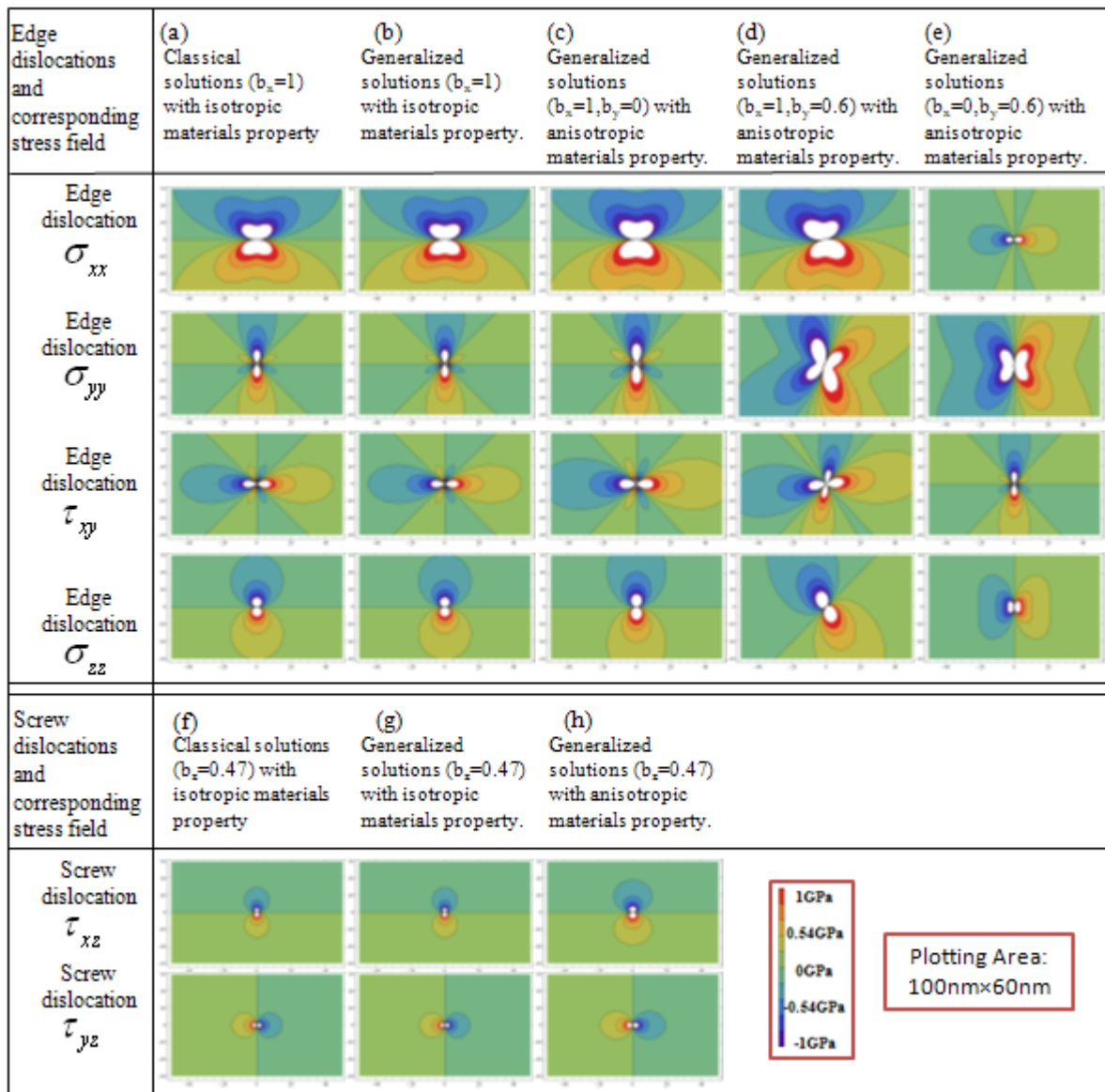


**Figure 4.15:** The stress field for edge and screw dislocations. (a) Stress distribution calculated via classical solutions [82] for a single edge dislocation with isotropic materials property. (b) & (c) Stress distribution calculated via generalized solutions [87] for a single edge dislocation with isotropic and anisotropic materials property, respectively. (d) & (e) Stress distribution for varied Burger's vector directions where generalized solutions for a single edge dislocation with anisotropic materials property are adapted. (f) Stress distribution calculated via classical solutions [82] for a single screw dislocation with isotropic materials property. (g) & (h) Stress distribution calculated via generalized solutions [87] for a single screw dislocation with isotropic and anisotropic material properties, respectively.

## 4.5 Stress Field for Multiple Dislocations

In real cases, multiple dislocations usually co-exist and interact with each other in the crystal; therefore I use the superposition method to investigate stress fields and forces between multiple dislocations. The stress fields manifesting between dislocations are numerically calculated and anisotropic material properties of electrodes are employed.

Anisotropic material properties of  $\text{LiFePO}_4$  are employed [83]. To investigate stress variations for arbitrary dislocation directions and how dislocations interact with each other, two dislocations with different Burger's vectors are incorporated. For dislocation number 1, the Burger's vectors are varied from  $(b_x=1, b_y=0)$  (Figure 4.16(a)),  $(b_x=1, b_y=0.6)$  to  $(b_x=0, b_y=0.6)$  (Figure 4.16(b)). Dislocation number 2 is fixed in its direction. The stress fields manifesting between dislocations are numerically calculated via Mathematica (Wolfram Research, Champaign, IL), and the superposition method with the elasticity solution of dislocations are utilized [87, 91].

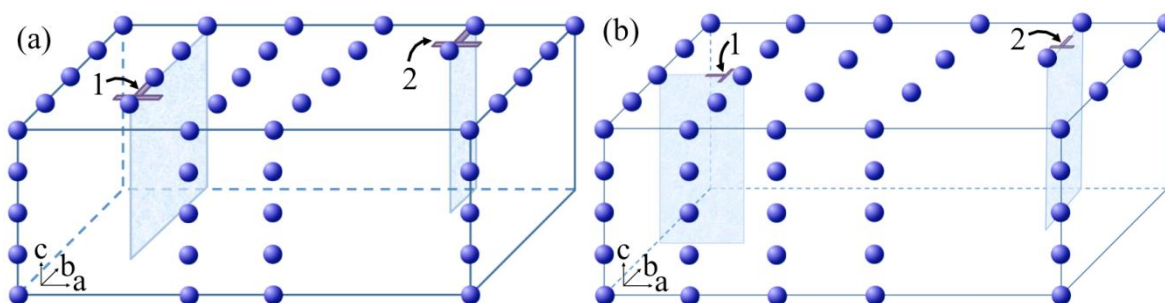


**Figure 4.16:** Representative multiple edge dislocation distributions in  $\text{LiFePO}_4$  crystals. For dislocation number 1, the Burger's vectors is varied from  $(b_x=1, b_y=0)$  in (a) to  $(b_x=0, b_y=0.6)$  in (b). Dislocation number 2 is fixed in its direction.

With the anisotropic solution (model B) and superposition method, I provide multiple dislocation stress distributions for  $\text{LiFePO}_4$  crystals (Figure 4.17). Representative results are shown in Figure 4.17 in which the edge dislocation 1 is located at  $(x, y)=(-20L, -12L)$  and the dislocation 2 is located at  $(x, y)=(40L, 24L)$  in our  $100L \times 60L$  model. Six components of stress caused by multiple dislocations with different Burger's vectors are numerically calculated. As for two edge dislocations, the stress field on the  $ab$ -plane is calculated by varying Burger's vector directions of dislocation 1 when dislocation 2 is fixed in its direction: the Burger's vectors is varied from  $(b_x=1, b_y=0)$  in (Figure 4.17(a)) to  $(b_x=1, b_y=0.6)$  in (Figure 4.17(b)) to  $(b_x=0, b_y=0.6)$  in (Figure 4.17(c)). Comparing (Figure 4.17(a)) to (Figure 4.17(c)), the results reveal that the mechanical stresses are dislocation direction and location dependent, suggesting that the greater distance between two dislocations, the lower mechanical stresses are generated between these the defects. It is also observed that mechanical stresses between two edge dislocations could be minimized when they are orthogonal to each other, suggesting the distribution of dislocation in Figure 4.16(b) is more preferable than one in Figure 4.16(a). Since it is likely to generate a dislocation configuration under high rate discharging, as shown in Figure 4.16(a), one could deduce that higher mechanical stresses are generated due to fast lithium intercalations. Studies have shown that while increasing the discharging rate, the capacity decreases [53], and the current study provides a link between mechanical stresses and the measured electrochemical performance. Similarly, the stress field of screw dislocation interactions is shown in Figure 4.17(d), where Burger's vector is  $b_z = 0.47$ . Moreover, the stress field for the screw dislocation is derived via the displacement in the  $c$ -direction, therefore Burger's vectors in

the x and y directions are unavailable. In general, the results reveal that the mechanical stresses are dislocation direction and location dependent, suggesting that the greater distance between two dislocations, the lower mechanical stresses are generated between these the defects.

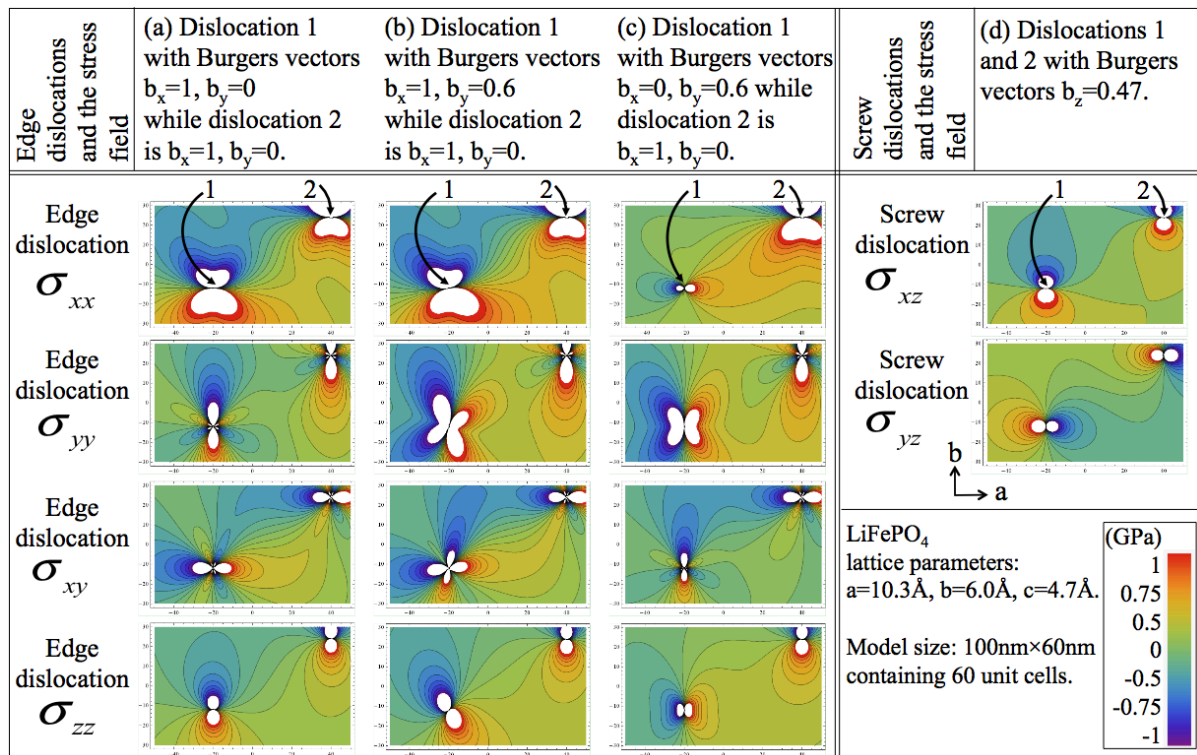


**Figure 4.17:** Stress field for multiple edge and screw dislocations. **(a)** The stress field on the ab-plane is calculated by varying Berger's vector directions of dislocation 1 when dislocation 2 is fixed in its direction, where the Burger's vector of dislocation 1 is  $(b_x=1, b_y=0)$ . **(b)** The stress distribution between two edge dislocations for which the Berger's vector of dislocation 1 is  $(b_x=1, b_y=0.6)$ . **(c)** The stress distribution between two edge dislocations for which the Berger's vector of dislocation 1 is  $(b_x=0, b_y=0.6)$ . **(d)** The stress distribution between two screw dislocations for which the Berger's vector of dislocation 1 is  $(b_z=0.47)$ .

#### 4.6 Force Field between Dislocations

The stresses created by dislocations can act on other neighboring dislocations. When two or more dislocations are close, they will experience forces due to the stress field created by each others. Once the forces between dislocations are big enough and exceed the critical value, they will start moving and thus glide or climb type motion will appear in crystal structures. Glide occurs when the dislocation moves in the surface which contains both its line and Burgers vector. Climb occurs when the dislocation moves out of the glide surface, and thus normal to the Burgers vector. To investigate the two types of movements of dislocation, the determination of magnitude of dislocation forces in glide direction and climb direction are in need. There are several methods to determine the forces between two dislocation lines, most of which reached the same numerical equation result [92]:

$$[F_{1to2}] = [\sigma_1][b_2] \times [t_2]$$

The equation 1 provided a solution for the reaction forces between two neighboring dislocations (dislocation #1 and #2, namely). In equation 1,  $[F_{1to2}]$  is a  $3 \times 1$  vector that represents the force from dislocation #1 to dislocation #2. And its three elements represent the three force components in three directions  $[F_x, F_y, F_z]$ .  $[\sigma_1]$  is a  $3 \times 3$  matrix that represents the stress field generated by dislocation #1.  $[b_2]$  is a  $3 \times 1$  vector that represents the Burgers vector direction and magnitude of dislocation #2.  $[t_2]$  is a  $3 \times 1$  vector that represents the sense vector, which is the dislocation line direction of dislocation #2. When knowing the

stress field of dislocation #1 and the Burgers vector and sense vector of dislocation #2, magnitudes in x, y, z directions of the force from dislocation #1 to #2 could be determined. Then glide component and climb component of the forces could be further determined.

With the above vector multiplication solution and the dislocation stress distribution achieved in previous part, I plotted the dislocation force field in  $\text{LiFePO}_4$  cathode material. The force between two edge dislocation lines that parallel to z-direction ( $[t]$  is the normal direction of the ab-plane) (Figure 4.18), for example, could be plotted by following these procedures: put the edge dislocation #1 at a fixed position (point (0, 0) at our case)  $\rightarrow$  put edge dislocation #2 at any position, calculate the force it experiences from edge dislocation #1, and record the force magnitude, direction at that position  $\rightarrow$  move edge dislocation #2 to a new position and repeat the calculation and data recording steps  $\rightarrow$  keep moving dislocation #2 around edge dislocation #1 until I have the force data at everywhere, then I could plot the force field applying from dislocation #1 to #2 with different color representing different force magnitude in x direction and y direction separately. Here  $[\sigma]$  is the stress field of dislocation 1, and  $[b]$  is the Burger's vector of dislocation 2. Dislocation 1 is assumed to locate at the origin with a Burger's vector  $b_1=(b_x=1, b_y=0)$ . The force field changes due to the direction of dislocation 2.

It is easy to determine the glide force and climb force from the provided force plot figure. In Figure 4.18(a) which the dislocation #2 has the Burgers vector  $(b_x=1, b_y=0)$ , for instance, the glide force is along x axis and thus the glide force is  $F_{xx}$ , and the climb force is along y axis and thus the glide force is  $F_{yy}$ . If the dislocation #2 lays in dark red area to dislocation #1's left, it experiences 1N glide force and 0 N climb force. In general, gliding occurs more

easily than climbing because it is a more energy favorable movement. For the glide motion, it is found that the glide most likely occurs on (100) and (010) planes due to the lowest energy requirement [88, 93]. In conclusion, the dislocation force field is similar to the cases of electron and electric field. However, unlike the electrons that could move freely under electronic field, a dislocation also suffers from forces that prevent its movement. So it only starts moving when the driving force exceeds a critical value. And the moving speed depends on both the net force it experienced and the material it lays in. As we could see now, the force data I provided could be very useful to predict the dislocation movements and could benefit the future battery development research.

Forces of attraction or repulsion between two edge dislocations are position and direction dependent, as shown in Figure 4.18. The result shows that the force field changes according to the Burger's vector direction of the dislocation 2: from  $b_2=(b_x=1, b_y=0)$  in Figure 4.18 (a) and (e), to  $b_2=(b_x=1, b_y=0.6)$  in Figure 4.18 (b) and (f), to  $b_2=(b_x=0, b_y=0.6)$  in Figure 4.18 (c) and (g), and to  $b_2=(b_x=-1, b_y=0)$  in Figure 4.18 (d) and (h). Equal and opposite forces act on the dislocation 1, assuming it locates at the origin with a Burger's vector  $b_1=(b_x=1, b_y=0)$ . Comparing with the force field in Figure 4.18 (a) (e) and the ones in Figure 4.18 (c) (g) and Figure 4.18 (d) (h), it is suggested that force values for arbitrary Burger's vector's directions could be simply calculated by utilizing linear transformations. For two parallel edge dislocations (Fig. 4.18 (a) (e) and Fig. 4.18 (d) (h)), the closer they are, the stronger attractive or repulsive forces are between them, suggesting the dislocations tend to reduce the total elastic energy by repelling each other. As for two parallel edge dislocations with the same Burgers vectors (Fig. 4.18 (a) (e)) or opposite Burgers vectors (Fig. 4.18 (d) (h)), similar but

opposite effects occur, and it is suggested two dislocations with opposite signs tend to meet each other and cancel out the forces between them. The phenomenon shows the tendency of minimizing the system energy. The force field studied here has been limited to the edge dislocations; however, the extension of the method to other types of dislocation is straightforward. The result from the current study suggests that the force field might be one key factor that repel or attract lithium ions in the crystal and results in the capacity fade in lithium-ion batteries.

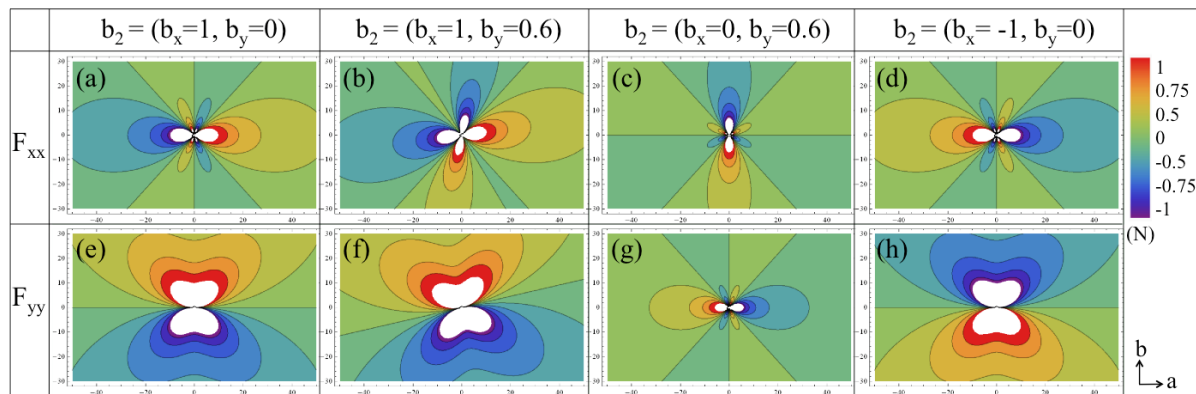


**Figure 4.18:** The force field of dislocation interactions. The force field changes due to the direction of dislocation 2. (a) and (e):  $b_x=1, b_y=0$ ; (b) and (f):  $b_x=1, b_y=0.6$ ; (c) and (g):  $b_x=0, b_y=0.6$ ; (d) and (h):  $b_x=-1, b_y=0$ . Equal and opposite forces act on dislocation 1. Warm color represents positive force, which means it push/pull the dislocation towards positive direction of x/y axis, and vice versa.

The accumulation of glide will finally cause cracks and even further structural failure. Cracks in cathode material particles, as suggested [94-96], could limit the electron/Li-ions diffusion rate and increase battery impedance of  $\text{LiFePO}_4$  batteries. With lower diffusion rate, the  $\text{LiFePO}_4$  cathode material would not be able to match the high charging/discharging rate. Thus the rate capacity decreases and cathode material degradation occurs. Moreover, cracks will create smaller particles and larger surface area, which could increase heat absorption [97] and aggravate side reactions such as the dissolution of transition metal in

electrolytes [98]. Therefore, the better understanding of the mechanism and plausible models to depict cathode material structural failures due to delithiation in our works are helpful.

## **CHAPTER 5      LiFePO<sub>4</sub> CATHODE MATERIAL FRACTURE ACCOMMODATED TO DISLOCATION MOVEMENT**

### **5.1 Dislocation Movement**

In this part, I report that the mechanical and structural failures are attributed to dislocations formations. I also provide analytical models of stress distribution generated by multiple dislocations and crystal visualizations of crack formation for further understanding the stress development and failure mechanisms due to lithium diffusions during charging or discharging.

### **5.2 Lithium Ion Diffusion and Dislocation Formation**

During charging and discharging process, lithium ions shuttle between cathode and anode materials to generate electricity. The cathode materials, such as LiFePO<sub>4</sub>, typically exhibit layered structures amenable to lithium ion storage (Figure 5.1(b)). For LiFePO<sub>4</sub> cathode material, the supporting matrix structure is made up by FePO<sub>4</sub>, a matrix structure that could store lithium ions and let them travel in and out dynamically. It has been suggested that lithium ions travel in and out along tunnels in the *b*-direction, therefore LiFePO<sub>4</sub> crystals are filled with lithium ions layer by layer (Figure 5.1(b)) [68, 69]. Because the energy needed for lithium ions travel in *b*-direction is lower than that in other directions[69, 99].

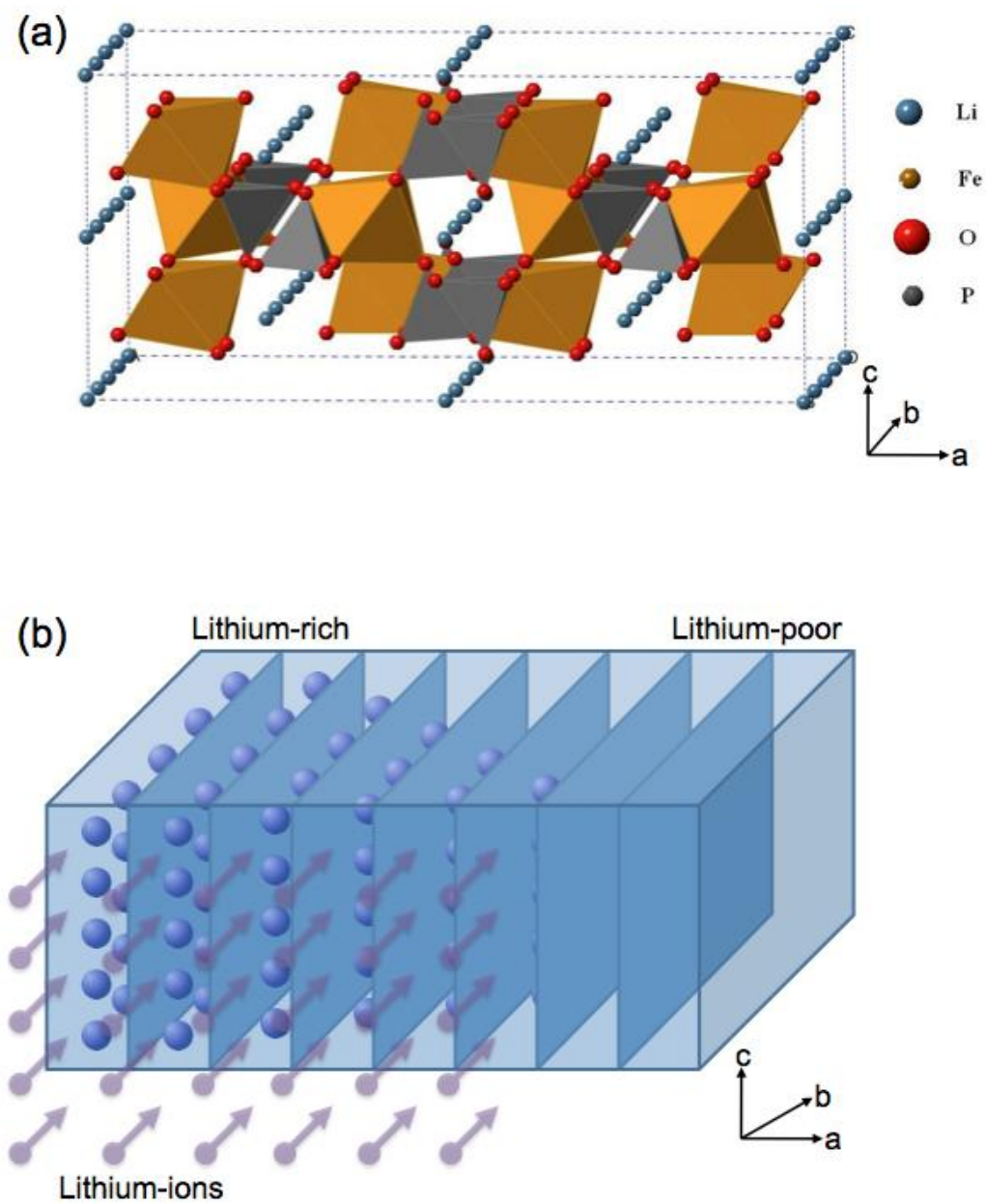


**Figure 5.1:** (a)  $\text{LiFePO}_4$  crystal structure of eight unit cells. (b) Lithium ions diffusion along the b-direction in  $\text{LiFePO}_4$  material during the discharging process (fill the crystal layer by layer in the a-direction).

During repetitive and fast lithium intercalations, one or two layers in  $\text{LiFePO}_4$  might be only half-filled or skipped entirely [41, 43]. In this case, the crystal would then be filled with more lithium ions at one end than the other, thus generating extra-half planes with mixed edge and screw dislocations. In previous study, I reported that the mechanical and structural failures of cathode materials are attributed to dislocations formations. When experiencing a big enough glide force, dislocations will start moving and thus gliding will appear in crystal structures. The accumulation of glide will finally cause cracks and further structural failure. From published experimental observations [69] [88], fractures have been observed to be parallel to the c-direction, (001). In the present study, I consider three possible dislocation distributions caused by coupled mechanics-structure-electrochemistry interactions; these distributions could all result in an observed (001) crack and the fracture surfaces are oriented parallel to (100) or (010) planes.

### **5.3 Dislocation based Fracture**

#### **5.3.1 Edge dislocation based mode I fracture**

In the case of one or two layers in  $\text{LiFePO}_4$  crystal be only half-filled during lithium intercalations, an edge dislocation with a (100) extra half-plane and a (010) glide plane occurs (Figure 5.2 (a)). During repetitive and fast lithium intercalations, the dislocations would result in a crack surface normal to (010) where a crack line is parallel to (001) (Figure 5.2 (b)). The dislocation experiences glide forces or the crystal particle experiences shear

forces along the  $a$ -direction, suggesting a mode I fracture caused by the accumulated dislocations due to lithium intercalations (Figure 5.2 (c)), as observed from the experiments [69] [88].

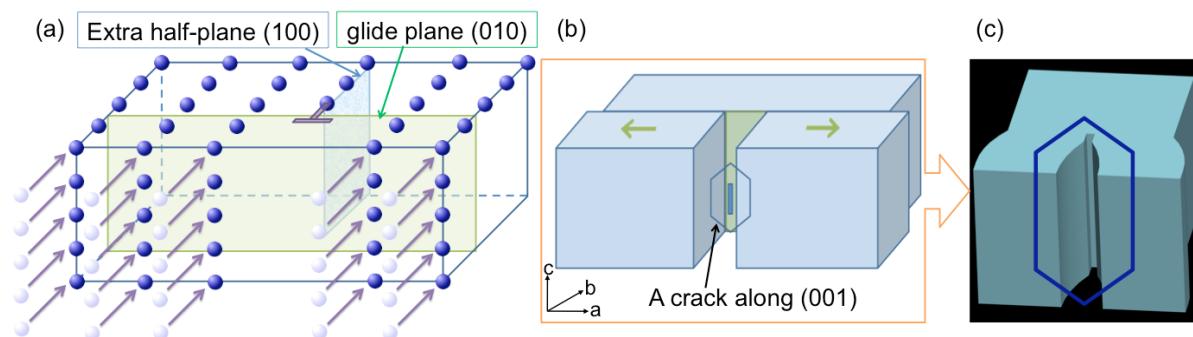


**Figure 5.2:** (a) Kinetics of the formation of the  $[100]$  edge dislocation and  $(010)$  glide plane in  $\text{LiFePO}_4$  crystal during Lithium ions diffusion. (b) Mechanism of the dislocations gliding resulting in a crack surface normal to  $(010)$  where a crack line is parallel to  $(001)$  [88]. (c) Mode I fracture caused by the accumulated dislocations.

### 5.3.2 Edge dislocation based mode II fracture:

Due to repetitive and fast lithium intercalations,  $\text{LiFePO}_4$  crystal might be filled with lithium ions inhomogeneously where the crystal has more lithium ions at one end than the other; an edge dislocation with a  $(010)$  extra half-plane and a  $(100)$  glide plane is formed (Figure 5.3 (a)). In this case, dislocations accumulate and result in a crack line parallel to  $(001)$  and a fracture surface parallel to  $(100)$  plane (Figure 5.3 (b)). The dislocation experiences glide forces or the crystal particle experiences shear forces along the  $b$ -direction, suggesting a mode II fracture caused by the accumulated dislocations (Figure 5.3 (c)), as observed from the experiments [88].

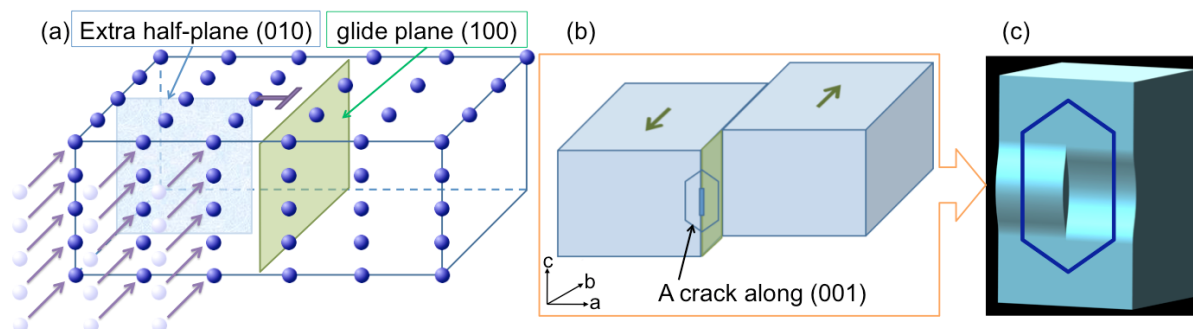


**Figure 5.3:** (a) Kinetics of the formation of the [010] edge dislocation and (100) glide plane in  $\text{LiFePO}_4$  crystal during Lithium ions diffusion.  $\text{LiFePO}_4$  crystal might be filled with lithium ions inhomogeneously. (b) Mechanism of the dislocations gliding resulting in a crack surface normal to (010) where a crack line is parallel to (001) [88]. (c) Mode II fracture caused by the accumulated dislocations.

### 5.3.3 Screw dislocation based mode III fracture:

Oftentimes, layers in  $\text{LiFePO}_4$  might not be fully filled during lithium intercalation, and the crystal would have more lithium ions at one region than the other. A right-handed screw glides toward the left to extend the surface step in the required manner. Therefore, a screw dislocation with a [001] Burger's vector, a (100) extra half-plane, and a (100) glide plane is formed (Figure 5.4 (a)). The dislocation experiences glide forces or the crystal particle experiences shear forces along  $c$ -direction, and the screw dislocation boundary would rotate with axis [100]. Accumulated screw dislocations would result in a crack line parallel to (001) and a fracture surface parallel to (100) plane (Figure 5.4 (b)). It is suggested a mode III fracture caused by the accumulated dislocations (Figure 5.4 (c)), as observed from the experiments [88].

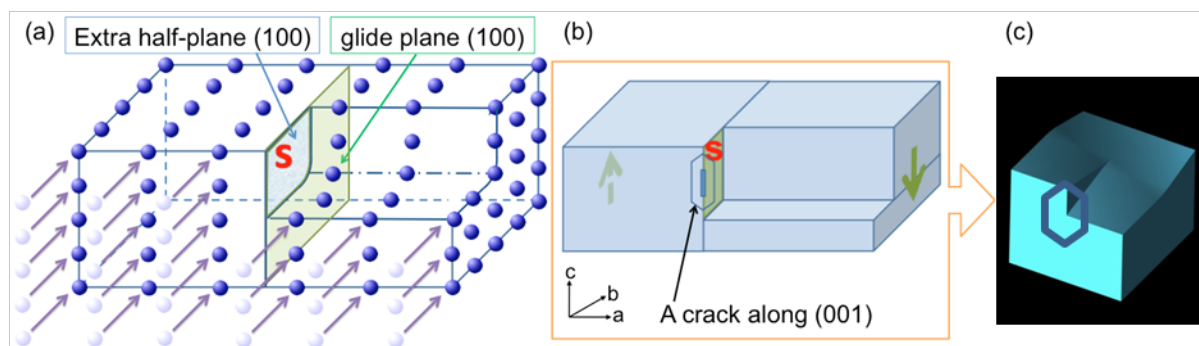


**Figure 5.4:** (a) Kinetics of the formation of the [001] screw dislocation and (100) glide plane in  $\text{LiFePO}_4$  crystal during Lithium ions diffusion.  $\text{LiFePO}_4$  crystal might be filled with lithium ions inhomogeneously. (b) Mechanism of the dislocations gliding resulting in a crack surface normal to (010) where a crack line is parallel to (001) [88]. (c) Mode III fracture caused by the accumulated dislocations.

## CHAPTER 6 CONCLUSION

This study provides an overview of four mainstream lithium-ion battery cathode materials. Characteristics of  $\text{LiCoO}_2$ ,  $\text{LiMn}_2\text{O}_4$ ,  $\text{LiNiO}_2$ , and  $\text{LiFePO}_4$  were collected and compared. Specifically, I focused on specifications for (1) volumetric power and energy densities, (2) gravimetric power and energy densities, (3) stability, safety and environmental factors, and (4) capacity and rate-capacity. Since synthetic methods are different for the four different cathode materials, only the representative data that appeared most frequently within the past five years were chosen to ensure that data from different literature sources are comparable. Current electrochemical technology is still limited to developing cathode materials to achieve EV goals set by the USABC. The main obstacle for advanced rechargeable batteries is found in the rate-capacity loss at high C-rate discharging, and it is currently one of the most challenging issues in developing energy storage systems for EV/HEV/PHEV. The enhancement of rate-capacity retention is the primary design goal of battery chemistry in the electrochemical community.

Moreover, I report that the mechanical and structural failures are attributed to dislocation formations. Analytical models and crystal visualizations provide details for further understanding the stress developments due to lithium movement during charging or discharging. In the present study, I report three different lithium intercalation-induced dislocation mechanisms explaining experimental observed cracks. The theory of elasticity to calculate dislocation stress fields was used. In most cases, dislocations are not perfectly parallel to one specific axis. Therefore, stress variations for arbitrary dislocation directions

are investigated. In addition, multiple dislocations usually co-exist and interact with each other in the crystal; therefore I use the superposition method to investigate stress fields and forces between multiple dislocations. The stress fields manifesting between dislocations are numerically calculated via Mathematica (Wolfram Research, Champaign, IL), and anisotropic material properties of electrodes are employed. The results provide links between stress fields and the observed structural failure in lithium-ion batteries. This study contributes to the fundamental understanding of the mechanisms of capacity loss in lithium-ion battery materials and helps the design of better rechargeable batteries, and thus leads to economic and environmental benefits.

## REFERENCES

- [1] U.S. Department of Energy, 2010, "Monthly Energy Review," U.S. Energy Administration, DOE/EIA-0035(2010/12), Office of Energy Statistics, U.S. Department of Energy, Washington, DC 20585.
- [2] U.S. Department of Energy, 2009, "Emissions of Greenhouse Gases in the United States, 2008," U.S. Energy Administration, DOE/EIA-0573(2008), Office of Energy Statistics, U.S. Department of Energy, Washington, DC 20585.
- [3] Cutler J. Cleveland, 2004, "Encyclopedia of Energy," Elsevier, New York, .
- [4] Kurzweil, P., 2009, "Encyclopedia of Electrochemical Power Sources," Elsevier, Amsterdam, pp. 607-633.
- [5] Ibrahim, H., Ilinca, A., and Perron, J., 2008, "Energy Storage systems—Characteristics and Comparisons," *Renewable and Sustainable Energy Reviews*, **12**(5) pp. 1221-1250.
- [6] Gao, X. P., and Yang, H. X., 2010, "Multi-Electron Reaction Materials for High Energy Density Batteries," *Energy & Environmental Science*, **3**(2) pp. 174-189.
- [7] Chang, H., Wu, H., and Wu, N., 2008, "Enhanced High-Temperature Cycle Performance of LiFePO<sub>4</sub>/carbon Batteries by an Ion-Sieving Metal Coating on Negative Electrode," *Electrochemistry Communications*, **10**(12) pp. 1823-1826.

- [8] Masarapu, C., Subramanian, V., Zhu, H., 2009, "Long-Cycle Electrochemical Behavior of Multiwall Carbon Nanotubes Synthesized on Stainless Steel in Li Ion Batteries," *Advanced Functional Materials*, **19**(7) pp. 1008-1014.
- [9] Liu, P., Sherman, E., and Verbrugge, M., 2010, "Electrochemical and Structural Characterization of Lithium Titanate Electrodes," *Journal of Solid State Electrochemistry*, **14**(4) pp. 585-591.
- [10] Chan, C. K., Peng, H., Liu, G., 2008, "High-Performance Lithium Battery Anodes using Silicon Nanowires," *Nature Nanotechnology*, **3**(1) pp. 31-35.
- [11] Goodenough, J. B., and Kim, Y., 2010, "Challenges for Rechargeable Li Batteries," *Chemistry of Materials*, **22**(3) pp. 587-603.
- [12] Thackeray, M., Shao-Horn, Y., Kahaian, A., 1998, "Structural Fatigue in Spinel Electrodes in High Voltage (4V) Li/LixMn2O4 Cells," *Electrochemical and Solid State Letters*, **1**(1) pp. 7-9.
- [13] Padhi, A. K., Nanjundaswamy, K. S., and Goodenough, J. B., 1997, "Phospho-Olivines as Positive-Electrode Materials for Rechargeable Lithium Batteries," *Journal of the Electrochemical Society*, **144**(4) pp. 1188-1194.
- [14] Manthiram, A., Pasquali, M., Passerini, S., 2003, "Lithium batteries: science and technology," Springer, Kluwer Academic Publishers, Springer Science+Business Media, LLC, 233 Spring Street, New York, USA, 10013, pp. 728.

- [15] Takahashi, Y., Tode, S., Kinoshita, A., 2008, "Development of Lithium-Ion Batteries with a  $\text{LiCoO}_2$  Cathode Toward High Capacity by Elevating Charging Potential," *Journal of the Electrochemical Society*, **155**(7) pp. 537-541.
- [16] Choi, K., Jeon, J., Park, H., 2010, "Electrochemical Performance and Thermal Stability of  $\text{LiCoO}_2$  Cathodes Surface-Modified with a Sputtered Thin Film of Lithium Phosphorus Oxynitride," *Journal of Power Sources*, **195**(24) pp. 8317-8321.
- [17] Huang, Y., Li, J., and Jia, D., 2004, "Preparation and Characterization of  $\text{LiMn}_2\text{O}_4$ ; Nanorod by Low Heating Solid State Coordination Method," *Journal of Nanoparticle Research*, **6**(5) pp. 533-538.
- [18] OHZUKU, T., KITAGAWA, M., and HIRAI, T., 1990, "Electrochemistry of Manganese-Dioxide in Lithium Nonaqueous Cell .2. X-Ray Diffractonal and Electrochemical Characterization on Deep Discharge Products of Electrolytic Manganese-Dioxide," *Journal of the Electrochemical Society*, **137**(1) pp. 40-46.
- [19] Aoshima, T., Okahara, K., Kiyohara, C., 2001, "Mechanisms of Manganese Spinels Dissolution and Capacity Fade at High Temperature," *Journal of Power Sources*, **97-98**pp. 377-380.
- [20] Liu, H., and Tang, D., 2009, "The Effect of Nanolayer  $\text{AlF}_3$  Coating on  $\text{LiMn}_2\text{O}_4$  Cycle Life in High Temperature for Lithium Secondary Batteries," *Russian Journal of Electrochemistry*, **45**(7) pp. 762-764.

- [21] Han, C., Kim, J., Paeng, S., 2009, "Electrochemical Characteristics of LiNiO<sub>2</sub> Films Prepared for Charge Storable Electrode Application," *Thin Solid Films*, **517**(14) pp. 4215-4217.
- [22] Fu, X., Wang, X., Peng, H., 2010, "Low Temperature Synthesis of LiNiO<sub>2</sub>@LiCoO<sub>2</sub> as Cathode Materials for Lithium Ion Batteries," *Journal of Solid State Electrochemistry*, **14**(6) pp. 1117-1124.
- [23] Nagasubramanian, G., 2002, *Proceedings of the 40th Power Sources Conference*, Anonymous Cherry Hill, NJ, pp. 434.
- [24] Takahashi, M., Tobishima, S., Takei, K., 2002, "Reaction Behavior of LiFePO<sub>4</sub> as a Cathode Material for Rechargeable Lithium Batteries," *Solid State Ionics*, **148**(3-4) pp. 283-289.
- [25] STRELTSOV, V., BELOKONEVA, E., TSIRELSON, V., 1993, "Multipole Analysis of the Electron-Density in Triphylite, LiFePO<sub>4</sub>, using X-Ray-Diffraction Data," *Acta Crystallographica Section B-Structural Science*, **49**pp. 147-153.
- [26] Andersson, A. S., and Thomas, J. O., 2001, "The Source of First-Cycle Capacity Loss in LiFePO<sub>4</sub>," *Journal of Power Sources*, **97-98**pp. 498-502.
- [27] Awarke, A., Lauer, S., Pischinger, S., 2011, "Percolation-Tunneling Modeling for the Study of the Electric Conductivity in LiFePO<sub>4</sub> Based Li-Ion Battery Cathodes," *Journal of Power Sources*, **196**(1) pp. 405-411.

- [28] Chung, S., Bloking, J. T., and Chiang, Y., 2002, "Electronically Conductive Phospho-Olivines as Lithium Storage Electrodes," **1**(2) pp. 128.
- [29] Ravet, N., Chouinard, Y., Magnan, J., 2001, "Electroactivity of Natural and Synthetic Triphylite," *Journal of Power Sources*, **97-8**pp. 503-507.
- [30] Park, K., Schougaard, S. B., and Goodenough, J. B., 2007, "Conducting-polymer/iron-Redox-Couple Composite Cathodes for Lithium Secondary Batteries," *Advanced Materials*, **19**(6) pp. 848-+.
- [31] Cheon, S. E., Kwon, C. W., Kim, D. B., 2000, "Effect of Binary Conductive Agents in LiCoO<sub>2</sub> Cathode on Performances of Lithium Ion Polymer Battery," *Electrochimica Acta*, **46**(4) pp. 599-605.
- [32] Shaju, K. M., and Bruce, P. G., 2008, *Chem. Mater.*, **20**(17) pp. 5562.
- [33] U.S. Advanced Battery Consortium, 2006, "EV Battery Test Procedures Manual: Appendix G - USABC Criteria for Advanced Battery Technologies," .
- [34] Pasquier, A. D., Plitz, I., Gural, J., 2004, "Power-Ion Battery: Bridging the Gap between Li-Ion and Supercapacitor Chemistries," *Journal of Power Sources*, **136**(1) pp. 160-170.
- [35] Lu, W., Lee, C. W., Venkatachalapathy, R., 2000, "Electrochemical and Thermal Behaviour of LiNi<sub>0.8</sub>Co<sub>0.2</sub>O<sub>2</sub> Cathode in Sealed 18650 Li-Ion Cells," *Journal of Applied Electrochemistry*, **30**(10) pp. 1119-1124.

- [36] Chen, Y. H., Tang, Z. Y., Lu, X. H., 2006, "Research of Explosion Mechanism of Lithium-Ion Battery," *Progress in Chemistry*, **18**(6) pp. 823-831.
- [37] Xia, Y., Fujieda, T., Tatsumi, K., 2001, "Thermal and Electrochemical Stability of Cathode Materials in Solid Polymer Electrolyte," *Journal of Power Sources*, **92**(1-2) pp. 234-243.
- [38] Yuan, L., Wang, Z., Zhang, W., 2011, "Development and Challenges of LiFePO<sub>4</sub> Cathode Material for Lithium-Ion Batteries," *Energy & Environmental Science*, **4**(2) pp. 269-284.
- [39] Shim, J., and Striebel, K. A., 2003, "Cycling Performance of Low-Cost Lithium Ion Batteries with Natural Graphite and LiFePO<sub>4</sub>," *Journal of Power Sources*, **119**pp. 955-958.
- [40] DiLeo, R. A., Castiglia, A., Ganter, M. J., 2010, "Enhanced Capacity and Rate Capability of Carbon Nanotube Based Anodes with Titanium Contacts for Lithium Ion Batteries," *Acs Nano*, **4**(10) pp. 6121-6131.
- [41] Vetter, J., 2005, "Ageing Mechanisms in Lithium-Ion Batteries," *Journal of Power Sources*, **147**(1-2) pp. 269.
- [42] Belov, D., and Yang, M., 2008, "Failure Mechanism of Li-Ion Battery at Overcharge Conditions," *Journal of Solid State Electrochemistry*, **12**(7-8) pp. 885-894.
- [43] Broussely, M., Biensan, P., Bonhomme, F., 2005, "Main Aging Mechanisms in Li Ion Batteries," *Journal of Power Sources*, **146**(1-2) pp. 90-96.

- [44] Chen, G., and Richardson, T., 2009, "Solid Solution Phases in the Olivine-Type LiMnPO<sub>4</sub>/MnPO<sub>4</sub> System," *Journal of the Electrochemical Society*, **156**(9) pp. A756.
- [45] Sun, Y. C., Wang, Z. X., Chen, L. Q., 2003, "Improved Electrochemical Performances of Surface-Modified Spinel LiMn<sub>2</sub>O<sub>4</sub> for Long Cycle Life Lithium-Ion Batteries," *Journal of the Electrochemical Society*, **150**(10) pp. A1294-A1298.
- [46] Song, G., Wu, Y., Xu, Q., 2010, "Enhanced Electrochemical Properties of LiFePO<sub>4</sub> Cathode for Li-Ion Batteries with Amorphous NiP Coating," *Journal of Power Sources*, **195**(12) pp. 3913-3917.
- [47] Shenouda, A. Y., and Liu, H. K., 2009, "Studies on Electrochemical Behaviour of Zinc-Doped LiFePO<sub>4</sub> for Lithium Battery Positive Electrode," *Journal of Alloys and Compounds*, **477**(1-2) pp. 498-503.
- [48] Meethong, N., Huang, H. Y. S., Carter, W. C., 2007, "Size-Dependent Lithium Miscibility Gap in Nanoscale Li<sub>1-x</sub>FePO<sub>4</sub>," *Electrochemical and Solid State Letters*, **10**(5) pp. A134-A138.
- [49] Chen, G., and Richardson, T., 2010, "Thermal Instability of Olivine-Type LiMnPO<sub>4</sub> Cathodes," *Journal of Power Sources*, **195**(4) pp. 1221.
- [50] Cuisinier, M., Martin, J., Dupré, N., 2010, "Moisture Driven Aging Mechanism of LiFePO<sub>4</sub> Subjected to Air Exposure," *Electrochemistry Communications*, **12**(2) pp. 238-241.

[51] Tanguy, F., Gaubicher, J., Gaillot, A., 2009, "Lowering Interfacial Chemical Reactivity of Oxide Materials for Lithium Batteries. A Molecular Grafting Approach," *Journal of Materials Chemistry*, **19**(27) pp. 4771-4777.

[52] Vidu, R., and Stroeve, P., 2004, "Improvement of the Thermal Stability of Li-Ion Batteries by Polymer Coating of  $\text{LiMn}_2\text{O}_4$ ," *Industrial & Engineering Chemistry Research*, **43**(13) pp. 3314-3324.

[53] Kang, B., and Ceder, G., 2009, "Battery Materials for Ultrafast Charging and Discharging," *Nature*, **458**(7235) pp. 190-193.

[54] Cuisinier, M., Martin, J., Dupré, N., 2010, "Moisture Driven Aging Mechanism of  $\text{LiFePO}_4$  Subjected to Air Exposure," *Electrochemistry Communications*, **12**(2) pp. 238-241.

[55] Yamada, A., Koizumi, H., Nishimura, S., 2006, "Room-Temperature Miscibility Gap in  $\text{Li}_x\text{FePO}_4$ ," **5**(5) pp. 360.

[56] Duong, T., 2010, "Directions for Energy Storage R&D in the Vehicle Technologies Program," *Symposium on Energy Storage Beyond Lithium Ion: Materials Perspectives*, Anonymous .

[57] Chen, Y., Hu, C., and Li, Y., 2010, "Effects of Cathode Impedance on the Performances of Power-Oriented Lithium Ion Batteries," *Journal of Applied Electrochemistry*, **40**(2) pp. 277-284.

- [58] Du Pasquier, A., Huang, C. C., and Spitler, T., 2009, "Nano  $\text{Li}_4\text{Ti}_5\text{O}_{12}$ - $\text{LiMn}_2\text{O}_4$  Batteries with High Power Capability and Improved Cycle-Life," *Journal of Power Sources*, **186**(2) pp. 508-514.
- [59] Aurbach, D., Markovsky, B., Salitra, G., 2007, "Review on Electrode-Electrolyte Solution Interactions, Related to Cathode Materials for Li-Ion Batteries," *Journal of Power Sources*, **165**(2) pp. 491-499.
- [60] Fu, L. J., Liu, H., Li, C., 2006, "Surface Modifications of Electrode Materials for Lithium Ion Batteries," *Solid State Sciences*, **8**(2) pp. 113-128.
- [61] Sun, Y. K., Hong, K. J., Prakash, J., 2002, "Electrochemical Performance of Nano-Sized ZnO-Coated  $\text{LiNi}_{0.5}\text{Mn}_{1.5}\text{O}_4$  Spinel as 5 V Materials at Elevated Temperatures," *Electrochemistry Communications*, **4**(4) pp. 344-348.
- [62] Julien, C., Rougier, A., and Nazri, G., 1997, "Synthesis, Structure, Lattice Dynamics and Electrochemistry of Lithiated Manganese Spinel,  $\text{LiMn}_2\text{O}_4$ ," *Solid-State Chemistry of Inorganic Materials*, **453**pp. 647-652.
- [63] DAHN, J., FULLER, E., OBROVAC, M., 1994, "Thermal-Stability of  $\text{Li}_x\text{CoO}_2$ ,  $\text{Li}_x\text{NiO}_2$  and  $\lambda\text{-MnO}_2$  and Consequences for the Safety of Li-Ion Cells," *Solid State Ionics*, **69**(3-4) pp. 265-270.

[64] MacNeil, D., and Dahn, J., 2001, "The Reaction of Charged Cathodes with Nonaqueous Solvents and Electrolytes - I.  $\text{Li}_{0.5}\text{CoO}_2$ ," *Journal of the Electrochemical Society*, **148**(11) pp. A1205-A1210.

[65] Yamada, A., Koizumi, H., Sonoyama, N., 2005, "Phase Change in  $\text{Li}_x\text{FePO}_4$ ," *Electrochemical and Solid State Letters*, **8**(8) pp. A409-A413.

[66] Liu, Z., and Huang, X., 2010, "Factors that Affect Activation Energy for Li Diffusion in  $\text{LiFePO}_4$ : A First-Principles Investigation," *Solid State Ionics*, **181**(19-20) pp. 907-913.

[67] Jahn, H. A., and Teller, E., 1937, "Stability of Polyatomic Molecules in Degenerate Electronic States. I. Orbital Degeneracy," *Proceedings of the Royal Society of London. Series A - Mathematical and Physical Sciences*, **161**(905) pp. 220-235.

[68] Delmas, C., Maccario, M., Croguennec, L., 2008, "Lithium Deintercalation in  $\text{LiFePO}_4$  Nanoparticles Via a Domino-Cascade Model," *Nat Mater*, **7**(8) pp. 665-671.

[69] Chen, G., Song, X., and Richardson, T. J., 2006, "Electron Microscopy Study of the  $\text{LiFePO}_4$  to  $\text{FePO}_4$  Phase Transition," *Electrochemical and Solid-State Letters*, **9**(6) pp. A295-A298.

[70] Julien, C. M., Manger, A., Ait-Salah, A., 2007, "Nanoscope Scale Studies of  $\text{LiFePO}_4$  as Cathode Material in Lithium-Ion Batteries for HEV Application," *Ionics*, **13**(6) pp. 395-411.

- [71] Salah, A., Mauger, A., Julien, C., 2006, "Nano-Sized Impurity Phases in Relation to the Mode of Preparation of LiFePO<sub>4</sub>," *Materials Science and Engineering B-Solid State Materials for Advanced Technology*, **129**(1-3) pp. 232-244.
- [72] Doi, T., Kageura, J., Okada, S., 2008, "Surface Modification of LiNi<sub>1/2</sub>Mn<sub>3/2</sub>O<sub>4</sub> Thin-Films by Zirconium alkoxide/PMMA Composites and their Effects on Electrochemical Properties," *Journal of Power Sources*, **185**(1) pp. 473-479.
- [73] Changjiu, L., Huijing, W., Huabin, W., 2007, "Study on Physical Speciality and Electrochemical Characteristics of Electrode Material of Amorphous Nano-Ni(OH)<sub>2</sub>," *Rare Metal Materials and Engineering*, **36**(9) pp. 1545-1548.
- [74] Xia, Y., Kumada, N., and Yoshio, M., 2000, "Enhancing the Elevated Temperature Performance of Li/LiMn<sub>2</sub>O<sub>4</sub> Cells by Reducing LiMn<sub>2</sub>O<sub>4</sub> Surface Area," *Journal of Power Sources*, **90**(2) pp. 135-138.
- [75] Lanz, M., Kormann, C., and Novak, P., 2003, "A Procedure for Specific Charge and Cycling Performance Measurements on LiMn<sub>2</sub>O<sub>4</sub> Spinels for Lithium-Ion Batteries," *Journal of Solid State Electrochemistry*, **7**(9) pp. 658-664.
- [76] Broussely, A., Blanchard, P., Biensan, P., 2003, "Properties of Large Li Ion Cells using a Nickel Based Mixed Oxide," *Journal of Power Sources*, **119**pp. 859-864.

- [77] Albrecht, S., Kumpers, J., Kruft, M., 2003, "Electrochemical and Thermal Behavior of Aluminum- and Magnesium-Doped Spherical Lithium Nickel Cobalt Mixed Oxides  $\text{Li}_{1-x}(\text{Ni}_{1-y-z}\text{Co}_y\text{M}_z)\text{O}_2$  (M = Al, Mg)," *Journal of Power Sources*, **119**pp. 178-183.
- [78] Chen, G., Song, X., and Richardson, T., 2006, "Electron Microscopy Study of the  $\text{LiFePO}_4$  to  $\text{FePO}_4$  Phase Transition," *Electrochemical and Solid-State Letters*, **9**(6) pp. A295.
- [79] Bhandakkar, T. K., and Gao, H., 2010, "Cohesive Modeling of Crack Nucleation Under Diffusion Induced Stresses in a Thin Strip: Implications on the Critical Size for Flaw Tolerant Battery Electrodes," *International Journal of Solids and Structures*, **47**(10) pp. 1424-1434.
- [80] Cheng, Y. V., Mark W., 2010, "Diffusion-Induced Stress, Interfacial Charge Transfer, and Criteria for Avoiding Crack Initiation of Electrode Particles " *Journal of the Electrochemical Society*, **157**(4) pp. A508-A516.
- [81] Meethong, N., Huang, H. Y. S., Speakman, S. A., 2007, "Strain Accommodation during Phase Transformations in Olivine-Based Cathodes as a Materials Selection Criterion for High-Power Rechargeable Batteries," *Advanced Functional Materials*, **17**(7) pp. 1115-1123.
- [82] Hull, D., and Bacon, D.J., 2001, "Introduction to dislocations," Butterworth-Heinemann, Oxford Oxfordshire ; Boston, pp. 242.

- [83] Maxisch, T., and Ceder, G., 2006, "Elastic Properties of Olivine  $\text{Li}_x\text{FePO}_4$  from First Principles," *Physical Review B*, **73**(17) pp. 174112.
- [84] Eshelby, J. D., Read, W. T., and Shockley, W., 1953, "Anisotropic Elasticity with Applications to Dislocation Theory," *Acta Metallurgica*, **1**(3) pp. 251-259.
- [85] Heinisch, H. J., G. Sines, J. Goodman, 1975, "Elastic Stresses and Self-Energies of Dislocations of Arbitrary Orientation in Anisotropic Media: Olivine, Orthopyroxene, Calcite, and Quartz," *J. Geophys. Res.*, **80**(14) pp. 1885-1896.
- [86] Ohsawa, K., 2009, "Stress Function for Dislocation Loops in Anisotropic Crystals," *IOP Conference Series: Materials Science and Engineering*, **3**(1) pp. 012027.
- [87] Indenbom, L., 1992, "Elastic strain fields and dislocation mobility," Amsterdam ; New York : Elsevier Science Publishers ; New York, NY, USA : Sole distributor for the USA and Canada, Elsevier Science Pub., 1992, .
- [88] Gabrisch, H., Wilcox, J., and Doeff, M. M., 2008, "TEM Study of Fracturing in Spherical and Plate-Like  $\text{LiFePO}_4$  Particles," *Electrochemical and Solid State Letters*, **11**(3) pp. A25-A29.
- [89] Ceder, G., 2006, "Elastic Properties of Olivine  $\text{Li}_x\text{FePO}_4$  from First Principles," **73**(17) .
- [90] Hertzberg, R.W., 1995, "Deformation and Fracture Mechanics of Engineering Materials ," Wiley, New York, pp. 816.

- [91] Head, A. K., 1953, "Edge Dislocations in Inhomogeneous Media," Proceedings of the Physical Society of London Section B, **66**(405) pp. 793-801.
- [92] Bacon, D. J., Barnett, D. M., and Scattergood, R. O., 1980, "Anisotropic Continuum Theory of Lattice Defects," Progress in Materials Science, **23**pp. 51-262.
- [93] Williams, J. O., Thomas, J. M., Tennakoo, D., 1972, "Dislocations in Orthorhombic Minerals .1. Naturally-Occurring Barytes," Journal of the Chemical Society-Faraday Transactions i, **68**pp. 1987-&.
- [94] Deshpande, R., Cheng, Y., and Verbrugge, M. W., 2010, "Modeling Diffusion-Induced Stress in Nanowire Electrode Structures," Journal of Power Sources, **195**(15) pp. 5081-5088.
- [95] Xiao, X., Liu, P., Verbrugge, M. W., 2011, "Improved Cycling Stability of Silicon Thin Film Electrodes through Patterning for High Energy Density Lithium Batteries," Journal of Power Sources, **196**(3) pp. 1409-1416.
- [96] Saito, Y., and Rahman, M. K., 2007, "Investigation of Positive Electrodes After Cycle Testing of High-Power Li-Ion Battery Cells IV: An Approach to the Power Fading Mechanism by Depth Profile Analysis of Electrodes using Glow Discharge Optical Emission Spectroscopy," Journal of Power Sources, **174**(2) pp. 877-882.
- [97] Cho, J., and Park, B., 2001, "Preparation and electrochemical/thermal Properties of  $\text{LiNi}_{0.74}\text{Co}_{0.26}\text{O}_2$  Cathode Material," Journal of Power Sources, **92**(1-2) pp. 35-39.

[98] Cho, J., Kim, Y. J., and Park, B., 2001, "Structural Changes of  $\text{Li}_{3.1}\text{Mn}_{0.91}\text{Cr}_{1.09}\text{O}_4$  Cathode Material," *Solid State Ionics*, **138**(3-4) pp. 221-225.

[99] Delmas, C., Maccario, M., Croguennec, L., 2008, "Lithium Deintercalation in  $\text{LiFePO}_4$  Nanoparticles Via a Domino-Cascade Model," *Nature Materials*, **7**(8) pp. 665-671.

**APPENDICES**

Appendix A: Stress Data at Each Node in FEA Modeling and from Analytical Calculation

1. Nodal Element Numbering Chart:

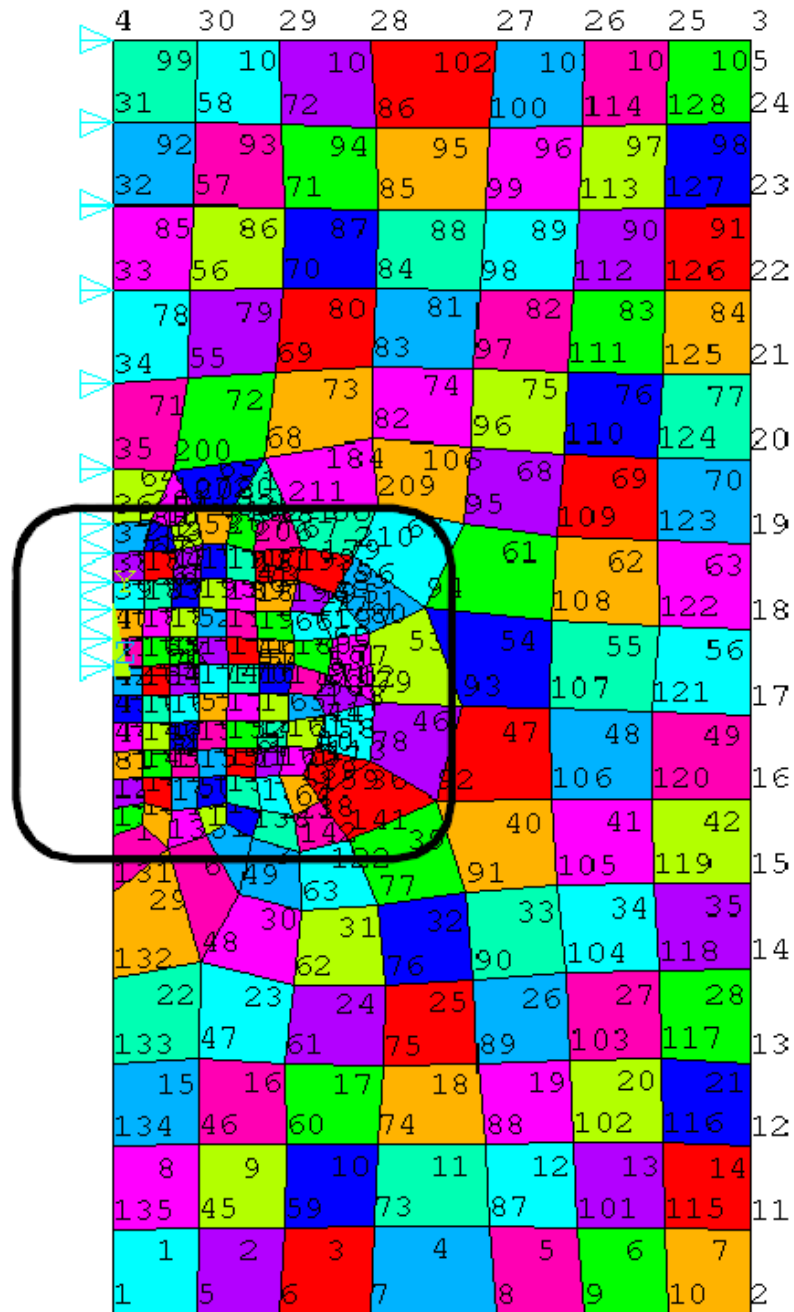
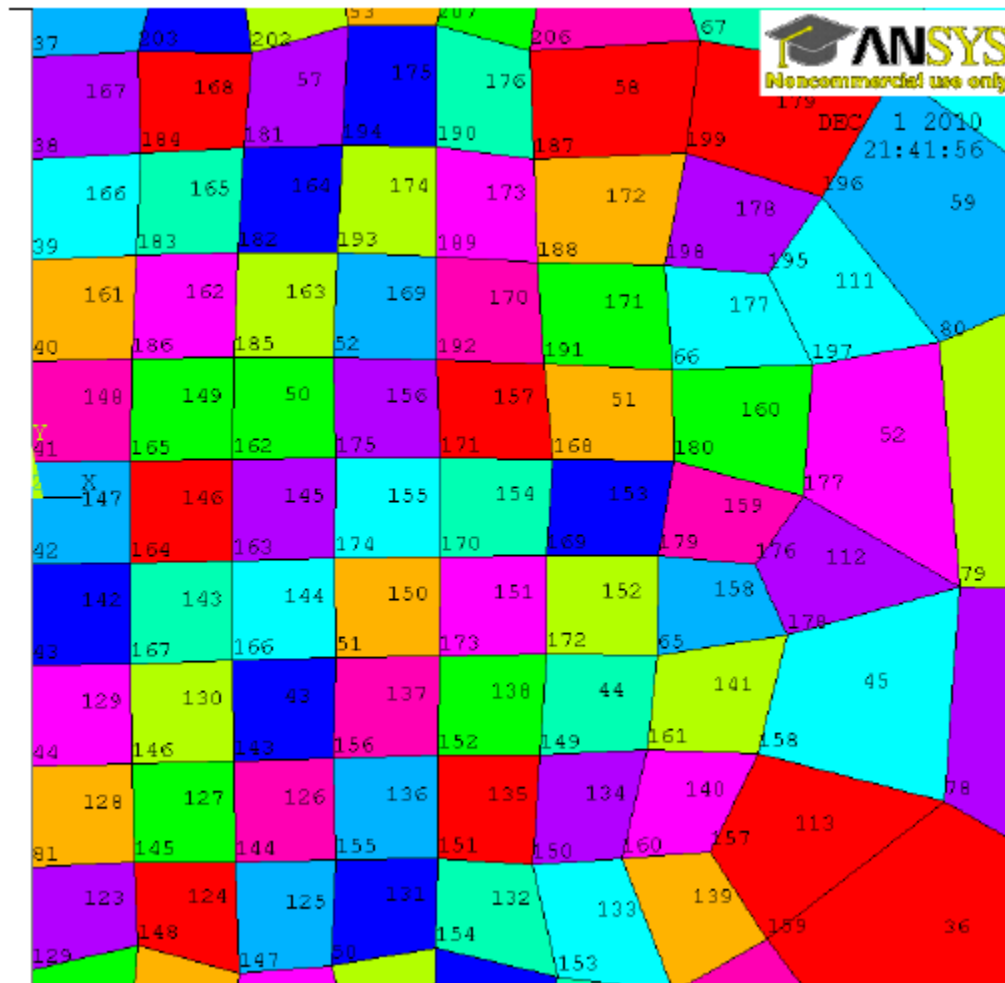


Figure A.1: Nodal numbering of the ANSYS model -- entire part



**Figure A.2:** Nodal numbering of the ANSYS model – the core area (circled area in figure (A.1))

## 2. Nodal Coordinates:

**Table A.1:** Coordinates of each node

NODE	X (m)	Y (m)	NODE	X (m)	Y (m)
1	0	-5.00E-08	4	0	5.00E-08
2	5.00E-08	-5.00E-08	5	6.50E-09	-5.00E-08
3	5.00E-08	5.00E-08	6	1.30E-08	-5.00E-08

Table A.1 Continued

NODE	X (m)	Y (m)	NODE	X (m)	Y (m)
7	2.00E-08	-5.00E-08	44	0	-5.90E-09
8	3.00E-08	-5.00E-08	45	6.67E-09	-4.34E-08
9	3.70E-08	-5.00E-08	46	6.72E-09	-3.68E-08
10	4.35E-08	-5.00E-08	47	6.74E-09	-3.00E-08
11	5.00E-08	-4.35E-08	48	6.79E-09	-2.24E-08
12	5.00E-08	-3.70E-08	49	9.91E-09	-1.71E-08
13	5.00E-08	-3.03E-08	50	6.56E-09	-1.03E-08
14	5.00E-08	-2.30E-08	51	6.67E-09	-3.53E-09
15	5.00E-08	-1.63E-08	52	6.62E-09	3.07E-09
16	5.00E-08	-9.66E-09	53	6.94E-09	1.03E-08
17	5.00E-08	-2.99E-09	54	4.57E-09	1.16E-08
18	5.00E-08	3.68E-09	55	5.84E-09	2.35E-08
19	5.00E-08	1.03E-08	56	5.93E-09	3.03E-08
20	5.00E-08	1.70E-08	57	6.28E-09	3.70E-08
21	5.00E-08	2.37E-08	58	6.48E-09	4.35E-08
22	5.00E-08	3.03E-08	59	1.35E-08	-4.34E-08
23	5.00E-08	3.70E-08	60	1.35E-08	-3.69E-08
24	5.00E-08	4.35E-08	61	1.34E-08	-3.04E-08
25	4.35E-08	5.00E-08	62	1.41E-08	-2.43E-08
26	3.70E-08	5.00E-08	63	1.47E-08	-1.85E-08
27	3.00E-08	5.00E-08	64	1.41E-08	-1.09E-08
28	2.00E-08	5.00E-08	65	1.37E-08	-3.45E-09
29	1.30E-08	5.00E-08	66	1.41E-08	2.79E-09
30	6.50E-09	5.00E-08	67	1.47E-08	1.00E-08
31	0	4.35E-08	68	1.18E-08	1.71E-08
32	0	3.70E-08	69	1.27E-08	2.38E-08
33	0	3.03E-08	70	1.32E-08	3.04E-08
34	0	2.30E-08	71	1.34E-08	3.68E-08
35	0	1.63E-08	72	1.32E-08	4.33E-08
36	0	1.19E-08	73	2.04E-08	-4.32E-08
37	0	9.66E-09	74	2.07E-08	-3.68E-08
38	0	7.44E-09	75	2.11E-08	-3.06E-08
39	0	5.21E-09	76	2.12E-08	-2.43E-08
40	0	2.99E-09	77	2.06E-08	-1.80E-08
41	0	7.70E-10	78	2.00E-08	-6.67E-09
42	0	-1.45E-09	79	2.04E-08	-1.96E-09
43	0	-3.68E-09	80	1.99E-08	3.40E-09

Table A.1 Continued

NODE	X (m)	Y (m)	NODE	X (m)	Y (m)
81	0	-8.12E-09	118	4.28E-08	-2.32E-08
82	2.03E-08	1.86E-08	119	4.24E-08	-1.63E-08
83	2.03E-08	2.43E-08	120	4.22E-08	-9.57E-09
84	2.06E-08	3.04E-08	121	4.23E-08	-2.80E-09
85	2.07E-08	3.67E-08	122	4.28E-08	4.00E-09
86	2.05E-08	4.31E-08	123	4.27E-08	1.06E-08
87	2.93E-08	-4.33E-08	124	4.27E-08	1.71E-08
88	2.91E-08	-3.67E-08	125	4.30E-08	2.37E-08
89	2.86E-08	-3.04E-08	126	4.32E-08	3.02E-08
90	2.82E-08	-2.38E-08	127	4.33E-08	3.68E-08
91	2.76E-08	-1.70E-08	128	4.34E-08	4.34E-08
92	2.54E-08	-9.71E-09	129	0	-1.03E-08
93	2.74E-08	-2.25E-09	130	0	-1.26E-08
94	2.44E-08	5.37E-09	131	0	-1.70E-08
95	2.75E-08	1.19E-08	132	0	-2.37E-08
96	2.81E-08	1.81E-08	133	0	-3.03E-08
97	2.82E-08	2.42E-08	134	0	-3.70E-08
98	2.87E-08	3.03E-08	135	0	-4.35E-08
99	2.92E-08	3.67E-08	136	4.25E-09	-1.34E-08
100	2.94E-08	4.31E-08	137	2.16E-09	-1.17E-08
101	3.65E-08	-4.33E-08	138	1.08E-08	-1.27E-08
102	3.61E-08	-3.67E-08	139	8.82E-09	-1.15E-08
103	3.59E-08	-3.00E-08	140	7.24E-09	-1.25E-08
104	3.55E-08	-2.33E-08	141	1.85E-08	-1.28E-08
105	3.48E-08	-1.64E-08	142	1.46E-08	-1.39E-08
106	3.43E-08	-9.52E-09	143	4.42E-09	-5.78E-09
107	3.42E-08	-2.48E-09	144	4.46E-09	-7.99E-09
108	3.43E-08	4.35E-09	145	2.24E-09	-7.99E-09
109	3.48E-08	1.09E-08	146	2.19E-09	-5.84E-09
110	3.54E-08	1.75E-08	147	4.55E-09	-1.04E-08
111	3.57E-08	2.39E-08	148	2.33E-09	-9.83E-09
112	3.61E-08	3.02E-08	149	1.12E-08	-5.65E-09
113	3.66E-08	3.67E-08	150	1.10E-08	-8.04E-09
114	3.68E-08	4.32E-08	151	8.91E-09	-7.90E-09
115	4.32E-08	-4.33E-08	152	8.92E-09	-5.64E-09
116	4.31E-08	-3.67E-08	153	1.16E-08	-1.05E-08
117	4.30E-08	-2.99E-08	154	8.87E-09	-9.88E-09

Table A.1 Continued

NODE	X (m)	Y (m)	NODE	X (m)	Y (m)
155	6.66E-09	-7.95E-09	189	8.89E-09	5.30E-09
156	6.62E-09	-5.74E-09	190	8.90E-09	7.70E-09
157	1.49E-08	-7.79E-09	191	1.12E-08	2.95E-09
158	1.59E-08	-5.62E-09	192	8.88E-09	3.02E-09
159	1.61E-08	-9.68E-09	193	6.71E-09	5.37E-09
160	1.30E-08	-7.90E-09	194	6.80E-09	7.73E-09
161	1.35E-08	-5.53E-09	195	1.62E-08	4.90E-09
162	4.40E-09	8.42E-10	189	8.89E-09	5.30E-09
163	4.40E-09	-1.38E-09	190	8.90E-09	7.70E-09
164	2.17E-09	-1.42E-09	191	1.12E-08	2.95E-09
165	2.17E-09	7.99E-10	192	8.88E-09	3.02E-09
166	4.40E-09	-3.58E-09	193	6.71E-09	5.37E-09
167	2.17E-09	-3.65E-09	194	6.80E-09	7.73E-09
168	1.14E-08	8.41E-10	195	1.62E-08	4.90E-09
169	1.13E-08	-1.26E-09	196	1.73E-08	6.59E-09
170	8.98E-09	-1.30E-09	197	1.71E-08	2.90E-09
171	8.98E-09	8.53E-10	198	1.39E-08	5.10E-09
172	1.13E-08	-3.42E-09	199	1.44E-08	7.56E-09
173	8.95E-09	-3.48E-09	200	4.70E-09	1.61E-08
174	6.64E-09	-1.34E-09	201	2.87E-09	1.23E-08
175	6.67E-09	8.54E-10	202	4.81E-09	9.75E-09
176	1.59E-08	-1.46E-09	203	2.32E-09	9.78E-09
177	1.69E-08	2.55E-11	204	1.12E-08	1.19E-08
178	1.66E-08	-3.02E-09	205	9.51E-09	1.32E-08
179	1.38E-08	-1.27E-09	206	1.09E-08	9.81E-09
180	1.41E-08	8.17E-10	207	8.88E-09	1.03E-08
181	4.64E-09	7.66E-09	208	6.42E-09	1.32E-08
182	4.50E-09	5.36E-09	209	2.07E-08	1.34E-08
183	2.30E-09	5.32E-09	210	1.90E-08	9.34E-09
184	2.37E-09	7.56E-09	211	1.37E-08	1.30E-08
185	4.43E-09	3.08E-09			
186	2.20E-09	3.06E-09			
187	1.10E-08	7.43E-09			
188	1.11E-08	5.16E-09			

### 3. Average Nodal Stresses Computed by ANSYS:

**Table A.2:** Average Nodal Stresses Computed by ANSYS

Node	Avg. Sxx	Avg. Syy	Avg. Sxy	Node	Avg. Sxx	Avg. Syy	Avg. Sxy
1	-5.5E+07	-9.4E+07	-56913	36	-1.8E+09	-1.1E+09	-1E+08
2	-7.5E+07	-7.5E+07	361960	37	-2E+09	-1.4E+09	-1.1E+08
3	-1.5E+09	-6.1E+08	115870	38	-2.2E+09	-1.6E+09	-2E+08
4	-1.5E+09	-5.9E+08	2358.7	39	-2.6E+09	-2.1E+09	-3E+08
5	-5.6E+07	-1.1E+08	-1.5E+07	40	-3.8E+09	-3.9E+09	-7.9E+08
6	-6.1E+07	-1.4E+08	-2.3E+07	41	-5.7E+09	9100000	1.98E+09
7	-6.8E+07	-1.8E+08	-1.8E+07	42	4.02E+09	-6.7E+08	1.97E+09
8	-7E+07	-2E+08	-173450	43	2.29E+09	3.24E+09	-8.4E+08
9	-6.8E+07	-1.9E+08	15596500	44	1.09E+09	1.47E+09	-3E+08
10	-5.6E+07	-1.4E+08	20270000	45	-7.2E+07	-9.1E+07	-2.1E+07
11	-1.1E+08	-7.1E+07	40365500	46	-8E+07	-7E+07	-3.1E+07
12	-1.4E+08	-9.5E+07	78980000	47	-6.8E+07	-3.7E+07	-4.9E+07
13	-1.9E+08	-1.2E+08	1.24E+08	48	4447740	17308980	-1E+08
14	-2.7E+08	-1.6E+08	1.76E+08	49	1.19E+08	-1E+08	-1.2E+08
15	-3.9E+08	-2.1E+08	2.24E+08	50	5.27E+08	-7.1E+07	-1.7E+08
16	-5.4E+08	-2.6E+08	2.63E+08	51	7.01E+08	-7.2E+08	8.6E+08
17	-7.2E+08	-3.2E+08	2.84E+08	52	-2.3E+09	35099000	7.83E+08
18	-9.1E+08	-3.8E+08	2.85E+08	53	-2E+09	-6.2E+08	-2E+08
19	-1.1E+09	-4.3E+08	2.59E+08	54	-1.9E+09	-9.1E+08	-1.5E+08
20	-1.2E+09	-4.9E+08	2.17E+08	55	-1.5E+09	-7.1E+08	-7.4E+07
21	-1.3E+09	-5.3E+08	1.68E+08	56	-1.5E+09	-6.4E+08	-4.5E+07
22	-1.4E+09	-5.7E+08	1.21E+08	57	-1.5E+09	-6E+08	-2.8E+07
23	-1.4E+09	-5.9E+08	76479500	58	-1.5E+09	-5.9E+08	-1.3E+07
24	-1.5E+09	-6E+08	36765500	59	-6.4E+07	-1.4E+08	-3.1E+07
25	-1.5E+09	-5.5E+08	1327450	60	-5.9E+07	-1.3E+08	-4.3E+07
26	-1.5E+09	-4.9E+08	1676050	61	-3.7E+07	-1.5E+08	-6E+07
27	-1.6E+09	-4.8E+08	1056850	62	5603150	-1.8E+08	-7.2E+07
28	-1.5E+09	-5E+08	-862645	63	73594250	-2.7E+08	-5.5E+07
29	-1.5E+09	-5.5E+08	-1718600	64	1.66E+08	-4.5E+08	1.26E+08
30	-1.5E+09	-5.8E+08	-1345800	65	-3E+08	-4.8E+08	6.41E+08
31	-1.5E+09	-6E+08	-6137850	66	-1.3E+09	-2.1E+08	6.22E+08
32	-1.5E+09	-6.2E+08	-1.3E+07	67	-1.7E+09	-2.2E+08	1.61E+08
33	-1.5E+09	-6.8E+08	-2.3E+07	68	-1.7E+09	-4.9E+08	-8.6E+07
34	-1.5E+09	-7.8E+08	-4.9E+07	69	-1.6E+09	-5.4E+08	-7.6E+07
35	-1.6E+09	-9.3E+08	-9E+07	70	-1.5E+09	-5.5E+08	-6E+07

Table A.2 Continued

71	-1.5E+09	-5.5E+08	-3.9E+07	108	-1E+09	-3.1E+08	2.93E+08
72	-1.5E+09	-5.5E+08	-2E+07	109	-1.2E+09	-3.1E+08	2.44E+08
73	-5.5E+07	-1.9E+08	-2.4E+07	110	-1.4E+09	-3.4E+08	1.75E+08
74	-4E+07	-2.1E+08	-2.7E+07	111	-1.5E+09	-3.8E+08	1.14E+08
75	-2.8E+07	-2.4E+08	-2.6E+07	112	-1.5E+09	-4.2E+08	72962500
76	-2E+07	-3E+08	-175768	113	-1.5E+09	-4.6E+08	42699250
77	-2.3E+07	-3.6E+08	61193500	114	-1.5E+09	-4.9E+08	19597525
78	-2.6E+08	-4.9E+08	3.91E+08	115	-7.4E+07	-1.4E+08	41573000
79	-6.7E+08	-3.7E+08	4.97E+08	116	-9.8E+07	-1.6E+08	69471000
80	-1.1E+09	-2.2E+08	4.55E+08	117	-1.4E+08	-2E+08	1.14E+08
81	6.55E+08	9.92E+08	-2E+08	118	-2.1E+08	-2.4E+08	1.7E+08
82	-1.6E+09	-3.3E+08	32262000	119	-3.3E+08	-2.9E+08	2.25E+08
83	-1.6E+09	-4E+08	-1.8E+07	120	-5E+08	-3.2E+08	2.74E+08
84	-1.6E+09	-4.5E+08	-3.1E+07	121	-7.1E+08	-3.3E+08	3E+08
85	-1.5E+09	-4.8E+08	-2.6E+07	122	-9.3E+08	-3.5E+08	3E+08
86	-1.5E+09	-5E+08	-1.4E+07	123	-1.1E+09	-3.7E+08	2.65E+08
87	-5E+07	-2.2E+08	1509075	124	-1.3E+09	-4.1E+08	2.14E+08
88	-4.2E+07	-2.5E+08	7598050	125	-1.4E+09	-4.5E+08	1.61E+08
89	-4.9E+07	-2.8E+08	26169500	126	-1.5E+09	-4.9E+08	1.12E+08
90	-7.6E+07	-3.4E+08	66113950	127	-1.5E+09	-5.2E+08	69262500
91	-1.4E+08	-3.9E+08	1.54E+08	128	-1.5E+09	-5.4E+08	33074000
92	-3E+08	-4.2E+08	2.68E+08	129	4.04E+08	7.23E+08	-1.2E+08
93	-6.9E+08	-3.6E+08	3.96E+08	130	2.74E+08	4.82E+08	-6.1E+07
94	-1.1E+09	-2.7E+08	3.33E+08	131	1.24E+08	2.44E+08	-1.1E+08
95	-1.3E+09	-2.8E+08	2.35E+08	132	-3.8E+07	1.09E+08	-7.6E+07
96	-1.5E+09	-3.1E+08	1.2E+08	133	-9E+07	13709000	-3.1E+07
97	-1.5E+09	-3.6E+08	56851675	134	-9.1E+07	-4.4E+07	-1.4E+07
98	-1.5E+09	-4.1E+08	22861375	135	-7.6E+07	-7.3E+07	-5252100
99	-1.5E+09	-4.4E+08	7844450	136	2.23E+08	2.05E+08	-1.6E+08
100	-1.6E+09	-4.7E+08	1856500	137	2.43E+08	5.01E+08	-7.2E+07
101	-5.7E+07	-2E+08	24646000	138	2.4E+08	-2.8E+08	-5.5E+07
102	-6.2E+07	-2.3E+08	41896000	139	3.4E+08	-2.1E+08	-7.4E+07
103	-8.8E+07	-2.7E+08	74185500	140	3.16E+08	-5.5E+07	-1.6E+08
104	-1.4E+08	-3.2E+08	1.24E+08	141	-2.2E+07	-4.2E+08	1.36E+08
105	-2.5E+08	-3.6E+08	1.9E+08	142	1.37E+08	-3.7E+08	10064325
106	-4.3E+08	-3.8E+08	2.59E+08	143	1.48E+09	-1.2E+08	-8.7E+07
107	-7E+08	-3.5E+08	3.08E+08	144	8.33E+08	2.05E+08	-2.8E+08

Table A.2 Continued

145	7.16E+08	7.37E+08	-2.2E+08	182	-3E+09	-5.8E+08	-1.3E+08
146	1.3E+09	9.7E+08	-4E+08	183	-2.8E+09	-1.6E+09	-4E+08
147	4.99E+08	2.52E+08	-2.5E+08	184	-2.3E+09	-1.4E+09	-2.3E+08
148	4.31E+08	5.8E+08	-1.7E+08	185	-3.4E+09	1.72E+08	4.97E+08
149	1.88E+08	-5.7E+08	4.96E+08	186	-4.7E+09	-1.1E+09	1.67E+08
150	3.22E+08	-5.2E+08	2.38E+08	187	-1.9E+09	-1.9E+08	2.28E+08
151	5.67E+08	-4.7E+08	1.36E+08	188	-1.8E+09	-1.2E+08	4.65E+08
152	5.19E+08	-6E+08	4.55E+08	189	-2.1E+09	-9.8E+07	3.95E+08
153	3.04E+08	-4.1E+08	66535250	190	-2.1E+09	-2.6E+08	69427425
154	4.64E+08	-3.1E+08	-2.2E+07	191	-1.5E+09	-1.5E+08	6.98E+08
155	7.93E+08	-2.4E+08	-7.1E+07	192	-1.8E+09	-7.2E+07	7.5E+08
156	9.99E+08	-5.8E+08	2.5E+08	193	-2.6E+09	-1.3E+08	1.92E+08
157	2385333	-5.4E+08	3.14E+08	194	-2.3E+09	-4.5E+08	-1E+08
158	-2E+08	-5E+08	4.76E+08	195	-1.4E+09	-1.6E+08	4.24E+08
159	-1.7E+07	-4.8E+08	2.26E+08	196	-1.4E+09	-1.8E+08	3.5E+08
160	1.31E+08	-5.3E+08	2.94E+08	197	-1.1E+09	-2.3E+08	5.47E+08
161	-3.9E+07	-5.3E+08	5.06E+08	198	-1.5E+09	-1.6E+08	4.59E+08
162	-2E+09	64133540	1.62E+09	199	-1.7E+09	-1.7E+08	2.95E+08
163	2.94E+08	-7.2E+08	1.67E+09	200	-1.7E+09	-8.1E+08	-1.3E+08
164	3.11E+09	-1.6E+09	1.48E+09	201	-1.8E+09	-1E+09	-1.3E+08
165	-4.8E+09	8.78E+08	1.4E+09	202	-2.1E+09	-9E+08	-2.2E+08
166	1.81E+09	-8.8E+08	5.82E+08	203	-2E+09	-1.2E+09	-1.7E+08
167	3.11E+09	4.58E+08	2.21E+08	204	-1.8E+09	-4E+08	1325667
168	-1.1E+09	-2.6E+08	8.41E+08	205	-1.9E+09	-5E+08	-1.3E+08
169	-5.7E+08	-4.1E+08	8.4E+08	206	-1.9E+09	-3E+08	56711000
170	-4.6E+08	-4.5E+08	1.03E+09	207	-2E+09	-4.3E+08	-9.7E+07
171	-1.2E+09	-2.2E+08	1.02E+09	208	-1.8E+09	-7.3E+08	-2E+08
172	-1.2E+08	-5.4E+08	7.23E+08	209	-1.5E+09	-2.7E+08	1.39E+08
173	1.72E+08	-6E+08	7.94E+08	210	-1.5E+09	-2.1E+08	2.39E+08
174	-2.3E+08	-5E+08	1.27E+09	211	-1.7E+09	-3.4E+08	32078525
175	-1.5E+09	-1.5E+08	1.25E+09				
176	-6.5E+08	-3.7E+08	5.64E+08				
177	-8.3E+08	-3.4E+08	5.93E+08				
178	-4.7E+08	-4.2E+08	5.73E+08				
179	-6.3E+08	-3.9E+08	6.94E+08				
180	-9.6E+08	-2.9E+08	7.01E+08				
181	-2.4E+09	-8.6E+08	-2.7E+08				

## 4. Nodal Stress Calculated by Classical Elastic Theory Equation:

**Table A.3:** Nodal Stress Calculated by Classical Elastic Theory Equation

Node	Sxx	Syy	Sxy	Node	Sxx	Syy	Sxy
1	2.1E+08	2.06E+08	0	36	-9E+08	-8.7E+08	0
2	2.1E+08	0	0	37	-1E+09	-1.1E+09	0
3	-2E+08	0	0	38	-1E+09	-1.4E+09	0
4	-2E+08	-2.1E+08	0	39	-2E+09	-2E+09	0
5	2.1E+08	1.96E+08	-2.5E+07	40	-3E+09	-3.4E+09	0
6	2.2E+08	1.69E+08	-4.4E+07	41	-1E+10	-1.3E+10	0
7	2.3E+08	1.28E+08	-5.1E+07	42	7.1E+09	7.09E+09	0
8	2.3E+08	71429832	-4.3E+07	43	2.8E+09	2.8E+09	0
9	2.3E+08	38916122	-2.9E+07	44	1.7E+09	1.75E+09	0
10	2.2E+08	16226142	-1.4E+07	45	2.4E+08	2.21E+08	-3.4E+07
11	2.2E+08	-1.4E+07	16226142	46	2.9E+08	2.53E+08	-4.6E+07
12	2.3E+08	-2.9E+07	38916122	47	3.6E+08	2.96E+08	-6.6E+07
13	2.2E+08	-4.2E+07	69523625	48	4.9E+08	3.5E+08	-1.1E+08
14	2.1E+08	-5.1E+07	1.11E+08	49	6.8E+08	2.24E+08	-1.3E+08
15	1.7E+08	-4.9E+07	1.5E+08	50	1.1E+09	3E+08	-1.9E+08
16	1.1E+08	-3.6E+07	1.84E+08	51	1.6E+09	-3.6E+08	6.8E+08
17	3.7E+07	-1.2E+07	2.04E+08	52	-2E+09	3.84E+08	8.27E+08
18	-5E+07	14900160	2.03E+08	53	-1E+09	-2.6E+08	-1.7E+08
19	-1E+08	37512993	1.81E+08	54	-1E+09	-5.6E+08	-2.2E+08
20	-2E+08	49785307	1.46E+08	55	-5E+08	-3.7E+08	-9.1E+07
21	-2E+08	50499438	1.07E+08	56	-4E+08	-3E+08	-5.9E+07
22	-2E+08	42189716	69523625	57	-3E+08	-2.6E+08	-4.3E+07
23	-2E+08	28797930	38916122	58	-2E+08	-2.2E+08	-3.3E+07
24	-2E+08	14116743	16226142	59	2.5E+08	1.79E+08	-5.5E+07
25	-2E+08	-1.6E+07	-1.4E+07	60	3E+08	1.88E+08	-6.9E+07
26	-2E+08	-3.9E+07	-2.9E+07	61	3.8E+08	1.92E+08	-8.4E+07
27	-2E+08	-7.1E+07	-4.3E+07	62	4.8E+08	1.57E+08	-9.1E+07
28	-2E+08	-1.3E+08	-5.1E+07	63	6.1E+08	77679815	-6.2E+07
29	-2E+08	-1.7E+08	-4.4E+07	64	8E+08	-9E+07	1.17E+08
30	-2E+08	-2E+08	-2.5E+07	65	5.1E+08	-1.6E+08	6.22E+08
31	-2E+08	-2.4E+08	0	66	-4E+08	1.29E+08	6.51E+08
32	-3E+08	-2.8E+08	0	67	-8E+08	1.19E+08	1.73E+08
33	-3E+08	-3.4E+08	0	68	-7E+08	-1.5E+08	-1E+08
34	-4E+08	-4.5E+08	0	69	-5E+08	-1.9E+08	-1E+08
35	-6E+08	-6.3E+08	0	70	-4E+08	-1.9E+08	-8.5E+07

Table A.3 Continued

71	-3E+08	-1.9E+08	-6.9E+07	108	-1E+08	36245900	2.86E+08
72	-3E+08	-1.8E+08	-5.5E+07	109	-2E+08	69298388	2.22E+08
73	2.7E+08	1.24E+08	-5.8E+07	110	-3E+08	70225209	1.42E+08
74	3.2E+08	1.1E+08	-6.2E+07	111	-3E+08	50821987	75911915
75	3.8E+08	80514000	-5.6E+07	112	-3E+08	24580080	29333085
76	4.5E+08	32237160	-2.8E+07	113	-3E+08	-541725	-539645
77	5.3E+08	-3.3E+07	37816084	114	-3E+08	-2.2E+07	-1.9E+07
78	4.3E+08	-1.2E+08	3.7E+08	115	2.4E+08	247732.4	-247218
79	1.4E+08	-4.7E+07	4.92E+08	116	2.5E+08	-1.9E+07	22141888
80	-3E+08	80723942	4.74E+08	117	2.6E+08	-3.9E+07	55961927
81	1.3E+09	1.27E+09	0	118	2.6E+08	-5.5E+07	1.02E+08
82	-5E+08	22172826	24211844	119	2.2E+08	-6E+07	1.57E+08
83	-5E+08	-4.4E+07	-3.7E+07	120	1.5E+08	-4.7E+07	2.09E+08
84	-4E+08	-8.6E+07	-5.8E+07	121	4.8E+07	-1.6E+07	2.4E+08
85	-3E+08	-1.1E+08	-6.2E+07	122	-7E+07	21938162	2.35E+08
86	-3E+08	-1.2E+08	-5.8E+07	123	-2E+08	49987555	2.01E+08
87	2.7E+08	60263034	-4.1E+07	124	-2E+08	60209211	1.5E+08
88	3.1E+08	39329124	-3.1E+07	125	-3E+08	54037724	98019693
89	3.5E+08	10917412	-1E+07	126	-3E+08	38328865	54745927
90	3.9E+08	-3E+07	35862194	127	-3E+08	18907903	22243141
91	4.1E+08	-7.5E+07	1.23E+08	128	-2E+08	-136781	-136623
92	3.7E+08	-1E+08	2.64E+08	129	1E+09	9.96E+08	0
93	9.1E+07	-3E+07	3.68E+08	130	8.2E+08	8.2E+08	0
94	-3E+08	80311513	3.65E+08	131	6.1E+08	6.06E+08	0
95	-4E+08	93591546	2.16E+08	132	4.4E+08	4.35E+08	0
96	-4E+08	69036454	1.07E+08	133	3.4E+08	3.4E+08	0
97	-4E+08	27259688	31737865	134	2.8E+08	2.78E+08	0
98	-3E+08	-1E+07	-9519559	135	2.4E+08	2.37E+08	0
99	-3E+08	-3.9E+07	-3.1E+07	136	8.2E+08	5.7E+08	-1.8E+08
100	-3E+08	-6E+07	-4.1E+07	137	9.1E+08	7.96E+08	-1.5E+08
101	2.5E+08	23714267	-2E+07	138	8.7E+08	72461424	-6.2E+07
102	2.8E+08	2166123	-2133460	139	9.8E+08	1.45E+08	-1.1E+08
103	3.1E+08	-2.5E+07	29622960	140	9.3E+08	3.06E+08	-1.8E+08
104	3.2E+08	-5.3E+07	80373073	141	6.1E+08	-9.2E+07	1.33E+08
105	3E+08	-7.3E+07	1.54E+08	142	7.2E+08	-1.8E+07	18909441
106	2.2E+08	-6.6E+07	2.39E+08	143	2E+09	2.94E+08	-2.2E+08
107	6.5E+07	-2.1E+07	2.96E+08	144	1.5E+09	5.16E+08	-2.9E+08

Table A.3 Continued

145	1.4E+09	1.02E+09	-2.9E+08	182	-2E+09	-1.9E+08	-1.6E+08
146	1.9E+09	1.16E+09	-4.4E+08	183	-2E+09	-1.1E+09	-4.8E+08
147	1.1E+09	5.65E+08	-2.5E+08	184	-1E+09	-1E+09	-3.2E+08
148	1.1E+09	8.86E+08	-2.1E+08	185	-3E+09	3.78E+08	5.43E+08
149	9.6E+08	-2.2E+08	4.35E+08	186	-4E+09	-7.1E+08	-5.1E+08
150	1E+09	-1.4E+08	1.85E+08	187	-1E+09	1.63E+08	2.41E+08
151	1.2E+09	-6.8E+07	77080582	188	-9E+08	2.29E+08	4.92E+08
152	1.3E+09	-2.2E+08	3.54E+08	189	-1E+09	2.42E+08	4.06E+08
153	9.3E+08	-4.1E+07	45318899	190	-1E+09	82492812	95363856
154	1.1E+09	61863740	-5.6E+07	191	-6E+08	1.96E+08	7.47E+08
155	1.4E+09	1.34E+08	-1.1E+08	192	-1E+09	2.8E+08	8.24E+08
156	1.6E+09	-1.1E+08	1.26E+08	193	-2E+09	1.64E+08	2.05E+08
157	7.3E+08	-1.6E+08	3.1E+08	194	-1E+09	-9.6E+07	-8.4E+07
158	5.6E+08	-1.6E+08	4.48E+08	195	-5E+08	1.47E+08	4.85E+08
159	7E+08	-1.3E+08	2.21E+08	196	-5E+08	1.47E+08	3.88E+08
160	8.7E+08	-1.6E+08	2.65E+08	197	-3E+08	93408986	5.52E+08
161	7.2E+08	-1.9E+08	4.66E+08	198	-7E+08	1.83E+08	4.98E+08
162	-1E+09	4.02E+08	2.1E+09	199	-8E+08	1.67E+08	3.18E+08
163	1.9E+09	-5.5E+08	1.75E+09	200	-7E+08	-5E+08	-1.4E+08
164	5.2E+09	-8.7E+08	1.32E+09	201	-9E+08	-7.1E+08	-1.7E+08
165	-4E+09	1.17E+09	3.18E+09	202	-1E+09	-5.2E+08	-2.6E+08
166	2.5E+09	-2.3E+08	2.88E+08	203	-1E+09	-8.9E+08	-2.1E+08
167	3.2E+09	9.98E+08	-5.9E+08	204	-9E+08	-2.8E+07	-2.6E+07
168	-2E+08	65322712	8.87E+08	205	-9E+08	-1.6E+08	-1.2E+08
169	3E+08	-9.8E+07	8.78E+08	206	-1E+09	51075227	56993234
170	4.8E+08	-1.6E+08	1.08E+09	207	-1E+09	-8.7E+07	-7.5E+07
171	-3E+08	1.06E+08	1.12E+09	208	-9E+08	-3.9E+08	-1.9E+08
172	7.2E+08	-2.1E+08	6.95E+08	209	-5E+08	93353603	1.45E+08
173	1.1E+09	-2.9E+08	7.38E+08	210	-6E+08	1.31E+08	2.66E+08
174	8.8E+08	-2.8E+08	1.37E+09	211	-8E+08	19855661	20936366
175	-6E+08	1.88E+08	1.47E+09				
176	1.8E+08	-5.8E+07	6.32E+08				
177	-3E+06	916246.7	6.08E+08				
178	3.2E+08	-1E+08	5.62E+08				
179	2E+08	-6.7E+07	7.3E+08				
180	-1E+08	41984725	7.24E+08				
181	-2E+09	-4.6E+08	-2.8E+08				

## Appendix B: Mathematica Code for Stress and Force Calculation Code

**1. Mathematica code for stress calculation with classical equation (equation 1) for single dislocation in isotropic material**

```
Eiso=10^9*(138.9^2+138.9*72.8-2*72.8^2)/(138.9+72.8)
8.88307×1010
```

```
viso=72.8/(138.9+72.8)
0.343883
```

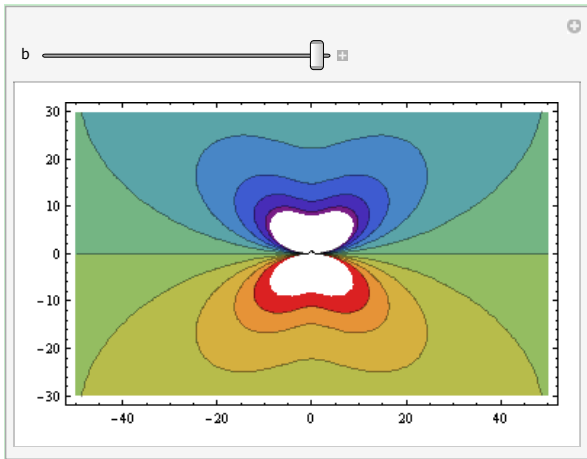
```
c11iso=(Eiso*(1-viso))/(1-viso-2*viso^2)
1.389×1011
```

```
c12iso=(Eiso*viso)/(1-viso-2*viso^2)
7.28×1010
```

```
c44iso=Eiso/(2+2viso)
3.305×1010
uiso=33.05*10^9
3.305×1010
```

```
Manipulate[ContourPlot[N[(-(uiso*b)/(2*Pi*(1-
viso)))*(y*(3*x^2+y^2))/(x^2+y^2)^2],{x,-50,50},{y,-
30,30},(*cotrol stress range*)PlotRange→{Full,All,{-
1000000000,1000000000}},ColorFunction→"Rainbow",AspectRatio→Au
tomatic,Contours→10,ContourLabels→Automatic,ClippingStyle→Non
e],{b,0,1,0.1}]
```

```
TraditionalForm[(-(uiso*b)/(2*Pi*(1-
viso)))*(y*(3*x^2+y^2))/(x^2+y^2)^2]
```

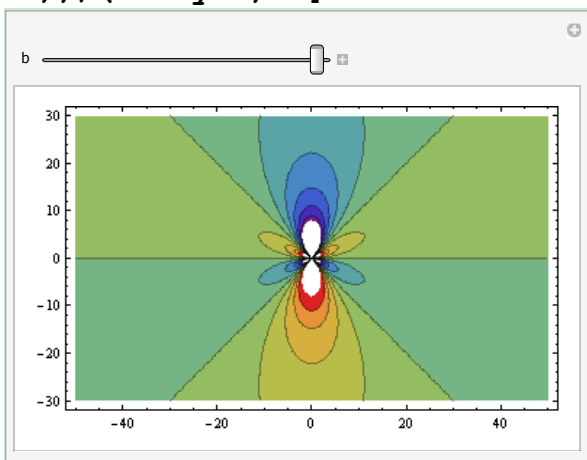


$$-((8.01697 \times 10^9 b y (3 x^2 + y^2)) / (x^2 + y^2)^2)$$

(\*The stress value at the tip of white area\*)

```
N[(-(uiso*b)/(2*Pi*(1-
viso)))*(y*(3*x^2+y^2))/(x^2+y^2)^2].{x->0,y->-8,b->1}
1.00212*10^9
```

```
Manipulate[ContourPlot[N[ ((uiso*b)/(2*Pi*(1-viso)))*(y*(x^2-
y^2))/(x^2+y^2)^2],{x,-50,50},{y,-30,30},(*cotrol stress
range*)PlotRange->{Full,All,{-
1000000000,1000000000}},ColorFunction->"Rainbow",AspectRatio->Au
tomatic,Contours->10,ContourLabels->False,ClippingStyle->None],{
b,0,1,0.1}]
TraditionalForm[ ((uiso*b)/(2*Pi*(1-viso)))*(y*(x^2-
y^2))/(x^2+y^2)^2]
```

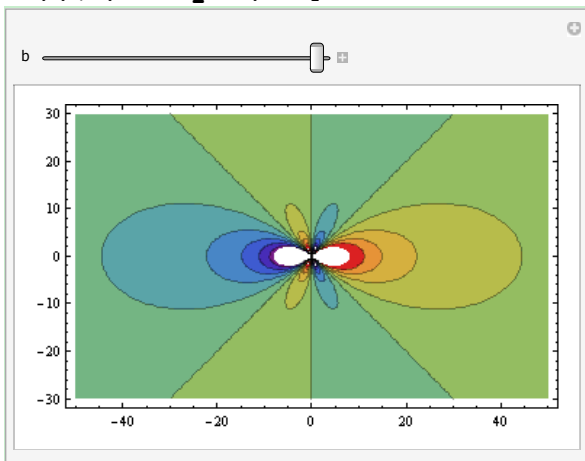


$$(8.01697 \times 10^9 b y (x^2 - y^2)) / (x^2 + y^2)^2$$

(\*The stress value at the tip of white area\*)

```
N[ ((uiso*b) / (2*Pi*(1-viso))) * (y*(x^2-
y^2)) / (x^2+y^2)^2] /. {x→0,y→-8,b→1}
1.00212×109
```

```
Manipulate[ContourPlot[N[ ((uiso*b) / (2*Pi*(1-viso))) * (x*(x^2-
y^2)) / (x^2+y^2)^2], {x,-50,50}, {y,-30,30}, (*cotrol stress
range*)PlotRange→{Full,All,{-
1000000000,1000000000}}, ColorFunction→"Rainbow", AspectRatio→Au
tomatic, Contours→10, ContourLabels→False, ClippingStyle→None], {
b,0,1,0.1}]
TraditionalForm[ ((uiso*b) / (2*Pi*(1-viso))) * (x*(x^2-
y^2)) / (x^2+y^2)^2]
```

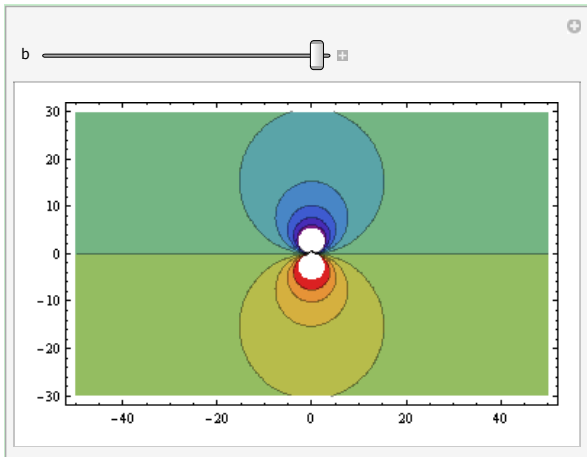


$(8.01697 \times 10^9 b x (x^2 - y^2)) / (x^2 + y^2)^2$

(\*The stress value at the tip of white area\*)

```
N[ ((uiso*b) / (2*Pi*(1-viso))) * (x*(x^2-
y^2)) / (x^2+y^2)^2] /. {x→8,y→0,b→1}
1.00212×109
```

```
Manipulate[ContourPlot[N[viso*((( -(uiso*b) / (2*Pi*(1-
viso))) * (y*(3*x^2+y^2)) / (x^2+y^2)^2) + (((uiso*b) / (2*Pi*(1-
viso))) * (y*(x^2-y^2)) / (x^2+y^2)^2))], {x,-50,50}, {y,-
30,30}, (*cotrol stress range*)PlotRange→{Full,All,{-
1000000000,1000000000}}, ColorFunction→"Rainbow", AspectRatio→Au
tomatic, Contours→10, ContourLabels→False, ClippingStyle→None], {
b,0,1,0.1}]
TraditionalForm[viso*((( -(uiso*b) / (2*Pi*(1-
viso))) * (y*(3*x^2+y^2)) / (x^2+y^2)^2) + (((uiso*b) / (2*Pi*(1-
viso))) * (y*(x^2-y^2)) / (x^2+y^2)^2))]
```

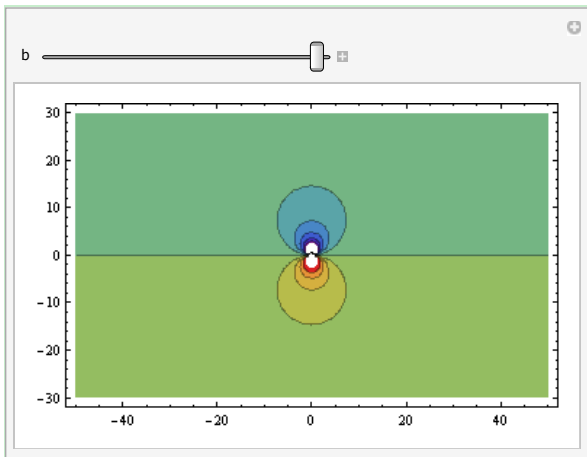


$$0.343883 \left( (8.01697 \times 10^9 b y (x^2 - y^2)) / (x^2 + y^2)^2 - (8.01697 \times 10^9 b y (3 x^2 + y^2)) / (x^2 + y^2)^2 \right)$$

(\*The stress value at the tip of white area\*)

```
N[viso*(((-(uiso*b)/(2*Pi*(1-
viso)))*(y*(3*x^2+y^2))/(x^2+y^2)^2)+((uiso*b)/(2*Pi*(1-
viso)))*(y*(x^2-y^2))/(x^2+y^2)^2)]/.{x->0,y->-6,b->1}
9.18966*10^8
```

```
Manipulate[ContourPlot[N[(-
uiso*b)/(2*Pi)]*(y)/(x^2+y^2)],{x,-50,50},{y,-30,30},(*cotrol
stress range*)PlotRange->{Full,All,{-
1000000000,1000000000}},ColorFunction->"Rainbow",AspectRatio->Au
tomatic,Contours->10,ContourLabels->False,ClippingStyle->None],{
b,0,0.5,0.1}]
TraditionalForm[(-(uiso*b)/(2*Pi)]*(y)/(x^2+y^2)]
```



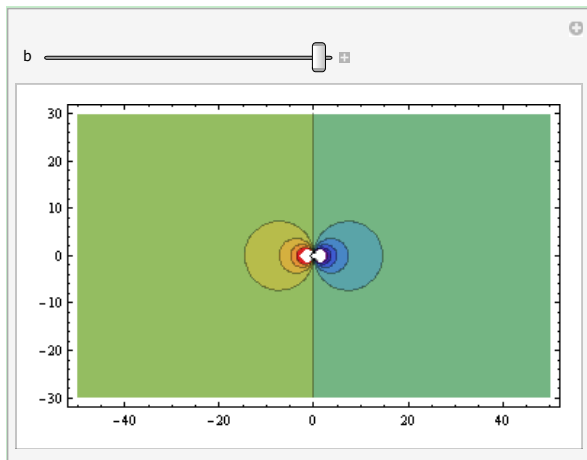
$$-((5.26007 \times 10^9 b y) / (x^2 + y^2))$$

(\*The stress value at the tip of white area\*)

```
N[(-uiso*b)/(2*Pi)*y/(x^2+y^2)]/.{x→0,y→-5,b→1}
1.05201×109
```

```
Manipulate[ContourPlot[N[(-uiso*b)/(2*Pi)*x/(x^2+y^2)],{x,-50,50},{y,-30,30},(*cotrol
stress range*)PlotRange→{Full,All,{-1000000000,1000000000}},ColorFunction→"Rainbow",AspectRatio→Au
tomatic,Contours→10,ContourLabels→False,ClippingStyle→None],{
b,0,0.5,0.1}]
```

```
TraditionalForm[(-uiso*b)/(2*Pi)*x/(x^2+y^2)]
```



```
-((5.26007×109 b x)/(x2+y2))
```

(\*The stress value at the tip of white area\*)

```
N[(-uiso*b)/(2*Pi)*x/(x^2+y^2)]/.{x→-4,y→0,b→1}
1.31502×109
```

**2. Mathematica code for stress calculation with generalized equation (equation 2) for single dislocation in isotropic material**

```

c11=138.9*10^9
c22=138.9*10^9
c33=138.9*10^9
c44=33.05*10^9
c55=33.05*10^9
c66=33.05*10^9
c12=72.8*10^9
c13=72.8*10^9
c23=72.8*10^9
1.389×1011
1.389×1011
1.389×1011
3.305×1010
3.305×1010
3.305×1010
7.28×1010
7.28×1010
7.28×1010

cd11=Sqrt[c11*c22]
1.389×1011

λ=Sqrt[Sqrt[c11/c22]]
1.

φ=1/2*ArcCos[(c12*c12+2*c12*c66-cd11*cd11)/(2*cd11*c66)]
1.5708_-1.05367×10-8 i

Q[x_,y_] := x*x+2*x*y*λ*Cos[φ]+y*y*λ*λ
T[x_,y_] := x*x-2*x*y*λ*Cos[φ]+y*y*λ*λ

σ11[x_,y_] := ((bx*λ*(c12-
cd11))/(4*Pi*Q[x,y]*T[x,y]*cd11*c66*Sin[φ]))*(c11*((cd11+c12+c
66)*x*x*y+λ*λ*c66*y*y*y) -
(c12/c22)*((c12*c12+cd11*c12+2*c12*c66+cd11*c66)*x*x*y-
cd11*c66*λ*λ*y*y*y)) - ((by*λ*(c12-
cd11))/(4*Pi*Q[x,y]*T[x,y]*cd11*c66*Sin[φ]))*(c12*((cd11+c12+c
66)*λ*λ*x*y*y+c66*x*x*x) -

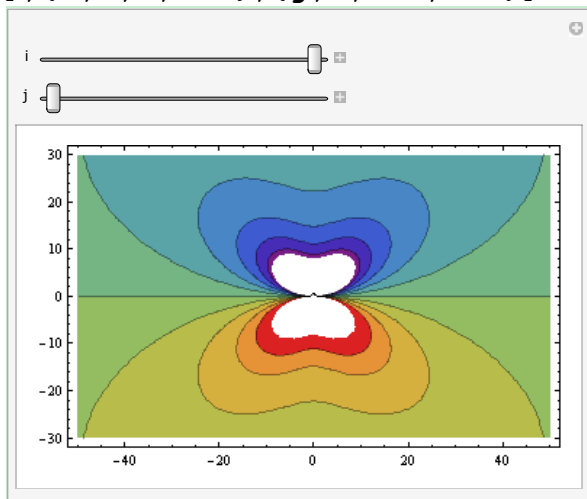
```

```
(c11/c22) * ((c12*c12+cd11*c12+2*c12*c66+cd11*c66) *λ*λ*x*y*y-
cd11*c66*x*x*x)
```

```
TraditionalForm[σ11[x,y]]
```

```
((1.14582×10-12+7.39271×10-37 i) by (7.28×1010 (3.305×1010 x3+2.4475×1011 x y2)-1.
(2.48145×1022 x y2-4.59064×1021 x3))/((x2-(1.22465×10-16+2.10734×10-8 i) x y+1. y2)
(x2+(1.22465×10-16+2.10734×10-8 i) x y+1. y2))-((1.14582×10-12+7.39271×10-37 i) bx
(1.389×1011 (2.4475×1011 x2 y+3.305×1010 y3)-0.524118 (2.48145×1022 x2 y-4.59064×1021
y3))/((x2-(1.22465×10-16+2.10734×10-8 i) x y+1. y2) (x2+(1.22465×10-16+2.10734×10-8 i) x
y+1. y2))
```

```
Manipulate[ContourPlot[{σ11[x,y]}/.{bx→i, by→j},{x,-
50,50},{y,-30,30},(*cotrol stress
range*)PlotRange→{Full,All},{-
1000000000,1000000000}],ColorFunction→"Rainbow",AspectRatio→Au
tomatic,Contours→10,ContourLabels→Automatic,ClippingStyle→Non
e],{i,0,1,0.1},{j,0,0.6,0.1}]
```



(\*The stress value at the tip of white area\*)

```
σ11[x,y]/.{x→0,y→-8,bx→1,by→0}
```

```
1.00212×109+6.46556×10-16 i
```

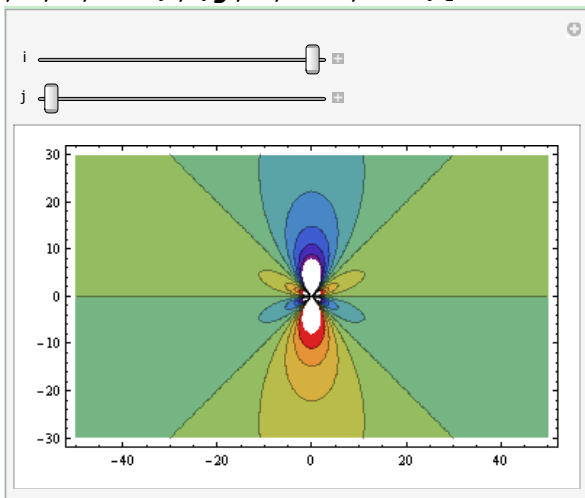
```
σ22[x_,y_] := ((bx*λ*(c12-
cd11))/(4*Pi*Q[x,y]*T[x,y]*cd11*c66*Sin[φ]))*(c12*((cd11+c12+c
66)*x*x*y+λ*λ*c66*y*y*y)-
(c22/c22)*((c12*c12+cd11*c12+2*c12*c66+cd11*c66)*x*x*y-
cd11*c66*λ*λ*y*y*y))-((by*λ*(c12-
cd11))/(4*Pi*Q[x,y]*T[x,y]*cd11*c66*Sin[φ]))*(c22*((cd11+c12+c
66)*λ*λ*x*y+y*c66*x*x*x)-
```

```
(c12/c22) * ((c12*c12+cd11*c12+2*c12*c66+cd11*c66) *λ*λ*x*y*y-
cd11*c66*x*x*x)
```

```
TraditionalForm[σ22[x,y]]
```

```
((1.14582×10-12+7.39271×10-37 i) by (1.389×1011 (3.305×1010 x3+2.4475×1011 x y2)-
0.524118 (2.48145×1022 x y2-4.59064×1021 x3))/((x2-(1.22465×10-16+2.10734×10-8 i) x y+1.
y2) (x2+(1.22465×10-16+2.10734×10-8 i) x y+1. y2))-((1.14582×10-12+7.39271×10-37 i) bx
(7.28×1010 (2.4475×1011 x2 y+3.305×1010 y3)-1. (2.48145×1022 x2 y-4.59064×1021 y3))/((x2-
(1.22465×10-16+2.10734×10-8 i) x y+1. y2) (x2+(1.22465×10-16+2.10734×10-8 i) x y+1. y2))
```

```
Manipulate[ContourPlot[{σ22[x,y]}/.{bx→i, by→j},{x,-
50,50},{y,-30,30},(*cotrol stress
range*)PlotRange→{Full,All,{-
1000000000,1000000000}}],ColorFunction→"Rainbow",AspectRatio→Au
tomatic,Contours→10,ContourLabels→False,ClippingStyle→None],{
i,0,1,0.1},{j,0,0.6,0.1}]
```



(\*The stress value at the tip of white area\*)

```
σ22[x,y]/.{x→0,y→-8,bx→1,by→0}
1.00212×109+6.46556×10-16 i
```

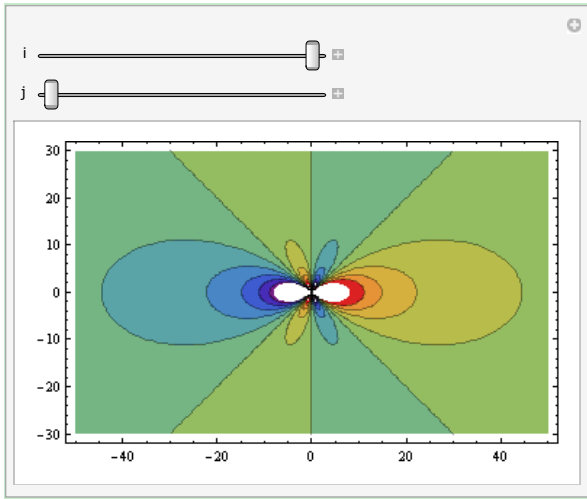
```
σ12[x_,y_] := ((bx*λ*(c12-
cd11))/(4*Pi*Q[x,y]*T[x,y]*cd11*c66*Sin[φ]))*(-
c66*(c12+cd11)*(x*x*x-λ*λ*x*y*y))-((by*λ*(c12-
cd11))/(4*Pi*Q[x,y]*T[x,y]*cd11*c66*Sin[φ]))*(-
c66*(c12+cd11)*(λ*λ*y*y*y-x*x*y))
```

```
TraditionalForm[σ12[x,y]]
```

```
((8.01697×109+5.17245×10-15 i) bx (x3-1. x y2))/((x2-(1.22465×10-16+2.10734×10-8 i) x y+1.
y2) (x2+(1.22465×10-16+2.10734×10-8 i) x y+1. y2))-((8.01697×109+5.17245×10-15 i) by (1.
y3-x2 y))/((x2-(1.22465×10-16+2.10734×10-8 i) x y+1. y2) (x2+(1.22465×10-16+2.10734×10-8 i)
```

$x y + 1. y^2)$

```
Manipulate[ContourPlot[ $\sigma_{12}[x,y]$ ]/. {bx->i, by->j}, {x,-50,50}, {y,-30,30}, (*control stress range*) PlotRange->{Full, All, {-1000000000, 1000000000}}, ColorFunction->"Rainbow", AspectRatio->Automatic, Contours->10, ContourLabels->Automatic, ClippingStyle->None], {i, 0, 1, 0.1}, {j, 0, 0.6, 0.1}]
```



(\*The stress value at the tip of white area\*)

```
 $\sigma_{12}[x,y]$  /. {x->8, y->0, bx->1, by->0}
```

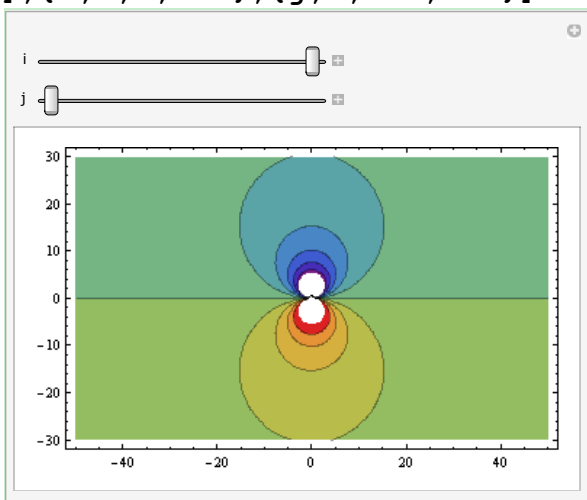
$1.00212 \times 10^9 + 6.46556 \times 10^{-16} i$

```
 $\sigma_{33}[x_, y_] := 0.343883 * ((bx * \lambda * (c12 - cd11)) / (4 * \text{Pi} * Q[x, y] * T[x, y] * cd11 * c66 * \text{Sin}[\phi])) * (c11 * ((cd11 + c12 + c66) * x * x * y + \lambda * \lambda * c66 * y * y * y) - (c12 / c22) * ((c12 * c12 + cd11 * c12 + 2 * c12 * c66 + cd11 * c66) * x * x * y - cd11 * c66 * \lambda * \lambda * y * y * y)) + ((-by * \lambda * (c12 - cd11)) / (4 * \text{Pi} * Q[x, y] * T[x, y] * cd11 * c66 * \text{Sin}[\phi])) * (c12 * ((cd11 + c12 + c66) * \lambda * \lambda * x * y * y + c66 * x * x * x) - (c11 / c22) * ((c12 * c12 + cd11 * c12 + 2 * c12 * c66 + cd11 * c66) * \lambda * \lambda * x * y * y - cd11 * c66 * x * x * x)) + (bx * \lambda * (c12 - cd11)) / (4 * \text{Pi} * Q[x, y] * T[x, y] * cd11 * c66 * \text{Sin}[\phi])) * (c12 * ((cd11 + c12 + c66) * x * x * y + \lambda * \lambda * c66 * y * y * y) - (c22 / c22) * ((c12 * c12 + cd11 * c12 + 2 * c12 * c66 + cd11 * c66) * x * x * y - cd11 * c66 * \lambda * \lambda * y * y * y)) + ((-by * \lambda * (c12 - cd11)) / (4 * \text{Pi} * Q[x, y] * T[x, y] * cd11 * c66 * \text{Sin}[\phi])) * (c22 * ((cd11 + c12 + c66) * \lambda * \lambda * x * y * y + c66 * x * x * x) - (c12 / c22) * ((c12 * c12 + cd11 * c12 + 2 * c12 * c66 + cd11 * c66) * \lambda * \lambda * x * y * y - cd11 * c66 * x * x * x))$ 
```

**TraditionalForm[σ33[x,y]]**

$$0.343883 \left( -\left( (1.14582 \times 10^{-12} + 7.39271 \times 10^{-37} i) b_x (7.28 \times 10^{10} (2.4475 \times 10^{11} x^2 y + 3.305 \times 10^{10} y^3) - 1. (2.48145 \times 10^{22} x^2 y - 4.59064 \times 10^{21} y^3)) \right) / \left( (x^2 - (1.22465 \times 10^{-16} + 2.10734 \times 10^{-8} i) x y + 1. y^2) \right) - \left( (1.14582 \times 10^{-12} + 7.39271 \times 10^{-37} i) b_x (1.389 \times 10^{11} (2.4475 \times 10^{11} x^2 y + 3.305 \times 10^{10} y^3) - 0.524118 (2.48145 \times 10^{22} x^2 y - 4.59064 \times 10^{21} y^3)) \right) / \left( (x^2 - (1.22465 \times 10^{-16} + 2.10734 \times 10^{-8} i) x y + 1. y^2) (x^2 + (1.22465 \times 10^{-16} + 2.10734 \times 10^{-8} i) x y + 1. y^2) \right) + \left( (1.14582 \times 10^{-12} + 7.39271 \times 10^{-37} i) b_y (7.28 \times 10^{10} (3.305 \times 10^{10} x^3 + 2.4475 \times 10^{11} x y^2) - 1. (2.48145 \times 10^{22} x y^2 - 4.59064 \times 10^{21} x^3)) \right) / \left( (x^2 - (1.22465 \times 10^{-16} + 2.10734 \times 10^{-8} i) x y + 1. y^2) (x^2 + (1.22465 \times 10^{-16} + 2.10734 \times 10^{-8} i) x y + 1. y^2) \right) + \left( (1.14582 \times 10^{-12} + 7.39271 \times 10^{-37} i) b_y (1.389 \times 10^{11} (3.305 \times 10^{10} x^3 + 2.4475 \times 10^{11} x y^2) - 0.524118 (2.48145 \times 10^{22} x y^2 - 4.59064 \times 10^{21} x^3)) \right) / \left( (x^2 - (1.22465 \times 10^{-16} + 2.10734 \times 10^{-8} i) x y + 1. y^2) (x^2 + (1.22465 \times 10^{-16} + 2.10734 \times 10^{-8} i) x y + 1. y^2) \right) \right)$$

**Manipulate[ContourPlot[{σ33[x,y]}/.{bx→i, by→j},{x,-50,50},{y,-30,30},(\*cotrol stress range\*)PlotRange→{Full,All,{-1000000000,1000000000}},ColorFunction→"Rainbow",AspectRatio→Automatic,Contours→10,ContourLabels→Automatic,ClippingStyle→None],{i,0,1,0.1},{j,0,0.6,0.1}]**

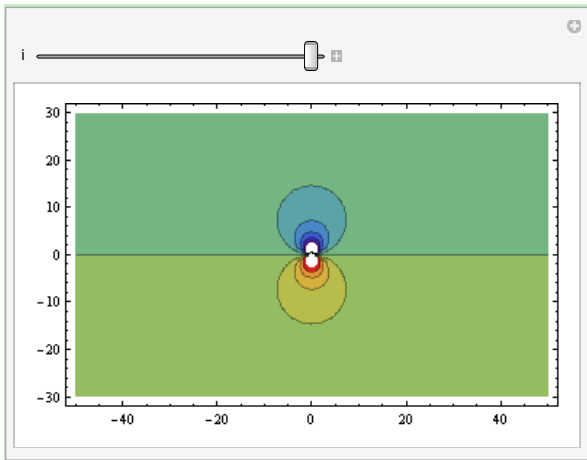


(\*The stress value at the tip of white area\*)

$\sigma_{33}[x,y] /. \{x \rightarrow 0, y \rightarrow -6, b_x \rightarrow 1, b_y \rightarrow 0\}$   
 $9.18966 \times 10^8 + 5.92906 \times 10^{-16} i$

$\tau_{xz}[x_,y_] := (b_z / (2 * \text{Pi})) * \text{Sqrt}[c_{44} * c_{55}] * ((-c_{55} * y) / (c_{44} * x * x + c_{55} * y * y))$   
**TraditionalForm[τxz[x,y]]**  
 $-((1.73845 \times 10^{20} b_z y) / (3.305 \times 10^{10} x^2 + 3.305 \times 10^{10} y^2))$

```
Manipulate[ContourPlot[{\tau_{xz}[x,y]}/.{bz->i},{x,-50,50},{y,-30,30},(*control stress range*)PlotRange->{Full,All,{-1000000000,1000000000}},ColorFunction->"Rainbow",AspectRatio->Automatic,Contours->10,ContourLabels->Automatic,ClippingStyle->None],{i,0,0.5,0.1}]
```

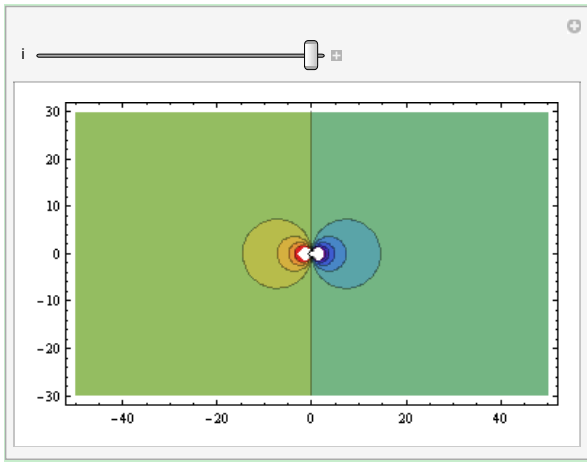


(\*The stress value at the tip of white area\*)

```
\tau_{xz}[x,y]/.{bz->1,x->0,y->-5}
1.05201\times 10^9
```

```
\tau_{yz}[x_,y_] := (-
bz/(2*Pi))*Sqrt[(c44*c55)]*((c44*x)/(c44*x*x+c55*y*y))
TraditionalForm[\tau_{yz}[x,y]]
-((1.73845\times 10^{20} bz x)/(3.305\times 10^{10} x^2+3.305\times 10^{10} y^2))
```

```
Manipulate[ContourPlot[{\tau_{yz}[x,y]}/.{bz->i},{x,-50,50},{y,-30,30},(*control stress range*)PlotRange->{Full,All,{-1000000000,1000000000}},ColorFunction->"Rainbow",AspectRatio->Automatic,Contours->10,ContourLabels->Automatic,ClippingStyle->None],{i,0,0.5,0.1}]
```



(\*The stress value at the tip of white area\*)

$\tau_{yz}[\mathbf{x}, \mathbf{y}] /. \{bz \rightarrow 1, x \rightarrow -5, y \rightarrow 0\}$

$1.05201 \times 10^9$

### 3. Mathematica code for stress calculation with generalized equation (equation 2) for single dislocation in anisotropic material

```
c11=138.9*10^9
```

```
c22=198.0*10^9
```

```
c33=173.0*10^9
```

```
c44=36.8*10^9
```

```
c55=50.6*10^9
```

```
c66=47.6*10^9
```

```
c12=72.8*10^9
```

```
c13=52.5*10^9
```

```
c23=45.8*10^9
```

```
1.389*1011
```

```
1.98*1011
```

```
1.73*1011
```

```
3.68*1010
```

```
5.06*1010
```

```
4.76*1010
```

```
7.28*1010
```

```
5.25*1010
```

```
4.58*1010
```

```
cd11=Sqrt[c11*c22]
```

```
1.65838*1011
```

```
λ=Sqrt[Sqrt[c11/c22]]
```

```
0.915186
```

```
φ=1/2*ArcCos[(c12*c12+2*c12*c66-cd11*cd11)/(2*cd11*c66)]
```

```
1.44261
```

```
Q[x_,y_]:=x*x+2*x*y*λ*Cos[φ]+y*y*λ*λ
```

```
T[x_,y_]:=x*x-2*x*y*λ*Cos[φ]+y*y*λ*λ
```

```
σ11[x_,y_]:=((bx*λ*(c12-
```

```
cd11))/(4*Pi*Q[x,y]*T[x,y]*cd11*c66*Sin[φ]))*(c11*((cd11+c12+c  
66)*x*x*y+λ*λ*c66*y*y*y)-
```

```
(c12/c22)*((c12*c12+cd11*c12+2*c12*c66+cd11*c66)*x*x*y-
```

```
cd11*c66*λ*λ*y*y*y))+((
```

```
-by*λ*(c12-
```

```
cd11))/(4*Pi*Q[x,y]*T[x,y]*cd11*c66*Sin[φ]))*(c12*((cd11+c12+c  
66)*λ*λ*x*y*y+c66*x*x*x)-
```

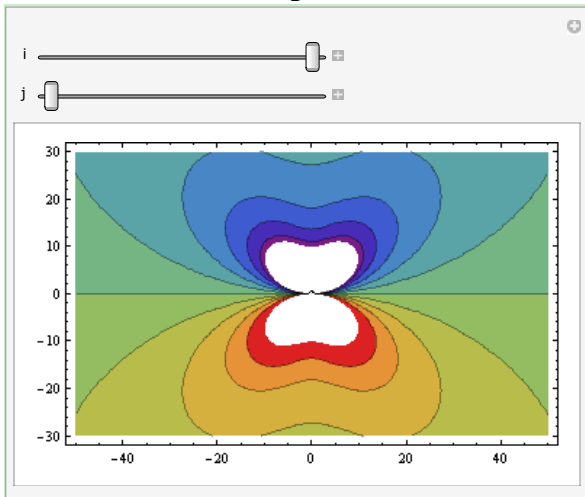
```
(c11/c22)*((c12*c12+cd11*c12+2*c12*c66+cd11*c66)*λ*λ*x*y*y-
```

`cd11*c66*x*x*x)`

`TraditionalForm[σ11[x,y]]`

$$\frac{(8.65458 \times 10^{-13} b_y (7.28 \times 10^{10} (4.76 \times 10^{10} x^3 + 2.39743 \times 10^{11} x y^2) - 0.701515 (2.69673 \times 10^{22} x y^2 - 7.89388 \times 10^{21} x^3))) / ((x^2 - 0.233978 x y + 0.837565 y^2) (x^2 + 0.233978 x y + 0.837565 y^2)) - (8.65458 \times 10^{-13} b_x (1.389 \times 10^{11} (2.86238 \times 10^{11} x^2 y + 3.98681 \times 10^{10} y^3) - 0.367677 (3.21973 \times 10^{22} x^2 y - 6.61164 \times 10^{21} y^3))) / ((x^2 - 0.233978 x y + 0.837565 y^2) (x^2 + 0.233978 x y + 0.837565 y^2))}{1}$$

`Manipulate[ContourPlot[{σ11[x,y]}/.{bx→i, by→j},{x,-50,50},{y,-30,30},(*cotrol stress range*)PlotRange→{Full,All},{-1000000000,1000000000}],ColorFunction→"Rainbow",AspectRatio→Automatic,Contours→10,ContourLabels→Automatic,ClippingStyle→None],{i,0,1,0.1},{j,0,0.6,0.1}]`



(\*The stress value at the tip of white area\*)

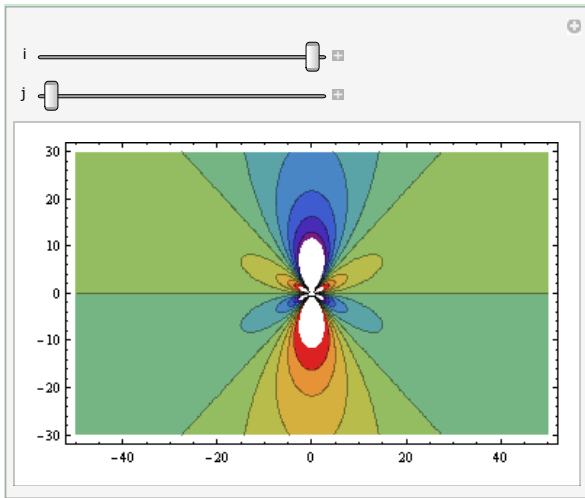
`σ11[x,y]/.{x→0,y→-10,bx→1,by→0}`  
 $9.83088 \times 10^8$

$$\sigma_{22}[x_, y_] := ((bx*\lambda*(c12 - cd11)) / (4*Pi*Q[x, y]*T[x, y]*cd11*c66*\text{Sin}[\phi])) * (c12 * ((cd11 + c12 + c66) * x*x*y + \lambda*\lambda*c66*y*y*y) - (c22/c22) * ((c12*c12 + cd11*c12 + 2*c12*c66 + cd11*c66) * x*x*y - cd11*c66*\lambda*\lambda*y*y*y)) + ((-by*\lambda*(c12 - cd11)) / (4*Pi*Q[x, y]*T[x, y]*cd11*c66*\text{Sin}[\phi])) * (c22 * ((cd11 + c12 + c66) * \lambda*\lambda*x*y*y + c66*x*x*x) - (c12/c22) * ((c12*c12 + cd11*c12 + 2*c12*c66 + cd11*c66) * \lambda*\lambda*x*y*y - cd11*c66*x*x*x))$$

**TraditionalForm[σ22[x,y]**

$$(8.65458 \times 10^{-13} b_y (1.98 \times 10^{11} (4.76 \times 10^{10} x^3 + 2.39743 \times 10^{11} x y^2) - 0.367677 (2.69673 \times 10^{22} x y^2 - 7.89388 \times 10^{21} x^3))) / ((x^2 - 0.233978 x y + 0.837565 y^2) (x^2 + 0.233978 x y + 0.837565 y^2)) - (8.65458 \times 10^{-13} b_x (7.28 \times 10^{10} (2.86238 \times 10^{11} x^2 y + 3.98681 \times 10^{10} y^3) - 1. (3.21973 \times 10^{22} x^2 y - 6.61164 \times 10^{21} y^3))) / ((x^2 - 0.233978 x y + 0.837565 y^2) (x^2 + 0.233978 x y + 0.837565 y^2))$$

**Manipulate[ContourPlot[{σ22[x,y]}/.{bx→i, by→j},{x,-50,50},{y,-30,30},(\*cotrol stress range\*)PlotRange→{Full,All,{-1000000000,1000000000}},ColorFunction→"Rainbow",AspectRatio→Automatic,Contours→10,ContourLabels→Automatic,ClippingStyle→None],{i,0,1,0.1},{j,0,0.6,0.1}]**



(\*The stress value at the tip of white area\*)

$\sigma_{22}[x,y] /. \{x \rightarrow 0, y \rightarrow -12, bx \rightarrow 1, by \rightarrow 0\}$

$9.78121 \times 10^8$

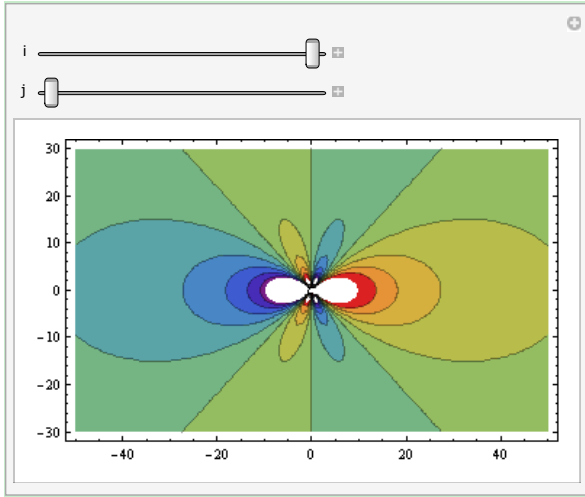
$$\sigma_{12}[x_, y_] := ((bx * \lambda * (c_{12} - cd_{11})) / (4 * \pi * Q[x, y] * T[x, y] * cd_{11} * c_{66} * \sin[\phi])) * (-c_{66} * (c_{12} + cd_{11}) * (x * x * x - \lambda * \lambda * x * y * y)) + ((-by * \lambda * (c_{12} - cd_{11})) / (4 * \pi * Q[x, y] * T[x, y] * cd_{11} * c_{66} * \sin[\phi])) * (-c_{66} * (c_{12} + cd_{11}) * (\lambda * \lambda * y * y * y - x * x * y))$$

**TraditionalForm[σ12[x,y]**

$$(9.83088 \times 10^9 b_x (x^3 - 0.837565 x y^2)) / ((x^2 - 0.233978 x y + 0.837565 y^2) (x^2 + 0.233978 x y + 0.837565 y^2)) - (9.83088 \times 10^9 b_y (0.837565 y^3 - x^2 y)) / ((x^2 - 0.233978 x y + 0.837565 y^2) (x^2 + 0.233978 x y + 0.837565 y^2))$$

**Manipulate[ContourPlot[{σ12[x,y]}/.{bx→i, by→j},{x,-**

```
50,50},{y,-30,30},(*cotrol stress
range*)PlotRange→{Full,All,{-
1000000000,1000000000}},ColorFunction→"Rainbow",AspectRatio→Au
tomatic,Contours→10,ContourLabels→Automatic,ClippingStyle→Non
e},{i,0,1,0.1},{j,0,0.6,0.1}]
```



(\*The stress value at the tip of white area\*)

```
 $\sigma_{12}[x,y] /. \{x \rightarrow 10, y \rightarrow 0, bx \rightarrow 1, by \rightarrow 0\}$   

9.83088  $\times 10^8$ 
```

```
 $\sigma_{33}[x_, y_] := 0.34 * ((bx * \lambda * (c12 -$   

 $cd11)) / (4 * \text{Pi} * Q[x, y] * T[x, y] * cd11 * c66 * \text{Sin}[\phi])) * (c11 * ((cd11 + c12 + c$   

 $66) * x * x * y + \lambda * \lambda * c66 * y * y * y) -$   

 $(c12 / c22) * ((c12 * c12 + cd11 * c12 + 2 * c12 * c66 + cd11 * c66) * x * x * y -$   

 $cd11 * c66 * \lambda * \lambda * y * y * y)) + (($   

 $-by * \lambda * (c12 -$   

 $cd11)) / (4 * \text{Pi} * Q[x, y] * T[x, y] * cd11 * c66 * \text{Sin}[\phi])) * (c12 * ((cd11 + c12 + c$   

 $66) * \lambda * \lambda * x * y * y + c66 * x * x * x) -$   

 $(c11 / c22) * ((c12 * c12 + cd11 * c12 + 2 * c12 * c66 + cd11 * c66) * \lambda * \lambda * x * y * y -$   

 $cd11 * c66 * x * x * x)) + (bx * \lambda * (c12 -$   

 $cd11)) / (4 * \text{Pi} * Q[x, y] * T[x, y] * cd11 * c66 * \text{Sin}[\phi])) * (c12 * ((cd11 + c12 + c$   

 $66) * x * x * y + \lambda * \lambda * c66 * y * y * y) -$   

 $(c22 / c22) * ((c12 * c12 + cd11 * c12 + 2 * c12 * c66 + cd11 * c66) * x * x * y -$   

 $cd11 * c66 * \lambda * \lambda * y * y * y)) + ((-by * \lambda * (c12 -$   

 $cd11)) / (4 * \text{Pi} * Q[x, y] * T[x, y] * cd11 * c66 * \text{Sin}[\phi])) * (c22 * ((cd11 + c12 + c$   

 $66) * \lambda * \lambda * x * y * y + c66 * x * x * x) -$   

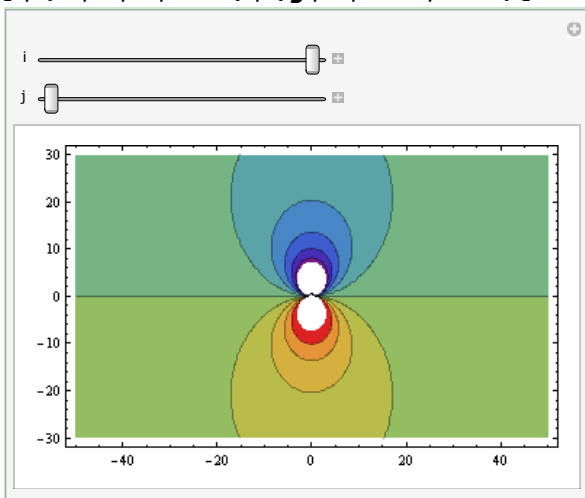
 $(c12 / c22) * ((c12 * c12 + cd11 * c12 + 2 * c12 * c66 + cd11 * c66) * \lambda * \lambda * x * y * y -$   

 $cd11 * c66 * x * x * x))$ 
```

```
TraditionalForm[ $\sigma_{33}[x, y]$ ]
```

$$0.34 \left( - \left( (8.65458 \times 10^{-13} b_x (7.28 \times 10^{10} (2.86238 \times 10^{11} x^2 y + 3.98681 \times 10^{10} y^3) - 1. (3.21973 \times 10^{22} x^2 y - 6.61164 \times 10^{21} y^3))) / ((x^2 - 0.233978 x y + 0.837565 y^2) (x^2 + 0.233978 x y + 0.837565 y^2)) \right) - \right. \\ \left. (8.65458 \times 10^{-13} b_x (1.389 \times 10^{11} (2.86238 \times 10^{11} x^2 y + 3.98681 \times 10^{10} y^3) - 0.367677 (3.21973 \times 10^{22} x^2 y - 6.61164 \times 10^{21} y^3))) / ((x^2 - 0.233978 x y + 0.837565 y^2) (x^2 + 0.233978 x y + 0.837565 y^2)) \right) + \\ \left. (8.65458 \times 10^{-13} b_y (7.28 \times 10^{10} (4.76 \times 10^{10} x^3 + 2.39743 \times 10^{11} x y^2) - 0.701515 (2.69673 \times 10^{22} x y^2 - 7.89388 \times 10^{21} x^3))) / ((x^2 - 0.233978 x y + 0.837565 y^2) (x^2 + 0.233978 x y + 0.837565 y^2)) \right) + \\ \left. (8.65458 \times 10^{-13} b_y (1.98 \times 10^{11} (4.76 \times 10^{10} x^3 + 2.39743 \times 10^{11} x y^2) - 0.367677 (2.69673 \times 10^{22} x y^2 - 7.89388 \times 10^{21} x^3))) / ((x^2 - 0.233978 x y + 0.837565 y^2) (x^2 + 0.233978 x y + 0.837565 y^2)) \right)$$

```
Manipulate[ContourPlot[{σ33[x,y]}/.{bx→i, by→j},{x,-50,50},{y,-30,30},(*cotrol stress range*)PlotRange→{Full,All,{-1000000000,1000000000}},ColorFunction→"Rainbow",AspectRatio→Automatic,Contours→10,ContourLabels→Automatic,ClippingStyle→None],{i,0,1,0.1},{j,0,0.6,0.1}]
```



(\*The stress value at the tip of white area\*)

$$\sigma_{33}[x,y] /. \{x \rightarrow 0, y \rightarrow -7, bx \rightarrow 1, by \rightarrow 0\}$$

$$1.0476 \times 10^9$$

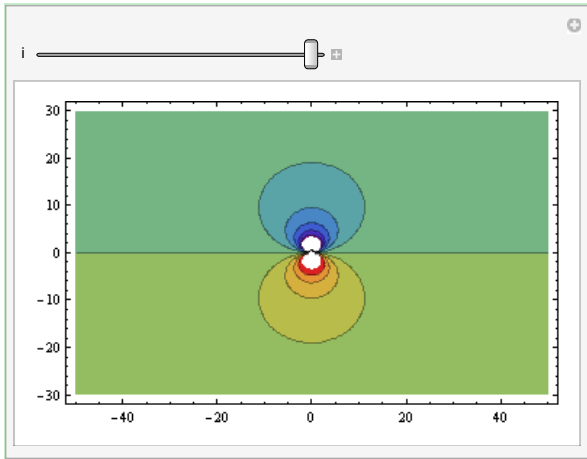
$$\tau_{xz}[x,y] := (bz / (2 * \text{Pi})) * \text{Sqrt}[(c44 * c55)] * ((-c55 * y) / (c44 * x * x + c55 * y * y))$$

$$\text{TraditionalForm}[\tau_{xz}[x,y]]$$

$$-(3.47512 \times 10^{20} b_z y) / (3.68 \times 10^{10} x^2 + 5.06 \times 10^{10} y^2)$$

```
Manipulate[ContourPlot[{τxz[x,y]}/.{bz→i},{x,-50,50},{y,-30,30},(*cotrol stress range*)PlotRange→{Full,All,{-1000000000,1000000000}},ColorFunction→"Rainbow",AspectRatio→Au
```

```
Automatic,Contours→10,ContourLabels→Automatic,ClippingStyle→None],{i,0,0.5,0.1}]
```



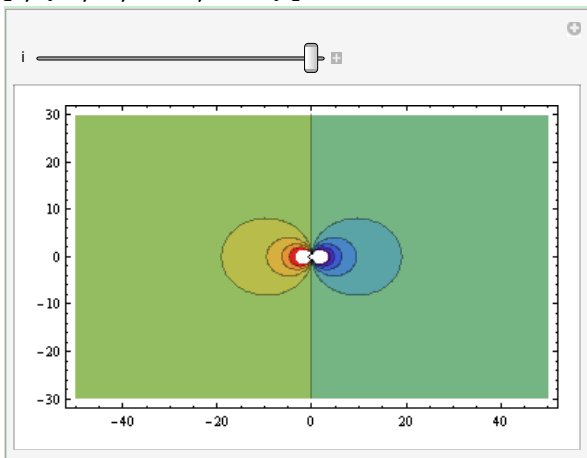
(\*The stress value at the tip of white area\*)

```
 $\tau_{xz}[x,y] /. \{bz \rightarrow 1, x \rightarrow 0, y \rightarrow -6\}$   
1.14464  $\times 10^9$ 
```

```
 $\tau_{yz}[x_,y_] := (-$   
 $bz / (2 * \text{Pi})) * \text{Sqrt}[(c44 * c55)] * ((c44 * x) / (c44 * x * x + c55 * y * y))$ 
```

```
TraditionalForm[ $\tau_{yz}[x,y]$ ]  
 $-((2.52736 \times 10^{20} \text{bz } x) / (3.68 \times 10^{10} x^2 + 5.06 \times 10^{10} y^2))$ 
```

```
Manipulate[ContourPlot[ $\{\tau_{yz}[x,y]\} /. \{bz \rightarrow i\}, \{x, -50, 50\}, \{y, -30, 30\},$   
(*control stress range*)PlotRange→{Full,All,{-1000000000,1000000000}},ColorFunction→"Rainbow",AspectRatio→Automatic,  
Contours→10,ContourLabels→Automatic,ClippingStyle→None],{i,0,0.5,0.1}]
```



(\*The stress value at the tip of white area\*)

$$\tau_{yz}[\mathbf{x}, \mathbf{y}] /. \{\mathbf{bz} \rightarrow 1, \mathbf{x} \rightarrow -7, \mathbf{y} \rightarrow 0\}$$

$$9.81118 \times 10^8$$

**4. Mathematica code for stress calculation with generalized equation (equation 2) for multiple dislocation in anisotropic material**

```

Eiso=10^9*(138.9^2+138.9*72.8-2*72.8^2)/(138.9+72.8)
viso=72.8/(138.9+72.8)
c11iso=(Eiso*(1-viso))/(1-viso-2*viso^2)
c12iso=(Eiso*viso)/(1-viso-2*viso^2)
c44iso=Eiso/(2+2viso)
uiso=33.05*10^9
8.88307×1010
0.343883
1.389×1011
7.28×1010
3.305×1010
3.305×1010

c11=138.9*10^9
c22=198.0*10^9
c33=173.0*10^9
c44=36.8*10^9
c55=50.6*10^9
c66=47.6*10^9
c12=72.8*10^9
c13=52.5*10^9
c23=45.8*10^9
1.389×1011
1.98×1011
1.73×1011
3.68×1010
5.06×1010
4.76×1010
7.28×1010
5.25×1010
4.58×1010

cd11=Sqrt[c11*c22]
1.65838×1011

λ=Sqrt[Sqrt[c11/c22]]
0.915186

φ=1/2*ArcCos[(c12*c12+2*c12*c66-cd11*cd11)/(2*cd11*c66)]

```

1.44261

$$Q1[x_, y_] := (x-m1) * (x-m1) + 2 * (x-m1) * (y-n1) * \lambda * \text{Cos}[\phi] + (y-n1) * (y-n1) * \lambda * \lambda$$

$$T1[x_, y_] := (x-m1) * (x-m1) - 2 * (x-m1) * (y-n1) * \lambda * \text{Cos}[\phi] + (y-n1) * (y-n1) * \lambda * \lambda$$

$$Q2[x_, y_] := (x-m2) * (x-m2) + 2 * (x-m2) * (y-n2) * \lambda * \text{Cos}[\phi] + (y-n2) * (y-n2) * \lambda * \lambda$$

$$T2[x_, y_] := (x-m2) * (x-m2) - 2 * (x-m2) * (y-n2) * \lambda * \text{Cos}[\phi] + (y-n2) * (y-n2) * \lambda * \lambda$$

(\*New equation--Two Edge--Any Burgers vector directoin & any location\*)

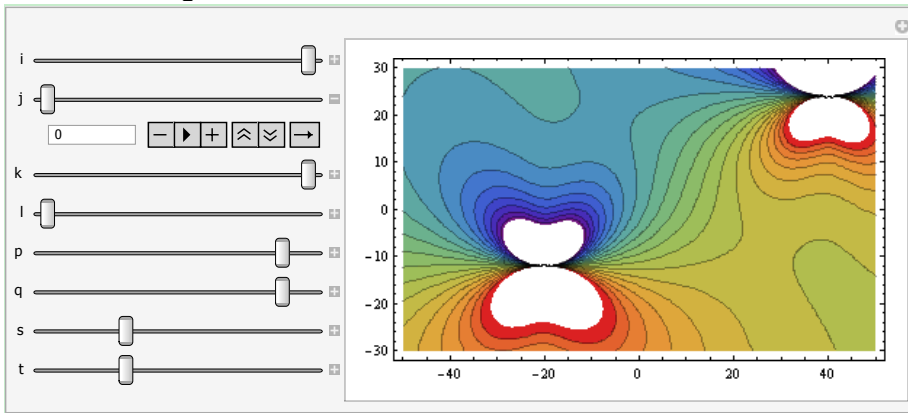
$$\begin{aligned} \sigma_{11}[x_, y_] := & ((b1x * \lambda * (c12 - cd11)) / (4 * \text{Pi} * Q1[x, y] * T1[x, y] * cd11 * c66 * \text{Sin}[\phi])) * (c11 * ((cd11 + c12 + c66) * (x-m1)^2 * (y-n1) + \lambda * \lambda * c66 * (y-n1)^3) - \\ & (c12/c22) * ((c12 * c12 + cd11 * c12 + 2 * c12 * c66 + cd11 * c66) * (x-m1)^2 * (y-n1) - cd11 * c66 * \lambda * \lambda * (y-n1)^3)) + ( \\ & -b1y * \lambda * (c12 - cd11)) / (4 * \text{Pi} * Q1[x, y] * T1[x, y] * cd11 * c66 * \text{Sin}[\phi])) * (c12 * ((cd11 + c12 + c66) * \lambda * \lambda * (x-m1) * (y-n1)^2 + c66 * (x-m1)^3) - \\ & (c11/c22) * ((c12 * c12 + cd11 * c12 + 2 * c12 * c66 + cd11 * c66) * \lambda * \lambda * (x-m1) * (y-n1)^2 - cd11 * c66 * (x-m1)^3)) + ((b2x * \lambda * (c12 - cd11)) / (4 * \text{Pi} * Q2[x, y] * T2[x, y] * cd11 * c66 * \text{Sin}[\phi])) * (c11 * ((cd11 + c12 + c66) * (x-m2)^2 * (y-n2) + \lambda * \lambda * c66 * (y-n2)^3) - \\ & (c12/c22) * ((c12 * c12 + cd11 * c12 + 2 * c12 * c66 + cd11 * c66) * (x-m2)^2 * (y-n2) - cd11 * c66 * \lambda * \lambda * (y-n2)^3)) + ( \\ & -b2y * \lambda * (c12 - cd11)) / (4 * \text{Pi} * Q2[x, y] * T2[x, y] * cd11 * c66 * \text{Sin}[\phi])) * (c12 * ((cd11 + c12 + c66) * \lambda * \lambda * (x-m2) * (y-n2)^2 + c66 * (x-m2)^3) - \\ & (c11/c22) * ((c12 * c12 + cd11 * c12 + 2 * c12 * c66 + cd11 * c66) * \lambda * \lambda * (x-m2) * (y-n2)^2 - cd11 * c66 * (x-m2)^3)) \end{aligned}$$

**TraditionalForm**[ $\sigma_{11}[x, y]$ ]

$$\begin{aligned} & -((8.65458 \times 10^{-13} b1x (1.389 \times 10^{11} (2.86238 \times 10^{11} (x-m1)^2 (y-n1) + 3.98681 \times 10^{10} (y-n1)^3) - \\ & 0.367677 (3.21973 \times 10^{22} (x-m1)^2 (y-n1) - 6.61164 \times 10^{21} (y-n1)^3)) / ((-0.233978 (x-m1) (y-n1) + (x-m1)^2 + 0.837565 (y-n1)^2)) + \\ & (8.65458 \times 10^{-13} b1y (7.28 \times 10^{10} (2.39743 \times 10^{11} (x-m1) (y-n1)^2 + 4.76 \times 10^{10} (x-m1)^3) - \\ & 0.701515 (2.69673 \times 10^{22} (x-m1) (y-n1)^2 - 7.89388 \times 10^{21} (x-m1)^3)) / ((-0.233978 (x-m1) (y-n1) + (x-m1)^2 + 0.837565 (y-n1)^2)) - \end{aligned}$$

$$\begin{aligned} & (8.65458 \times 10^{-13} b_2 x (1.389 \times 10^{11} (2.86238 \times 10^{11} (x-m_2)^2 (y-n_2) + 3.98681 \times 10^{10} (y-n_2)^3) - \\ & 0.367677 (3.21973 \times 10^{22} (x-m_2)^2 (y-n_2) - 6.61164 \times 10^{21} (y-n_2)^3)) / ((-0.233978 (x-m_2) (y- \\ & n_2) + (x-m_2)^2 + 0.837565 (y-n_2)^2) (0.233978 (x-m_2) (y-n_2) + (x-m_2)^2 + 0.837565 (y- \\ & n_2)^2)) + (8.65458 \times 10^{-13} b_2 y (7.28 \times 10^{10} (2.39743 \times 10^{11} (x-m_2) (y-n_2)^2 + 4.76 \times 10^{10} (x-m_2)^3) - \\ & 0.701515 (2.69673 \times 10^{22} (x-m_2) (y-n_2)^2 - 7.89388 \times 10^{21} (x-m_2)^3)) / ((-0.233978 (x-m_2) (y- \\ & n_2) + (x-m_2)^2 + 0.837565 (y-n_2)^2) (0.233978 (x-m_2) (y-n_2) + (x-m_2)^2 + 0.837565 (y-n_2)^2)) \end{aligned}$$

```
Manipulate[ContourPlot[{\sigma11[x,y]}/. {b1x->i,
b1y->j,b2x->k,b2y->l,m1->p, n1->q,m2->s,n2->t}, {x,-50,50}, {y,-
30,30}, (*cotrol stress range*)PlotRange->{Full,All,{-
1000000000,1000000000}}, ColorFunction->"Rainbow", AspectRatio->Au
tomatic, Contours->20, ContourLabels->Automatic, ClippingStyle->Non
e], {i,0,1,0.1}, {j,0,0.6,0.1}, {k,0,1,0.1}, {l,0,0.6,0.1}, {p,-
50,50,1}, {q,-30,30,1}, {s,-50,50,1}, {t,-30,30,1}]
```



$$\begin{aligned} \sigma_{22}[x_, y_] := & ((b_1 x * \lambda * (c_{12} - \\ & c_{d11})) / (4 * \text{Pi} * Q_1[x, y] * T_1[x, y] * c_{d11} * c_{66} * \text{Sin}[\phi])) * (c_{12} * ((c_{d11} + c_{12} \\ & + c_{66}) * (x - m_1)^2 * (y - n_1) + \lambda * \lambda * c_{66} * (y - n_1)^3) - \\ & (c_{22} / c_{22}) * ((c_{12} * c_{12} + c_{d11} * c_{12} + 2 * c_{12} * c_{66} + c_{d11} * c_{66}) * (x - m_1)^2 * (y - \\ & n_1) - c_{d11} * c_{66} * \lambda * \lambda * (y - n_1)^3)) + ((-b_1 y * \lambda * (c_{12} - \\ & c_{d11})) / (4 * \text{Pi} * Q_1[x, y] * T_1[x, y] * c_{d11} * c_{66} * \text{Sin}[\phi])) * (c_{22} * ((c_{d11} + c_{12} \\ & + c_{66}) * \lambda * \lambda * (x - m_1) * (y - n_1)^2 + c_{66} * (x - m_1)^3) - \\ & (c_{12} / c_{22}) * ((c_{12} * c_{12} + c_{d11} * c_{12} + 2 * c_{12} * c_{66} + c_{d11} * c_{66}) * \lambda * \lambda * (x - \\ & m_1) * (y - n_1)^2 - c_{d11} * c_{66} * (x - m_1)^3)) + ((b_2 x * \lambda * (c_{12} - \\ & c_{d11})) / (4 * \text{Pi} * Q_2[x, y] * T_2[x, y] * c_{d11} * c_{66} * \text{Sin}[\phi])) * (c_{12} * ((c_{d11} + c_{12} \\ & + c_{66}) * (x - m_2)^2 * (y - n_2) + \lambda * \lambda * c_{66} * (y - n_2)^3) - \\ & (c_{22} / c_{22}) * ((c_{12} * c_{12} + c_{d11} * c_{12} + 2 * c_{12} * c_{66} + c_{d11} * c_{66}) * (x - m_2)^2 * (y - \\ & n_2) - c_{d11} * c_{66} * \lambda * \lambda * (y - n_2)^3)) + ((-b_2 y * \lambda * (c_{12} - \\ & c_{d11})) / (4 * \text{Pi} * Q_2[x, y] * T_2[x, y] * c_{d11} * c_{66} * \text{Sin}[\phi])) * (c_{22} * ((c_{d11} + c_{12} \\ & + c_{66}) * \lambda * \lambda * (x - m_2) * (y - n_2)^2 + c_{66} * (x - m_2)^3) - \\ & (c_{12} / c_{22}) * ((c_{12} * c_{12} + c_{d11} * c_{12} + 2 * c_{12} * c_{66} + c_{d11} * c_{66}) * \lambda * \lambda * (x - \\ & m_2) * (y - n_2)^2 - c_{d11} * c_{66} * (x - m_2)^3)) \end{aligned}$$

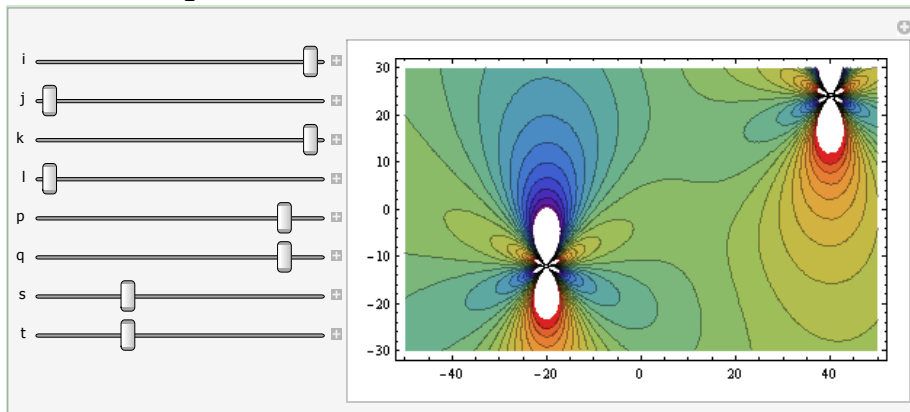
**TraditionalForm[σ22[x,y]]**

$$\begin{aligned}
& -((8.65458 \times 10^{-13} b1x (7.28 \times 10^{10} (2.86238 \times 10^{11} (x-m1)^2 (y-n1) + 3.98681 \times 10^{10} (y-n1)^3) - 1. \\
& (3.21973 \times 10^{22} (x-m1)^2 (y-n1) - 6.61164 \times 10^{21} (y-n1)^3)) / ((-0.233978 (x-m1) (y-n1) + (x- \\
& m1)^2 + 0.837565 (y-n1)^2) (0.233978 (x-m1) (y-n1) + (x-m1)^2 + 0.837565 (y- \\
& n1)^2))) + (8.65458 \times 10^{-13} b1y (1.98 \times 10^{11} (2.39743 \times 10^{11} (x-m1) (y-n1)^2 + 4.76 \times 10^{10} (x-m1)^3) - \\
& 0.367677 (2.69673 \times 10^{22} (x-m1) (y-n1)^2 - 7.89388 \times 10^{21} (x-m1)^3)) / ((-0.233978 (x-m1) (y- \\
& n1) + (x-m1)^2 + 0.837565 (y-n1)^2) (0.233978 (x-m1) (y-n1) + (x-m1)^2 + 0.837565 (y-n1)^2)) - \\
& (8.65458 \times 10^{-13} b2x (7.28 \times 10^{10} (2.86238 \times 10^{11} (x-m2)^2 (y-n2) + 3.98681 \times 10^{10} (y-n2)^3) - 1. \\
& (3.21973 \times 10^{22} (x-m2)^2 (y-n2) - 6.61164 \times 10^{21} (y-n2)^3)) / ((-0.233978 (x-m2) (y-n2) + (x- \\
& m2)^2 + 0.837565 (y-n2)^2) (0.233978 (x-m2) (y-n2) + (x-m2)^2 + 0.837565 (y-n2)^2)) + (8.65458 \times 10^{-13} \\
& b2y (1.98 \times 10^{11} (2.39743 \times 10^{11} (x-m2) (y-n2)^2 + 4.76 \times 10^{10} (x-m2)^3) - 0.367677 \\
& (2.69673 \times 10^{22} (x-m2) (y-n2)^2 - 7.89388 \times 10^{21} (x-m2)^3)) / ((-0.233978 (x-m2) (y-n2) + (x- \\
& m2)^2 + 0.837565 (y-n2)^2) (0.233978 (x-m2) (y-n2) + (x-m2)^2 + 0.837565 (y-n2)^2))
\end{aligned}$$

```

Manipulate[ContourPlot[{σ22[x,y]}/. {b1x→i,
b1y→j,b2x→k,b2y→l,m1→p, n1→q,m2→s,n2→t}], {x,-50,50}, {y,-
30,30}, (*control stress range*) PlotRange→{Full,All,{-
1000000000,1000000000}}, ColorFunction→"Rainbow", AspectRatio→Au
tomatic, Contours→20, ContourLabels→Automatic, ClippingStyle→Non
e], {i,0,1,0.1}, {j,0,0.6,0.1}, {k,0,1,0.1}, {l,0,0.6,0.1}, {p,-
50,50,1}, {q,-30,30,1}, {s,-50,50,1}, {t,-30,30,1}]

```

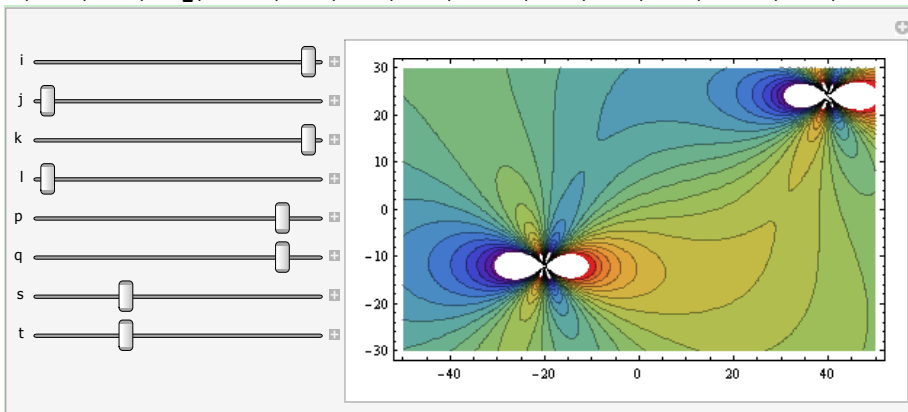


$$\begin{aligned}
\sigma_{22}[x_,y_] := & ((b1x*\lambda*(c12- \\
& cd11))/(4*Pi*Q1[x,y]*T1[x,y]*cd11*c66*\text{Sin}[\phi]))*(- \\
& c66*(c12+cd11)*((x-m1)^3-\lambda*\lambda*(x-m1)*(y-n1)^2))+(( \\
& -b1y*\lambda*(c12- \\
& cd11))/(4*Pi*Q1[x,y]*T1[x,y]*cd11*c66*\text{Sin}[\phi]))*(- \\
& c66*(c12+cd11)*(\lambda*\lambda*(y-n1)^3-(x-m1)^2*(y-n1)))+(b2x*\lambda*(c12- \\
& cd11))/(4*Pi*Q2[x,y]*T2[x,y]*cd11*c66*\text{Sin}[\phi]))*(- \\
& c66*(c12+cd11)*((x-m2)^3-\lambda*\lambda*(x-m2)*(y-n2)^2))+(( \\
& -b2y*\lambda*(c12- \\
& cd11))/(4*Pi*Q2[x,y]*T2[x,y]*cd11*c66*\text{Sin}[\phi]))*(- \\
& c66*(c12+cd11)*(\lambda*\lambda*(y-n2)^3-(x-m2)^2*(y-n2)))
\end{aligned}$$

**TraditionalForm[ $\sigma_{12}[x,y]$ ]**

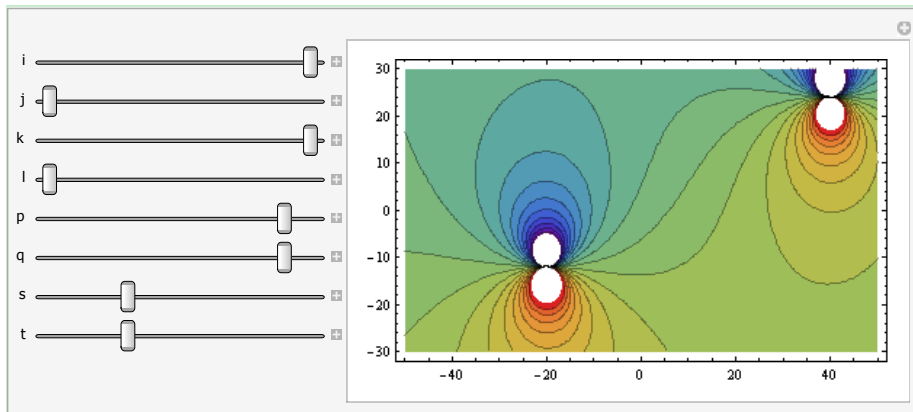
$$\frac{(9.83088 \times 10^9 b_1 x ((x-m_1)^3 - 0.837565 (x-m_1) (y-n_1)^2)) / ((-0.233978 (x-m_1) (y-n_1) + (x-m_1)^2 + 0.837565 (y-n_1)^2) (0.233978 (x-m_1) (y-n_1) + (x-m_1)^2 + 0.837565 (y-n_1)^2)) - (9.83088 \times 10^9 b_1 y (0.837565 (y-n_1)^3 - (x-m_1)^2 (y-n_1))) / ((-0.233978 (x-m_1) (y-n_1) + (x-m_1)^2 + 0.837565 (y-n_1)^2) (0.233978 (x-m_1) (y-n_1) + (x-m_1)^2 + 0.837565 (y-n_1)^2)) + (9.83088 \times 10^9 b_2 x ((x-m_2)^3 - 0.837565 (x-m_2) (y-n_2)^2)) / ((-0.233978 (x-m_2) (y-n_2) + (x-m_2)^2 + 0.837565 (y-n_2)^2) (0.233978 (x-m_2) (y-n_2) + (x-m_2)^2 + 0.837565 (y-n_2)^2)) - (9.83088 \times 10^9 b_2 y (0.837565 (y-n_2)^3 - (x-m_2)^2 (y-n_2))) / ((-0.233978 (x-m_2) (y-n_2) + (x-m_2)^2 + 0.837565 (y-n_2)^2) (0.233978 (x-m_2) (y-n_2) + (x-m_2)^2 + 0.837565 (y-n_2)^2))$$

**Manipulate[ContourPlot[{ $\sigma_{12}[x,y]$ }/. {b1x→i, b1y→j, b2x→k, b2y→l, m1→p, n1→q, m2→s, n2→t}], {x, -50, 50}, {y, -30, 30}, (\*control stress range\*) PlotRange→{Full, All, {-1000000000, 1000000000}}, ColorFunction→"Rainbow", AspectRatio→Automatic, Contours→20, ContourLabels→Automatic, ClippingStyle→None], {i, 0, 1, 0.1}, {j, 0, 0.6, 0.1}, {k, 0, 1, 0.1}, {l, 0, 0.6, 0.1}, {p, -50, 50, 1}, {q, -30, 30, 1}, {s, -50, 50, 1}, {t, -30, 30, 1}]**



**$\sigma_{33}[x_, y_] := 0.34 * (\sigma_{11}[x, y] + \sigma_{22}[x, y])$**

**Manipulate[ContourPlot[{ $\sigma_{33}[x,y]$ }/. {b1x→i, b1y→j, b2x→k, b2y→l, m1→p, n1→q, m2→s, n2→t}], {x, -50, 50}, {y, -30, 30}, (\*control stress range\*) PlotRange→{Full, All, {-1000000000, 1000000000}}, ColorFunction→"Rainbow", AspectRatio→Automatic, Contours→20, ContourLabels→Automatic, ClippingStyle→None], {i, 0, 1, 0.1}, {j, 0, 0.6, 0.1}, {k, 0, 1, 0.1}, {l, 0, 0.6, 0.1}, {p, -50, 50, 1}, {q, -30, 30, 1}, {s, -50, 50, 1}, {t, -30, 30, 1}]**



(\*New equation--Two Screw--Any Burgers vector direction & any location\*)

```
 $\tau_{xz}[\mathbf{x}_-, \mathbf{y}_-] := (\mathbf{b1z} / (2 * \text{Pi})) * \text{Sqrt}[(\mathbf{c44} * \mathbf{c55})] * ((-\mathbf{c55} * (\mathbf{y} - \mathbf{n1})) / (\mathbf{c44} * (\mathbf{x} - \mathbf{m1})^2 + \mathbf{c55} * (\mathbf{y} - \mathbf{n1})^2)) + (\mathbf{b2z} / (2 * \text{Pi})) * \text{Sqrt}[(\mathbf{c44} * \mathbf{c55})] * ((-\mathbf{c55} * (\mathbf{y} - \mathbf{n2})) / (\mathbf{c44} * (\mathbf{x} - \mathbf{m2})^2 + \mathbf{c55} * (\mathbf{y} - \mathbf{n2})^2))$ 
```

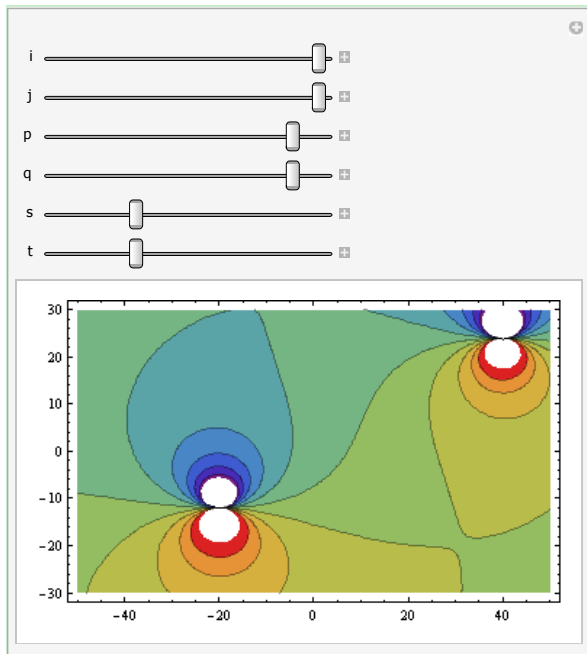
```
TraditionalForm[\mathbf{\tau_{xz}}[\mathbf{x}, \mathbf{y}]]
```

```

$$-\frac{(3.47512 \times 10^{20} \mathbf{b1z} (\mathbf{y} - \mathbf{n1}))}{(3.68 \times 10^{10} (\mathbf{x} - \mathbf{m1})^2 + 5.06 \times 10^{10} (\mathbf{y} - \mathbf{n1})^2)} - \frac{(3.47512 \times 10^{20} \mathbf{b2z} (\mathbf{y} - \mathbf{n2}))}{(3.68 \times 10^{10} (\mathbf{x} - \mathbf{m2})^2 + 5.06 \times 10^{10} (\mathbf{y} - \mathbf{n2})^2)}$$

```

```
Manipulate[ContourPlot[\mathbf{\tau_{xz}}[\mathbf{x}, \mathbf{y}]] /. {\mathbf{b1z} \to \mathbf{i}, \mathbf{b2z} \to \mathbf{j}, \mathbf{m1} \to \mathbf{p}, \mathbf{n1} \to \mathbf{q}, \mathbf{m2} \to \mathbf{s}, \mathbf{n2} \to \mathbf{t}}, {\mathbf{x}, -50, 50}, {\mathbf{y}, -30, 30}, (*control stress range*) PlotRange \to \{Full, All, \{-1000000000, 1000000000\}\}, ColorFunction \to "Rainbow", AspectRatio \to Automatic, Contours \to 10, ContourLabels \to Automatic, ClippingStyle \to None], {\mathbf{i}, 0, 1, 0.1}, {\mathbf{j}, 0, 1, 0.1}, {\mathbf{p}, -50, 50, 1}, {\mathbf{q}, -30, 30, 1}, {\mathbf{s}, -50, 50, 1}, {\mathbf{t}, -30, 30, 1}]
```



```

$$\tau_{yz}[\mathbf{x}_-, \mathbf{y}_-] := (-b1z / (2 * \text{Pi})) * \text{Sqrt}[(c44 * c55)] * ((c44 * (\mathbf{x} - m1)) / (c44 * (\mathbf{x} - m1)^2 + c55 * (\mathbf{y} - n1)^2)) + (-b2z / (2 * \text{Pi})) * \text{Sqrt}[(c44 * c55)] * ((c44 * (\mathbf{x} - m2)) / (c44 * (\mathbf{x} - m2)^2 + c55 * (\mathbf{y} - n2)^2))$$

```

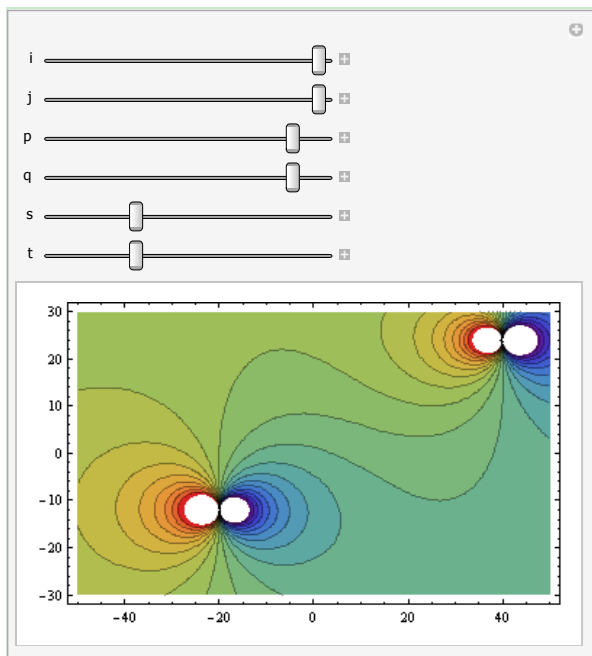
```
TraditionalForm[\(\tau_{yz}[\mathbf{x}, \mathbf{y}]\)]
```

```

$$-((2.52736 \times 10^{20} b1z (x - m1)) / (3.68 \times 10^{10} (x - m1)^2 + 5.06 \times 10^{10} (y - n1)^2)) - (2.52736 \times 10^{20} b2z (x - m2)) / (3.68 \times 10^{10} (x - m2)^2 + 5.06 \times 10^{10} (y - n2)^2)$$

```

```
Manipulate[ContourPlot[{\(\tau_{yz}[\mathbf{x}, \mathbf{y}]\)} /. {b1z -> i, b2z -> j, m1 -> p, n1 -> q, m2 -> s, n2 -> t}, {x, -50, 50}, {y, -30, 30}, (*control stress range*) PlotRange -> {Full, All, {-1000000000, 1000000000}}, ColorFunction -> "Rainbow", AspectRatio -> Automatic, Contours -> 20, ContourLabels -> Automatic, ClippingStyle -> None], {i, 0, 1, 0.1}, {j, 0, 1, 0.1}, {p, -50, 50, 1}, {q, -30, 30, 1}, {s, -50, 50, 1}, {t, -30, 30, 1}]
```



**5. Mathematica code for force calculation with generalized equation (equation 2) for two dislocation in anisotropic material**

```

c11=138.9*10^9
c22=198.0*10^9
c33=173.0*10^9
c44=36.8*10^9
c55=50.6*10^9
c66=47.6*10^9
c12=72.8*10^9
c13=52.5*10^9
c23=45.8*10^9

```

```

1.389×1011
1.98×1011
1.73×1011
3.68×1010
5.06×1010
4.76×1010
7.28×1010
5.25×1010
4.58×1010

```

```

cd11=Sqrt[c11*c22]
1.65838×1011

```

```

λ=Sqrt[Sqrt[c11/c22]]
0.915186

```

```

φ=1/2*ArcCos[(c12*c12+2*c12*c66-cd11*cd11)/(2*cd11*c66)]
1.44261

```

```

Q[x_,y_] := x*x+2*x*y*λ*Cos[φ]+y*y*λ*λ
T[x_,y_] := x*x-2*x*y*λ*Cos[φ]+y*y*λ*λ

```

```

σ11[x_,y_] := ((bx*λ*(c12-
cd11))/(4*Pi*Q[x,y]*T[x,y]*cd11*c66*Sin[φ]))*(c11*((cd11+c12+c
66)*x*x*y+λ*λ*c66*y*y*y) -
(c12/c22)*((c12*c12+cd11*c12+2*c12*c66+cd11*c66)*x*x*y-
cd11*c66*λ*λ*y*y*y))+((
-by*λ*(c12-
cd11))/(4*Pi*Q[x,y]*T[x,y]*cd11*c66*Sin[φ]))*(c12*((cd11+c12+c

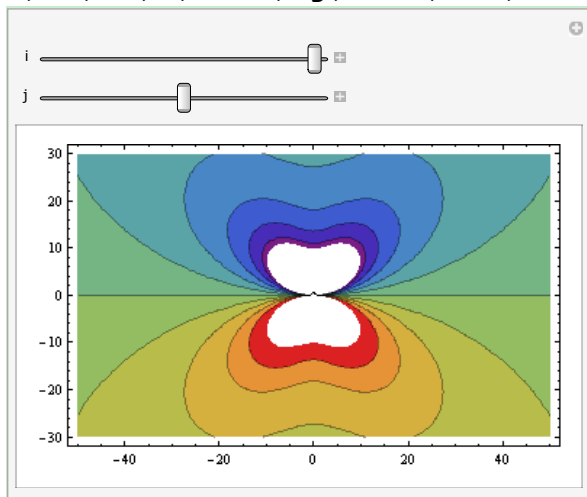
```

```
66)*λ*λ*x*y*y+c66*x*x*x) -
(c11/c22)*((c12*c12+cd11*c12+2*c12*c66+cd11*c66)*λ*λ*x*y*y-
cd11*c66*x*x*x)
```

```
TraditionalForm[σ11[x,y]]
```

```
(8.65458×10-13 by (7.28×1010 (4.76×1010 x3+2.39743×1011 x y2)-0.701515 (2.69673×1022 x
y2-7.89388×1021 x3)))/((x2-0.233978 x y+0.837565 y2) (x2+0.233978 x y+0.837565 y2))-
(8.65458×10-13 bx (1.389×1011 (2.86238×1011 x2 y+3.98681×1010 y3)-0.367677
(3.21973×1022 x2 y-6.61164×1021 y3)))/((x2-0.233978 x y+0.837565 y2) (x2+0.233978 x
y+0.837565 y2))
```

```
Manipulate[ContourPlot[{σ11[x,y]}/.{bx→i, by→j},{x,-
50,50},{y,-30,30},(*cotrol stress
range*)PlotRange→{Full,All},{-
1000000000,1000000000}],ColorFunction→"Rainbow",Contours→10,Co
ntourLabels→Automatic,AspectRatio→Automatic,ClippingStyle→Non
e},{i,-1,1,0.1},{j,-0.6,0.6,0.1}]
```



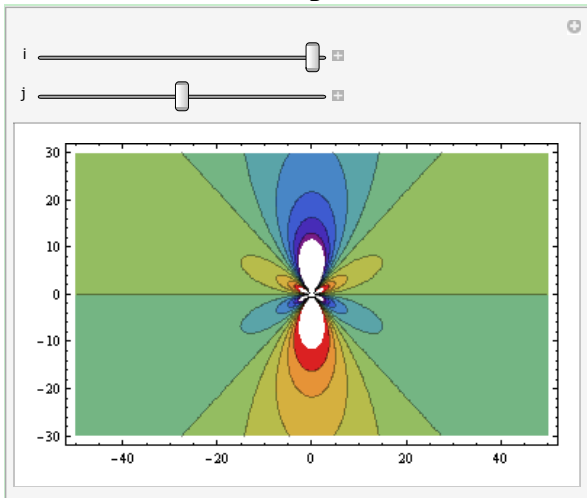
```
σ22[x_,y_] := ((bx*λ*(c12-
cd11))/(4*Pi*Q[x,y]*T[x,y]*cd11*c66*Sin[φ]))*(c12*((cd11+c12+c
66)*x*x*y+λ*λ*c66*y*y*y) -
(c22/c22)*((c12*c12+cd11*c12+2*c12*c66+cd11*c66)*x*x*y-
cd11*c66*λ*λ*y*y*y)) + ((-by*λ*(c12-
cd11))/(4*Pi*Q[x,y]*T[x,y]*cd11*c66*Sin[φ]))*(c22*((cd11+c12+c
66)*λ*λ*x*y*y+c66*x*x*x) -
(c12/c22)*((c12*c12+cd11*c12+2*c12*c66+cd11*c66)*λ*λ*x*y*y-
cd11*c66*x*x*x))
```

```
TraditionalForm[σ22[x,y]]
```

```
(8.65458×10-13 by (1.98×1011 (4.76×1010 x3+2.39743×1011 x y2)-0.367677 (2.69673×1022 x
y2-7.89388×1021 x3)))/((x2-0.233978 x y+0.837565 y2) (x2+0.233978 x y+0.837565 y2))-
```

$$(8.65458 \times 10^{-13} \text{bx} (7.28 \times 10^{10} (2.86238 \times 10^{11} x^2 y + 3.98681 \times 10^{10} y^3) - 1. (3.21973 \times 10^{22} x^2 y - 6.61164 \times 10^{21} y^3))) / ((x^2 - 0.233978 x y + 0.837565 y^2) (x^2 + 0.233978 x y + 0.837565 y^2))$$

```
Manipulate[ContourPlot[{σ22[x,y]} /. {bx→i, by→j}, {x, -50, 50}, {y, -30, 30}, (*cotrol stress range*) PlotRange→{Full, All, {-1000000000, 1000000000}}, ColorFunction→"Rainbow", Contours→10, ContourLabels→Automatic, AspectRatio→Automatic, ClippingStyle→None], {i, -1, 1, 0.1}, {j, -0.6, 0.6, 0.1}]
```

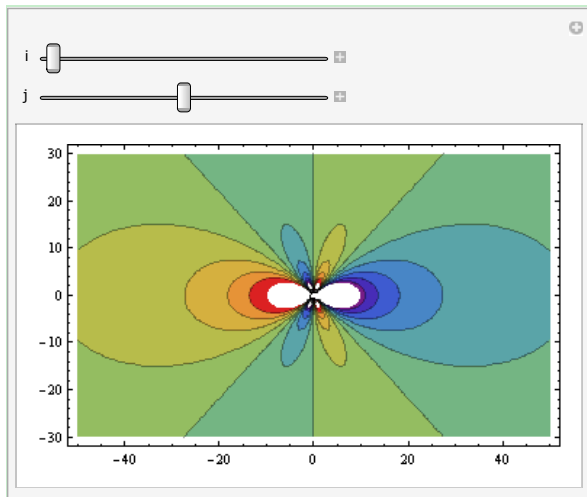


```
σ12[x_, y_] := ((bx*λ*(c12 - cd11)) / (4*Pi*Q[x, y]*T[x, y]*cd11*c66*Sin[φ])) * (-c66*(c12 + cd11) * (x*x*x - λ*λ*x*y*y)) + ((-by*λ*(c12 - cd11)) / (4*Pi*Q[x, y]*T[x, y]*cd11*c66*Sin[φ])) * (-c66*(c12 + cd11) * (λ*λ*y*y*y - x*x*y))
```

```
TraditionalForm[σ12[x, y]]
```

$$(9.83088 \times 10^9 \text{bx} (x^3 - 0.837565 x y^2)) / ((x^2 - 0.233978 x y + 0.837565 y^2) (x^2 + 0.233978 x y + 0.837565 y^2)) - (9.83088 \times 10^9 \text{by} (0.837565 y^3 - x^2 y)) / ((x^2 - 0.233978 x y + 0.837565 y^2) (x^2 + 0.233978 x y + 0.837565 y^2))$$

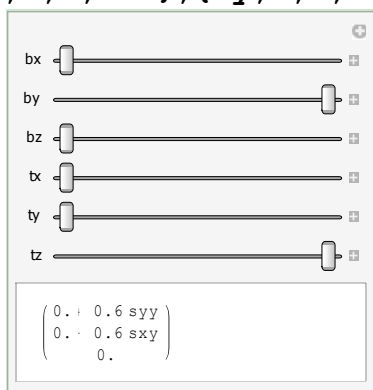
```
Manipulate[ContourPlot[{σ12[x,y]} /. {bx→i, by→j}, {x, -50, 50}, {y, -30, 30}, (*cotrol stress range*) PlotRange→{Full, All, {-1000000000, 1000000000}}, ColorFunction→"Rainbow", Contours→10, ContourLabels→Automatic, AspectRatio→Automatic, ClippingStyle→None], {i, -1, 1, 0.1}, {j, -0.6, 0.6, 0.1}]
```



(\*End of Calculating Stress Field of Dislocation 1\*)

(\*Next step is to input the Force equation for two dislocations. The Burgers vector for dislocation 1 is fixed and the Burgers vector and sense vector of dislocation 2 could be any value:  $b_x, b_y, b_z$  stands for Burgers vector component for dislocation 2, and  $t_x, t_y, t_z$  stands for sense vector.  $s_{xx}, s_{yy}, s_{zz}$  etc. stands for the stress values of dislocation 1.\*)

```
Manipulate[MatrixForm[{bx sxx+by sxy+bz sxz,bx sxy+by syy+bz
syz,bx sxz+by syz+bz
szz}*{tx,ty,tz}],{bx,0,1,0.1},{by,0,0.6,0.1},{bz,0,0.5,0.1},{t
x,0,1,0.1},{ty,0,1,0.1},{tz,0,1,0.1}]
```



(\*By adjusting slide bars, we can get magnitude of forces applied on dislocation 2 (with any Burgers/sense vector) from dislocation 1 in  $x, y, z$  directions\*)

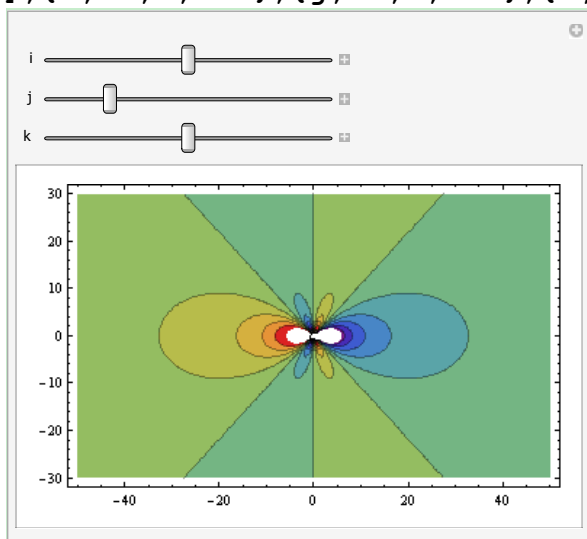
(\*in our case, sense vector of dislocation 2 is always (001),

when the Burgers vector is (100), the force in x direction is  $s_{xy}$ , in y direction is  $-s_{xx}$ ,  
 when the Burgers vector is (110), the force in x direction is  $s_{xy}+s_{yy}$ , in y direction is  $-s_{xx}-s_{xy}$ ,  
 when the Burgers vector is (010), the force in x direction is  $s_{yy}$ , in y direction is  $-s_{xy}$ ,  
 when the Burgers vector is (-100), the force in x direction is  $-s_{xy}$ , in y direction is  $s_{xx}$ .

So we could easily draw the force field with the obtained data of stress field  $s_{xx}$ ,  $s_{xy}$ , and  $s_{yy}$  in the first part

\*)

```
Manipulate[ContourPlot[{i*σ11[x,y]}+{j*σ12[x,y]}+{k*σ22[x,y]}/
 .{bx→1, by→0},{x,-50,50},{y,-30,30},(*control stress
 range*)PlotRange→{Full,All,{-
 1000000000,1000000000}},ColorFunction→"Rainbow",Contours→10,Co
 ntourLabels→Automatic,AspectRatio→Automatic,ClippingStyle→Non
 e],{i,-1,1,0.1},{j,-1,1,0.1},{k,-1,1,0.1}]
```



End